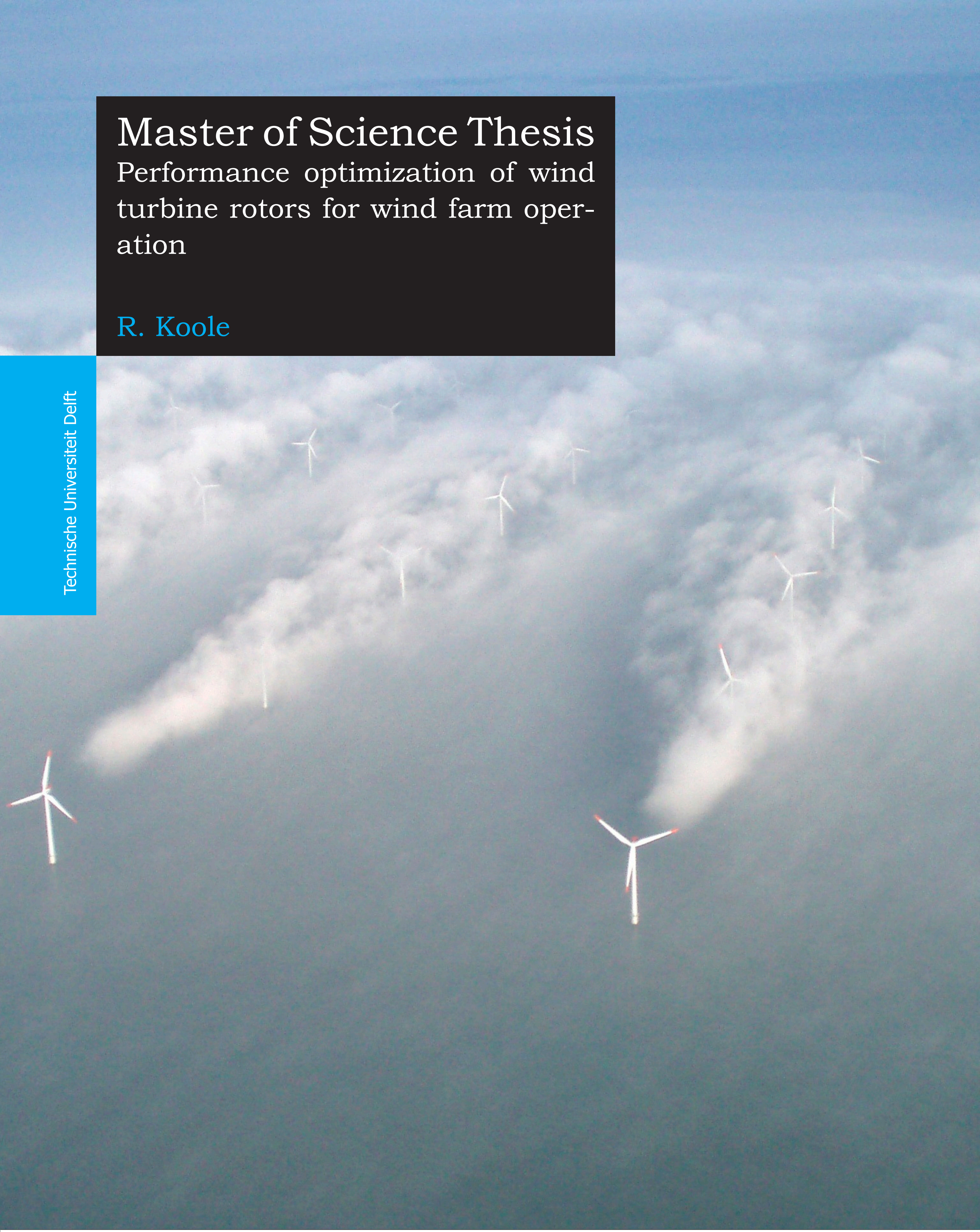

# Master of Science Thesis

## Performance optimization of wind turbine rotors for wind farm operation

R. Koole

Technische Universiteit Delft

Delft University of Technology

Challenge the future

# Master of Science Thesis

## Performance optimization of wind turbine rotors for wind farm operation

by

**R. Koole**

For obtaining the degree of

**Master of Science**
in Aerospace Engineering

at Delft University of Technology,
to be defended publicly on Thursday July 2, 2015 at 09:30 AM.

| | | |
|---|---|---|
| Date: | June 18, 2015 | |
| Research group: | Wind Energy | |
| Faculty: | Aerospace Engineering | |
| University: | Delft University of Technology | |
| External partner: | Energy research Centre of the Netherlands (ECN) | |
| Supervisor: | Dr. M. B. Zaaijer | |
| Thesis committee: | Prof. dr. G. J. W. Van Bussel, | TU Delft, chair |
| | Dr. M. B. Zaaijer, | TU Delft, supervisor |
| | Dr. A. Elham, | TU Delft |
| | Ir. Ö. Ceyhan, | ECN |

The work in this thesis was supported by ECN and conducted at ECN. Their cooperation is hereby gratefully acknowledged.

# Abstract

Due to fierce competition on the electricity market, many wind energy related research projects are currently aimed at cost reduction. In order to establish the cost reduction, more and more wind turbines are being clustered in (offshore) wind farms. Major drawback of wind farms however, is the energy production loss due to aerodynamic wake interaction between wind turbines.

Optimizing wind turbine rotor designs on wind farm scale instead of focussing on wind turbine level, can increase the energy production of a wind farm. The increase can amongst others be established by optimization of wind turbine thrust and power curves. Thrust and power curves are related to the axial induction factor of wind turbine rotors, by using momentum theory.

In the current project, optimization problems have been investigated that manipulate wind turbine performance parameters. The optimization parameters are the axial induction factor curves of the wind turbines, which were either parametrized by discrete data points or by Bézier control points.

The parameters were manipulated by Matlab's optimization toolbox, using built-in optimization algorithms. The optimization algorithm searches for the optimum axial induction factor curve, yielding the lowest wake losses and resulting in the maximum annual energy production of a wind farm. A requisite of the optimization problems is the use of ECN's wind farm-wake simulation tool 'FarmFlow-fast', to calculate the annual energy production of a wind farm for each evaluated set of optimization parameter values.

The current project involved two main objectives. First, the FarmFlow-fast model had to be validated for optimization purposes. This was done by performing simulations with the software, based on predefined flow scenarios. The results of the simulations were compared with power measurement data, taken from the Horns Rev and Lillgrund wind farms.

Secondly, the potential of wind turbine performance curve optimization had to be investigated. This was done by investigating multiple performance curve optimization scenarios, in which the increase in annual energy production of a wind farm was calculated as function of the wind turbine performance curves.

It is found that FarmFlow-fast is capable to be used for optimization purposes. The quality of the FarmFlow-fast simulations was not worse than the simulations of the already validated original 'FarmFlow' version. FarmFlow-fast however performed approximately 19 times quicker than the original FarmFlow version.

The influence of the ambient turbulence intensity, wind turbine spacing and wind speed range on the quality of FarmFlow-fast simulation results can not be judged based on the FarmFlow-fast validation study. More validation cases have to be investigated for getting a better impression of the above mentioned influences. Investigation of more validation cases however requires additional measurement data.

The most suitable optimization algorithm for the investigated optimization problems, concerning time consumption and objective function value decrement, is the "patternsearch" algorithm. Unique optimum performance curves were found, depending on the wind farm layout, accounted wind speed and direction ranges and the used performance curve parametrization and optimization method.

It was found that increasing the number of wind turbines in a wind farm results into higher energy-loss fractions. The relative gain in annual energy production after optimization was however higher when the number of wind turbines was increased. The optimum performance curves move further away from the Betz limit, as the number of wind turbines increases.

The contribution of a free-stream wind turbine to the total energy-loss fraction of a wind farm proved to be substantial. It turned out that it is more beneficial to only manipulate the performance curves of free-stream wind turbines, than to use the same optimized performance curves for all wind turbines. This implies that there is a potential for considering different rotors for the first wind turbine row of a wind farm than the rotors of the other wind turbines.

The optimized performance curves increase the annual energy production of a wind farm, with respect to wind turbines operating at the Betz limit. Bézier curve parametrization performed in the order of 20 times quicker than using discrete data points.

Although the potential increase in annual energy production can be considered rather small, the thrust reduction on wind turbine rotors around rated wind speed might as well be an important outcome of the optimization runs. The thrust reduction can result in cheaper wind turbine designs, which might even be a more promising result in terms of cost of energy reduction than the increase in annual energy production. The results of this project contribute to choosing new design parameters for future wind turbine rotor designs, in order to minimize the costs of energy.

# Acknowledgements

I wish to thank the following persons. First of all I would like to thank my supervisors Michiel Zaaijer (Delft University of Technology) and Özlem Ceyhan (Energy research Centre of the Netherlands (ECN)), for guiding me in this project. Their experience and knowledge have helped me in choosing which areas to further investigate and we had good discussions about the results.

Furthermore, I would like to thank the people of the Wind Energy section at ECN for providing me and the other students a good working environment. I would also like to thank Francesco Grasso (ECN) for his support with the optimization algorithms and the Bézier curve parametrization. His knowledge provided me insights which I would never have obtained by solely reading papers, during the time I spend at ECN.

I would especially like to thank Edwin Bot (ECN), being the person that helped me out with all FarmFlow-fast issues that occurred during the project. His out ‘out of the box’ way of thinking considerably influenced the choices I made regarding calculation and parametrization methods and taught me how results had to be interpreted.

*R. Koole*
*Bergambacht, June 2015*

# Contents

# Glossary

| | |
|---|---|
| Energy-loss fraction | Fractional energy loss between the actual annual energy production and the annual energy production without wake losses. |
| FarmFlow | ECN's wind farm-wake simulation tool that solves the 3D steady parabolized Navier-Stokes equations in disturbance form. |
| FarmFlow-fast | Quicker variant to the original FarmFlow. Especially developed for optimization purposes concerning the shorter calculation times. |
| Objective function | An equation to be optimized given certain constraints and with variables that need to be minimized or maximized using programming techniques. |
| Optimization parameters | Model parameters to be optimized for reducing the objective function values. |
| Power-loss fraction | Fractional power generation loss of a wind turbine operating in a wake with respect to a wind turbine exposed to undisturbed meteorological conditions. |

# Acronyms

| | |
|---|---|
| ABL | Atmospheric Boundary Layer. |
| ADI | Alternating Direction Implicit. |
| AEP | Annual Energy Production. |
| CFD | Computational Fluid Dynamics. |
| CG | Conjugate Gradient. |
| COE | Costs Of Energy. |
| CP | Control Points. |
| DTU | Technical University of Denmark. |
| ECN | Energy research Centre of the Netherlands. |
| FLaP | Farm Layout Program. |
| fminc | fmincon. |
| fmins | fminsearch. |
| GA | Genetic Algorithm. |
| GPS | Generalized Pattern Search. |
| KKT | Karush-Kuhn-Tucker. |
| LES | Large Eddy Simulation. |
| NPV | Net Present Value. |
| NREL | National Renewable Energy Laboratory. |
| O&M | Operation & Maintenance. |
| PCHIP | Piecewise Cubic Hermite Interpolating Polynomial. |
| PS | Pattern Search. |
| SA | Simulated Annealing. |
| SGS | Sub-Grid Scale. |
| SIMPLE | Semi-Implicit Method for Pressure Linked Equations. |
| SODAR | SOnic Detection And Ranging. |
| SOWFA | Simulator for Offshore Wind Farm Applications. |
| TNO | Netherlands Organisation for Applied Scientific Research. |
| WAsP | Wind Atlas Analysis and Application Program. |
| WT | Wind Turbine. |

# List of Symbols

| | |
|---|---|
| $\lvert\Delta u_\infty\rvert$ | Rotor-averaged wind speed interval $[\mathrm{m/s}]$. |
| $\lvert\Delta V_\infty\rvert$ | Free-stream wind speed interval $[\mathrm{m/s}]$. |
| $\lvert\Delta x\rvert$ | Grid size in stream-wise direction $[\mathrm{m}]$. |
| $\lvert\Delta\theta_\infty\rvert$ | Wind direction sector $[^\circ]$. |
| $\lvert\Delta\overline{\xi}_{P_{\mathrm{FN,max}}}\rvert$ | Maximum absolute difference in calculated power-loss fraction between FarmFlow-fast and FarmFlow averaged over a wind direction sector $[\%]$. |
| $\lvert\Delta\overline{\xi}_{P_{\mathrm{SM,max}}}\rvert$ | Maximum absolute difference in power-loss fraction between simulations and measurements averaged over a wind direction sector $[\%]$. |
| $A$ | Weibull scale parameter $[\mathrm{m/s}]$. |
| $a$ | Axial induction factor $[-]$. |
| $\mathbf{a}$ | Vector of axial induction factor optimization parameters $[-]$. |
| $a_{\mathrm{Betz}}$ | Axial induction factor of a wind turbine operating at the Betz limit $[-]$. |
| $\mathbf{A}_{eq}$ | Matrix part of linear equality constraints. |
| $a_{\mathrm{i}}$ | Axial induction factor of wind turbine $i$ $[-]$. |
| $a_{\mathrm{i,init}}$ | Initial axial induction factor value of wind turbine $i$ for an optimization run $[-]$. |
| $a_{\mathrm{i,opt,'method'}}$ | Optimum axial induction factor of wind turbine $i$ found by 'method' $[-]$. |
| $\mathbf{a}_{\mathrm{init,'alt'}}$ | Vector of initial optimization parameter values alternative 'alt'$[-]$. |
| $\mathbf{A}_{neq}$ | Matrix part of linear inequality constraints. |
| $\mathbf{a}_{\mathrm{opt}}$ | Vector of optimum axial induction factor values $[-]$. |
| $a_{\mathrm{u}_\infty}$ | Discrete axial induction factor value at rotor-averaged wind speed $u_\infty$ $[-]$. |
| $a_{\mathrm{u}_\infty,\mathrm{Betz}}$ | Discrete axial induction factor value at rotor-averaged wind speed $u_\infty$ of a Betz wind turbine $[-]$. |
| $AEP$ | Annual energy production of $N_{\mathrm{wt}}$ wind turbines $[\mathrm{GWh}]$. |
| $AEP_{\mathrm{Betz}}$ | Annual energy production of $N_{\mathrm{wt}}$ Betz wind turbines $[\mathrm{GWh}]$. |
| $AEP_{\mathrm{i}}$ | Annual energy production of wind turbine $i$ $[\mathrm{GWh}]$. |
| $AEP_{\mathrm{no\ loss}}$ | Annual energy production without wake losses $[\mathrm{GWh}]$. |
| $\Delta AEP_{\mathrm{opt,Betz}}$ | Difference in total annual energy production between $N_{\mathrm{wt}}$ optimized wind turbines and $N_{\mathrm{wt}}$ Betz wind turbines $[\mathrm{MWh}]$. |
| $AEP_{\mathrm{ref}}$ | Annual energy production of a Betz wind turbine facing undisturbed meteorological conditions $[\mathrm{GWh}]$. |
| $AEP_{\mathrm{tot}}$ | Total annual energy production of $N_{\mathrm{wt}}$ wind turbines $[\mathrm{GWh}]$. |
| $AEP_{\mathrm{'type'}}$ | Annual energy production of a type 'type' wind turbine $[\mathrm{GWh}]$. |
| $\mathbf{b}_{eq}$ | Constant part of linear equality constraints. |
| $\mathbf{b}_{neq}$ | Constant part of linear inequality constraints. |
| $\mathbf{c}$ | Outside contraction point. |
| $\mathbf{c}_{eq}$ | Non-linear equality constraints. |
| $c_{\mathrm{j}}$ | Fitting parameters for function $f_\xi$ $[-]$. |
| $\mathbf{c}_{neq}$ | Non-linear inequality constraints. |
| $C_{\mathrm{P}}$ | Power coefficient $[-]$. |
| $C_{\mathrm{T}}$ | Thrust coefficient $[-]$. |
| $C_{\mathrm{T}_{\mathrm{u}_\infty}}$ | Discrete thrust coefficient value at rotor-averaged wind speed $u_\infty$ $[-]$. |
| $\mathbf{cc}$ | Inside contraction point. |
| $D$ | Rotor diameter $[\mathrm{m}]$. |
| $\mathbf{d}_j$ | Set of vectors obtained by multiplying pattern vectors with the mesh size. |
| $\mathbf{e}$ | Vector of ones with the same size as $\mathbf{g}$. |
| $f$ | Objective function of an optimization problem. |

| | |
|---|---|
| $f_\xi$ | Fitting function for power-loss fraction as function of the angle between the wind turbine row orientation and the wind direction $[\%]$. |
| $\Delta f_{no}$ | Absolute difference between the new and the old objective function value. |
| $g$ | Gravitational acceleration $[\mathrm{m/s^2}]$. |
| $\mathbf{g}$ | Inequality constraint functions. |
| $\mathbf{H}$ | Hessian of the Lagrangian of the approximate function. |
| $\mathbf{h}$ | Equality constraint functions. |
| $i$ | Wind turbine number $[-]$. |
| $I_{\mathrm{AEP}}$ | Relative annual energy production increase fraction between the optimized performance curves and Betz performance curves $[\%]$. |
| $I_{\mathrm{P}}$ | Relative total power generation increase fraction between Betz conditions and the optimum axial induction factor $[\%]$. |
| $\mathbf{J_g}$ | Jacobian of the constraint function $\mathbf{g}$. |
| $\mathbf{J_h}$ | Jacobian of the constraint function $\mathbf{h}$. |
| $k$ | Weibull shape parameter $[-]$. |
| $L$ | Monin-Obukhov length $[\mathrm{m}]$. |
| $\mathbf{l}$ | Lower bounds of optimization parameters. |
| $\mathcal{L}$ | Lagrangian. |
| $\mathbf{m}$ | Middle point between all points except the point with the highest objective function value in a simplex. |
| $N$ | Number of independent variables in the objective function. |
| $n$ | Number of optimization parameters $[-]$. |
| $N_{\mathrm{B}}$ | Number of Bézier control points. |
| $N_{\mathrm{wt}}$ | Number of wind turbines $[-]$. |
| $P$ | Wind turbine power generation $[\mathrm{kW}]$. |
| $p$ | Probability of occurrence $[\%]$. |
| $P_{\lvert\Delta\theta_\infty\rvert}$ | Averaged power generation over a $\lvert\Delta\theta_\infty\rvert$ wind direction sector $[\mathrm{kW}]$. |
| $P_{\mathrm{free}}$ | Power generation of a free-stream wind turbine $[\mathrm{kW}]$. |
| $P_{\mathrm{i}}$ | Power generation of wind turbine $i$ $[\mathrm{kW}]$. |
| $P_{\mathrm{i,init}}$ | Initial power generation of wind turbine $i$ $[\mathrm{kW}]$. |
| $P_{\mathrm{i,opt}}$ | Optimum power generation of wind turbine $i$ $[\mathrm{kW}]$. |
| $\Delta P_{opt,Betz}$ | Difference in total power generation between $N_{\mathrm{wt}}$ optimized wind turbines and $N_{\mathrm{wt}}$ Betz wind turbines $[\mathrm{kW}]$. |
| $P_{\mathrm{rated}}$ | Wind turbine rated power $[\mathrm{kW}]$. |
| $P_{\mathrm{ref}}$ | Power generation of a Betz wind turbine facing undisturbed meteorological conditions $[\mathrm{kW}]$. |
| $P_{\mathrm{sim}}$ | Power generation value obtained by FarmFlow-fast simulations $[\mathrm{kW}]$. |
| $P_{\mathrm{tot,Betz}}$ | Total power generation of $N_{\mathrm{wt}}$ Betz wind turbines $[\mathrm{kW}]$. |
| $P_{\mathrm{tot,init}}$ | Total initial power generation of $N_{\mathrm{wt}}$ wind turbines $[\mathrm{kW}]$. |
| $P_{\mathrm{tot,opt}}$ | Total power generation of $N_{\mathrm{wt}}$ optimized wind turbines $[\mathrm{kW}]$. |
| $P_{\mathrm{u}_\infty}$ | Discrete power value at rotor-averaged wind speed $u_\infty$ $[\mathrm{kW}]$. |
| $P_{\mathrm{WA}}$ | Weighted average power generation after compensating for wind direction uncertainty $[\mathrm{kW}]$. |
| $P_{\mathrm{wake}}$ | Power generation of wind turbine(s) operating in the wake of a free-stream wind turbine $[\mathrm{kW}]$. |
| $q$ | Annealing parameter. |
| $R$ | Radius of the trust region $[-]$. |
| $\mathbf{r}$ | Reflected point. |
| $\mathbf{S}$ | $diag(\mathbf{s})$. |
| $\Delta s$ | Distance between wind turbines $[\mathrm{m}]$. |
| $\mathbf{s}$ | Vector of slack variables. |
| $T$ | Absolute temperature $[\mathrm{K}]$. |
| $t_{\mathrm{opt}}$ | Optimization time $[\mathrm{min}]/[\mathrm{hrs}]$. |
| $t_{\mathrm{opt,'method'}}$ | Optimization time of 'method' $[\mathrm{min}]/[\mathrm{hrs}]$. |
| $T_{\mathrm{year}}$ | Hours per year $[\mathrm{hrs}]$. |
| $TI$ | Turbulence intensity $[\%]$. |

| | |
|---|---|
| $TI_\infty$ | Ambient turbulence intensity at hub height $[\%]$. |
| $TI_{\infty,\mathrm{z}}$ | Ambient turbulence intensity at height $z$ $[\%]$. |
| $\mathbf{u}$ | Upper bounds of optimization parameters. |
| $u_\infty$ | Rotor-averaged wind speed $[\mathrm{m/s}]$. |
| $u_{*0}$ | Near-surface friction velocity $[\mathrm{m/s}]$. |
| $\mathbf{u}_{\infty,\mathrm{opt}}$ | Vector with the rotor-averaged wind speeds of the optimum control points for optimization problems using Bézier curve parametrization $[\mathrm{m/s}]$. |
| $u_\mathrm{d}$ | Wind speed at the rotor disk $[\mathrm{m/s}]$. |
| $u_\mathrm{rated}$ | Rotor-averaged rated wind speed $[\mathrm{m/s}]$. |
| $\mathbf{v}$ | Shrinked simplex points. |
| $V_\infty$ | Free-stream wind speed at hub height $[\mathrm{m/s}]$. |
| $V_{\infty,\mathrm{rated,i}}$ | Rated free-stream wind speed of wind turbine $i$ $[\mathrm{m/s}]$. |
| $V_{\infty,\mathrm{z}}$ | Free-stream wind speed at height $z$ $[\mathrm{m/s}]$. |
| $V_\mathrm{in}$ | Cut-in wind speed $[\mathrm{m/s}]$. |
| $\mathbf{v}_j$ | Set of vectors that the pattern search algorithm uses to determine which points to search at each iteration. |
| $V_\mathrm{opt,max}$ | Maximum optimization velocity $[\mathrm{m/s}]$. |
| $V_\mathrm{out}$ | Cut-out wind speed $[\mathrm{m/s}]$. |
| $V_\mathrm{tip,max}$ | Maximum tip speed $[\mathrm{m/s}]$. |
| $w'$ | Fluctuating term of the vertical wind speed $[\mathrm{m/s}]$. |
| $\overline{w'\theta_0'}$ | Vertical turbulent heat flux $[\mathrm{K\cdot m/s}]$. |
| $w_j$ | Gradient of the objective function in direction $j$ times the difference of bounds in direction $j$. |
| $\overline{WPD}_\mathrm{z}$ | Average wind power density at height $z$ $[\mathrm{W/m^2}]$. |
| $x$ | Distance in the wake $[\mathrm{m}]$. |
| $\mathbf{x}$ | Vector with optimization parameters. |
| $\mathbf{x}_0$ | Initial set of optimization parameter values. |
| $x_\mathrm{fw}$ | Starting distance of the far wake $[\mathrm{m}]$. |
| $x_\mathrm{i}$ | $x$-location of wind turbine $i$ $[\mathrm{m}]$. |
| $x_\mathrm{iw}$ | Starting distance of the intermediate wake $[\mathrm{m}]$. |
| $x_\mathrm{nw}$ | Starting distance of the near wake $[\mathrm{m}]$. |
| $\mathbf{y}$ | Lagrange multiplier vector associated with $\mathbf{h}$. |
| $y_\mathrm{i}$ | $y$-location of wind turbine $i$ $[\mathrm{m}]$. |
| $z$ | Height above the ground $[\mathrm{m}]$. |
| $\mathbf{z}$ | Expansion point. |
| $z_0$ | Aerodynamic roughness length $[\mathrm{m}]$. |
| $z_\mathrm{hub}$ | Wind turbine hub height $[\mathrm{m}]$. |
| $\Delta^m$ | Mesh size. |
| $\epsilon$ | Mesh tolerance of the pattern search algorithm $[-]$. |
| $\theta_\infty$ | Free-stream wind direction $[^\circ]$. |
| $\theta_0$ | Potential temperature $[\mathrm{K}]$. |
| $\boldsymbol{\theta}_\infty$ | Vector of wind directions used in optimization problems $[^\circ]$. |
| $\theta'$ | Angle between the orientation of a wind turbine row and the wind direction $[^\circ]$. |
| $\Delta\theta_\infty$ | Wind direction offset $[^\circ]$. |
| $\overline{\theta}_\infty$ | Average wind direction of an investigated wind direction sector $[^\circ]$. |
| $\theta_{\infty,\mathrm{z}}$ | Free-stream wind direction at height $z$ $[^\circ]$. |
| $\kappa$ | Von Kármán constant $[-]$. |
| $\lambda$ | Tip-speed ratio $[-]$. |
| $\boldsymbol{\lambda}$ | Lagrange multiplier vector associated with constraints $\mathbf{g}$. |
| $\boldsymbol{\Lambda}$ | $diag(\boldsymbol{\lambda})$. |
| $\mu$ | Barrier function approximation constant $[-]$. |
| $\nu$ | Merit function parameter $[-]$. |
| $\overline{\xi}_{\mathrm{P_{i,M}}}$ | Measured power-loss fraction of wind turbine $i$ averaged over a wind direction sector $[\%]$. |

| | |
|---|---|
| $\overline{\xi}_{\mathrm{P_{i,S}}}$ | Power-loss fraction of wind turbine $i$ calculated from simulations averaged over a wind direction sector [%]. |
| $\xi_{\mathrm{AEP}}$ | Energy-loss fraction [%]. |
| $\xi_{\mathrm{AEP,Betz}}$ | Energy-loss fraction of $N_{\mathrm{wt}}$ Betz wind turbines [%]. |
| $\xi_{\mathrm{AEP,farm}}$ | Energy-loss fraction of a wind farm with $N_{\mathrm{wt}}$ wind turbines [%]. |
| $\xi_{\mathrm{AEP,opt}}$ | Energy-loss fraction of $N_{\mathrm{wt}}$ optimized wind turbines [%]. |
| $\xi_{\mathrm{AEP,ref}}$ | Energy-loss fraction of a wind farm with $N_{\mathrm{wt}}$ Betz wind turbines [%]. |
| $\xi_{\mathrm{AEP_{tot}}}$ | Energy-loss fraction of a complete wind farm over all wind directions [%]. |
| $\xi_{\mathrm{AEP}_{\theta_\infty}}$ | Energy-loss fraction at wind direction $\theta_\infty$ [%]. |
| $\overline{\xi}_{\mathrm{AEP}_{\boldsymbol{\theta}_\infty}}$ | Average energy-loss fraction over wind directions $\boldsymbol{\theta}_\infty$ [%]. |
| $\xi_{\mathrm{P}}$ | Power-loss fraction [%]. |
| $\overline{\xi}_{\mathrm{P}}$ | Average power-loss fraction over a wind direction sector [%]. |
| $\xi_{\mathrm{P_{2,M,max}}}$ | Maximum power-loss fraction of a single wake wind turbine calculated from measurements [%]. |
| $\xi_{\mathrm{P_{2,S,max}}}$ | Maximum power-loss fraction of a single wake wind turbine calculated from simulations [%]. |
| $\xi_{\mathrm{P,Betz}}$ | Total power-loss fraction of $N_{\mathrm{wt}}$ Betz wind turbines [%]. |
| $\xi_{\mathrm{P,opt}}$ | Total power-loss fraction of $N_{\mathrm{wt}}$ optimized wind turbines [%]. |
| $\xi_{\mathrm{P,row}}$ | Average power-loss fraction of a wind turbine row [%]. |
| $\rho$ | Air density $[\mathrm{kg/m^3}]$. |
| $\sigma_\theta$ | Wind direction standard deviation [°]. |
| $\tau$ | Current temperature. |
| $\tau_0$ | Initial temperature of component $j$. |
| $\tau_j$ | Current temperature of component $j$. |
| $\psi_{\mathrm{m}}$ | Emperically determined stability function [−]. |

# 1

# Introduction

## 1.1. Background

The wind energy share on the global electricity market has experienced a steady increase over the past few years. It is expected that the number of wind energy projects will grow even faster, during the coming years[1]. Due to fierce competition, many wind energy related research projects are currently aimed at reducing the Costs Of Energy (COE)[2–4]. In order to establish the cost reduction, more and more wind turbines are being clustered in (offshore) wind farms[5, 6].

Clustering wind turbines together has advantages compared to operation as separate entities. A reduction in land use can be established and the cost of installation and maintenance may be reduced, resulting from economies of scale[7, 8]. Major drawback of wind farms however, is the energy production loss due to aerodynamic wake interaction between the wind turbines[3, 5, 7]. Experience has shown that energy losses caused by wake effects amount to roughly $10-20\%$, in conventional offshore wind farms[9–11].

## 1.2. Problem analysis

Wind turbines on the market nowadays are designed with a "greedy" attitude, which means that each wind turbine, individually, aims to generate maximum power[4]. Such a strategy works well for wind turbines operating as stand-alone machines, but not for wind turbines operating in a wind farm. The strategy is not suitable for wind farm operation, because it does not take into account the consequences of wake effects caused by operating wind turbine rotors.

Operating wind turbines at "sub-optimal" conditions can result in a higher accumulated wind farm power generation, than in case of operating at optimal conditions[12]. Sub-optimal conditions are created by reducing the axial induction factor of the rotors, yielding lower thrust and power coefficients. Lowering the thrust coefficient decreases the severity of the wake[5], resulting into higher power generation by downstream wind turbines. The above described strategy is followed by the investigated optimization problems in the current project.

## 1.3. Approach

The current project investigates optimization problems that manipulate the performance curves of wind turbines operating in a wind farm. The spacing between the wind turbines, rotor diameters and wind turbine hub heights remain fixed in the optimization problems. The optimization parameters are the axial induction factor curves of the wind turbines, which are converted to thrust coefficient and power curves by momentum theory.

The axial induction factor curve is either parametrized by discrete specification points, at rotor-averaged wind speed intervals of $|\Delta u_\infty| = 1\mathrm{m/s}$, or by Bézier control points. The optimization parameters are manipulated by Matlab's optimization toolbox, using built-in optimization algorithms. An optimization algorithm searches for the optimum axial induction factor curve, yielding the lowest energy losses caused by wake effects and resulting into maximum Annual Energy Production (AEP) of a wind farm.

A requisite of the optimization problems is the use of a wind farm simulation tool to estimate the AEP of a wind farm, for each evaluated set of optimization parameter values. As wake effects play a crucial role in the problems, the tool should be able to model flow in the wake of wind turbine rotors. As optimization runs require tens or hundreds of iterations before the solution converges into optimum design values, the software should preferably be non-computationally intensive in order to limit the time spent on calculations.

All wind farm simulations are performed with ECN's aerodynamic wind farm-wake simulation tool 'FarmFlow-fast', which solves the 3D steady parabolized Navier-Stokes equations in disturbance form. FarmFlow-fast is a quicker variant to the original 'FarmFlow'; especially developed for optimization purposes concerning the shorter calculation times. FarmFlow-fast is capable of calculating the power generation of free-stream wind turbines and wind turbines operating in the wake of other wind turbines. The power generation is calculated as function of the optimization parameters and the free-stream wind speed and direction. Next to the power generation, FarmFlow-fast calculates the reduced wind speed and increased turbulence intensity in the wake of wind turbine rotors.

Matlab is used to post-process simulation data and couples post-processed results back to the optimization toolbox. Different optimization problems and scenarios are investigated, all serving a specific purpose. Firstly, to obtain quantitative insight into the potential of energy production maximization by wind turbine performance curve optimization. Secondly, to explore how the optimum performance curves are influenced by changing the number of wind turbines, layout and wind climate of a wind farm.

Several steps are taken in the current research project, ultimately leading to an increase in AEP of a wind farm.

- First, the FarmFlow-fast model is validated for optimization purposes.
- Hereafter, a simplified wind farm optimization problem is defined to create the interface between Matlab's optimization toolbox and FarmFlow-fast.
- Once the coupling between the optimization toolbox and FarmFlow-fast is established, the performance of five different optimization algorithms are compared with each other on the simplified optimization problem.
- After the most suitable optimization algorithm is picked, a more comprehensive wind turbine performance curve optimization problem is defined. The performance curve optimization problem is used to compare different algorithm settings and parametrization methods with each other.
- Finally, when the best optimization methodology is known it is applied to three other optimization scenarios.

## 1.4. Objectives

The aim of the current project is:

*Obtain insight into the potential of wind turbine performance curve optimization for wind farm operation, by carrying out optimization runs with Matlab's optimization toolbox coupled to FarmFlow-fast.*

The project involves the accomplishment of two primary objectives. The first objective is the validation of FarmFlow-fast for the purpose of wind turbine performance curve optimization. The objective is achieved by comparing FarmFlow-fast simulation data with simulations of the original FarmFlow version and measurement data taken in two existing wind farms.

The FarmFlow-fast output parameters that are compared with the reference data are the power generation values of a wind turbine row, aligned with the wind direction. Simulations are performed for various rotor diameters, turbulence intensities, wind speeds, hub heights and spacings between the wind turbines. The influence of the wind direction is investigated and the calculation times of FarmFlow and FarmFlow-fast are compared with each other.

The second objective is to discover to what extent the energy production of a wind farm can be increased, by optimization of wind turbine performance curves. The objective is achieved by solving optimization problems with parametrized wind turbine performance curves, i.e. the thrust coefficient curve and the power curve.

The influence of the optimization algorithm type and settings on the optimum objective function value, parameter values and optimization time is investigated. Next to the influence of the algorithm, it is investigated how the optimum solution is affected by the performance curve parametrization method and the number of wind turbines in a wind farm. Finally, the contribution of the performance curves of free-stream wind turbines is examined.

An overview of the primary and secondary objectives is given below.

**Validation of the FarmFlow-fast software**

- Obtain insight into the quality of FarmFlow-fast simulations compared to FarmFlow simulation data and measurement data.
- Obtain insight into the calculation times of FarmFlow-fast and FarmFlow.
- Obtain insight into how the simulation quality is affected by the turbulence intensity, wind turbine spacing and wind speed and direction ranges.

**Optimization of wind turbine performance curves**

- Obtain insight into the influence of the optimization algorithm type and settings.
- Obtain insight into the influence of performance curve parametrization.
- Obtain insight into the influence of the number of wind turbines in a wind farm.
- Obtain insight into the contribution of the performance curves of free-stream wind turbines.

## 1.5. Outline of the report

The report is structured as follows.

- Chapter 2 starts with a general literature review about wake effects and provides a short overview of currently available aerodynamic wind farm simulation models. Wake model validation methods are briefly highlighted and the chapter summarizes what already has been done on wind farm optimization.
- Chapter 3 describes the capabilities, theory and models of FarmFlow-fast. Additionally, the differences with the original FarmFlow version are discussed.
- Chapter 4 presents the complete validation study of FarmFlow-fast. It explains the validation procedure and compares FarmFlow-fast simulation results with simulation data from the original FarmFlow version and measurement data.
- Chapter 5 illustrates the methodology of the investigated optimization problems including the governing equations, parametrization methods and objective functions. Additionally, the investigated optimization cases are described.
- Chapter 6 treats the results of all optimization runs and discusses the best optimization methodology and the potential of wind turbine performance curve optimization.
- Finally, Chapter 7 provides conclusions that are drawn from the project and gives recommendations for follow-up research.

# 2

# Literature review

## 2.1. Overview

This literature review is aimed at presenting a selection of topics related to wind farm aerodynamics and optimization. It mainly serves to demonstrate the research framework of the current study and the position of the current project within this framework. Besides the explanatory purpose, it serves to support the choices made during the project and to provide reference data for the validation study.

Section 2.2 begins with general characteristics of wake effects in wind farms. It explains causes and consequences of wake effects and highlights problematic areas, on which the current research is focussed. Hereafter, Section 2.3 presents currently available wind farm-wake models comprising a range of complexities. FarmFlow-fast is placed in perspective with other models, which supports the choice for using FarmFlow-fast in the optimization problems of the current project.

Section 2.4 treats the validation of wind farm-wake models by presenting a number of validation studies, using various procedures and reference data. The procedure for the current validation study is derived from the ones presented and is customized for the purpose of wind farm optimization. The reference data of the current validation study is amongst others subtracted from the described validation study sources. Finally, Section 2.5 discusses different types of wind farm optimization studies that have already been carried out. It clarifies the position and potential of wind turbine performance curve optimization for wind farm operation.

## 2.2. Wake effects

As stated in Chapter 1, the efficiency of a wind farm decreases due to aerodynamic interaction between its wind turbines. Wind turbines extract energy from wind by converting kinetic energy into mechanical energy. Due to the energy extraction, wind downstream of an operating wind turbine rotor contains less energy than in front of the rotor[13]. Next to the energy reduction, the turbulence intensity, $TI\,[\%]$, increases in the wake. The higher turbulence intensity causes an increase in blade loads on downstream wind turbines[13–15].

The effects of kinetic energy reduction and turbulence intensity increase are together called "wake-effects". Wake effects are most severe if the wind direction is aligned with the orientation of the wind farm and the wind turbines operate at maximum thrust coefficient, $C_\mathrm{T}\,[-]$. A closer wind turbine spacing, $\Delta s\,[\mathrm{m}]$, and a lower ambient turbulence intensity, $TI_\infty\,[\%]$, also amplify wake effects[5, 16]. As a result of the above mentioned relationships, wind turbines are preferably placed further away from each other in prevailing wind direction than in other directions. Atmospheric stability influences the severity of wake effects as well[11], but that influence is not covered in the current project.

Wake effects are most strongly represented in an offshore environment, because offshore ambient turbulence intensities tend to be lower than on land[17]. The lower turbulence intensity originates from the lower surface roughness and a generally more stable atmosphere than on land[16]. Wake effects are most noticeable along the wind direction in which wind turbines are located closest to each other and when wind turbines operate just below rated conditions ($u_\infty \sim u_\mathrm{rated}$). The region just below rated wind speed is the area where wind turbines generate maximum power and operate at the maximum thrust and thrust coefficient[18].

The focus of the optimization problems in the current project is on power generation losses and not on loads at wind turbine rotors. The power-loss fraction is defined as the relative loss in power generation, between a wind turbine exposed to free-stream meteorological conditions and a wind turbine in the wake of one or more other wind turbines[11, 19]. A formal definition of the power-loss fraction is given in Section 4.5.3.

The largest power generation reduction along a row of wind turbines occurs between the first and the second wind turbine. Additional wind turbines only marginally increase the power-loss fraction, compared to the power-loss fraction at the second wind turbine[19]. For a detailed review on rotor and wind farm aerodynamics along with the derivation of the governing equations, the reader is referred to [5].

## 2.3. Aerodynamic wind farm-wake models

Two distinguishable aerodynamic areas exist in wind energy technology; rotor aerodynamics and wind farm aerodynamics. Rotor aerodynamics solely focuses on the flow around one specific rotor, while wind farm aerodynamics involves the total flow in a wind farm[20]. Aerodynamic wind farm-wake models are capable of predicting the power-loss fraction along a row of wind turbine rotors. A wide variety of tools and models are available nowadays[5, 16, 20–22], each with a different level of parametrization and corresponding computational demands.

The complexity of both aerodynamic areas ranges from highly parametrized engineering models up to the most sophisticated Computational Fluid Dynamics (CFD) models. Engineering models transform complicated flow phenomena into transparent simplified equations, which are less computationally intensive to solve[20]. CFD models on the other hand, contain more physics and require more computational power. An overview of a range of different currently available models is given in [5].

An engineering model generally applies empirical tuning corrections to the simplified equations it is solving. Empirical data can be based on simulations performed by more sophisticated models, or on field measurements taken in existing wind farms[20]. The tuning corrections make it possible to compensate for deficiency of accuracy in comparison with CFD tools, while requiring the computational effort of an engineering tool.

A subdivision of wind farm aerodynamic tools can be made into three groups; engineering models, CFD models and intermediate models. A description of all three groups is given in the subsequent paragraphs.

**Engineering models** The first group consists of highly parametrized engineering models like the Park model[23, 24]. Simplified analytic equations are solved and wind turbines are modelled as permeable actuator disks. A positive characteristic of engineering models is that a complete wind farm assessment can be performed in a matter of seconds. Major drawbacks of engineering models are that results are generally only valid in the far wake region and the influence of most atmospheric parameters is not taken into account[16, 22]. Models in the engineering category can be used for a quick initial design assessment, but if more detail is required and the influence of atmospheric parameters has to be taken into account, the models are not accurate enough.

Examples of models belonging to the engineering category are the Park model [23, 24] and the Wind Atlas Analysis and Application Program (WAsP) model [25] of the Risø Technical University of Denmark (DTU) National Laboratory. Both models are based on an approximate solution of the boundary layer equations by neglecting the pressure term. A circular symmetric wake deficit profile is assumed and a similarity assumption for the shape of the wake deficit is adopted. The estimated wake deficit is superimposed on the undisturbed wind shear field, which yields the resulting downstream mean wind profile.

**CFD models** Secondly, there are the sophisticated CFD models that completely model the near and far wake. CFD models fully resolve the Navier-Stokes equations, including the elliptic terms. CFD solvers are capable of implementing actuator line wind turbine models, which are more realistic than actuator disk models.

CFD tools are in general the most accurate category of simulation tools. The models involve the highest degree of physics, which implies that a single wind farm assessment can take several days to weeks on a cluster of processors[22]. CFD models can be best used if small scale, detailed scenarios need to be simulated or when the influence of rarely occurring atmospheric parameters is investigated. If more general simulations are required as in case of AEP estimation, less sophisticated quicker models might be more appropriate.

An example of a tool belonging to the CFD category is the Simulator for Offshore Wind Farm Applications (SOWFA)[26]. SOFWA is developed by the National Renewable Energy Laboratory (NREL) and is based on the OpenFOAM CFD toolbox[27]. The tool includes aero-elastic actuator line wind turbine models and solves the Large Eddy Simulation (LES) Navier Stokes equations. A Sub-Grid Scale (SGS) model is used near the surface of the Atmospheric Boundary Layer (ABL)[28]. Another model in the CFD category is the fully elliptic turbulent 3D Navier-Stokes numerical solver (3D-NS) from the Robert Gorden University[29].

**Intermediate models** The third group is formed by models of intermediate complexity, based on parabolized Navier-Stokes equations[20]. The Navier-Stokes equations are parabolized by neglecting the axial pressure gradient in the wind turbine wakes. Neglecting the axial pressure gradient is only a valid assumption in the far wake region. A correction should be applied in the near wake, which can be done in different ways as explained in [20].

Parabolized equations are less computationally intensive than full Navier-Stokes equations, since all elliptic terms have disappeared[22]. Intermediate models can still be categorized as engineering models, but the results are generally more accurate than the Park model and the like[16]. Parabolized models are generally not applicable in the near wake region due to neglecting the pressure gradients, which are responsible for the deceleration and expansion of the flow. Wind turbines are modelled as permeable actuator disks in intermediate models.

An example of a model belonging to the intermediate category is Windfarmer[30, 31], which is developed by Garrad Hassan. Windfarmer is an axis-symmetric CFD Navier-Stokes solver with eddy-viscosity closure. The model is initiated at a distance of $x = 2D$ behind the wind turbine rotors, by an empirical wake profile. The initial profile is of Gaussian shape and varies with thrust coefficient and ambient turbulence intensity. The eddy-viscosity is defined by using the turbulence intensity in the wake.

Another example is the Farm Layout Program (FLaP) model[17, 32] from the University of Oldenburg. FLaP is a two-dimensional, axis-symmetrical model that also solves the momentum and continuity equations with an eddy-viscosity closure. The eddy-viscosity is modelled as a combination of contributions from ambient turbulence intensity and shear-generated turbulence in the wake.

The FLaP wake model is initiated at the end of the near wake, with an empirical wake profile as boundary condition. The near wake length is calculated with the model of Vermeulen [33] taking into account ambient, rotor-generated and shear-generated turbulence intensity. The average turbulence intensity in the wake is calculated from the modelled eddy-viscosity.

ECN's FarmFlow and FarmFlow-fast also belong to the intermediate category. Contrary to other models in the intermediate category, FarmFlow and FarmFlow-fast also include the near wake region by prescribing the forces of the neglected pressure gradients. A description of both models is provided in Chapter 3.

Before choosing a specific wind farm simulation tool, a trade-off should be made based on the purpose and character of the simulations one wants to perform. For accurate annual energy yield prediction of a wind farm with a fixed design, the major concern is that the average power generation calculations correspond with reality. For such an investigation, one should preferably use a model with a physics content in the governing equations as high as in the available wind climate data. Calculation time is less important, because the simulations need to be performed only once.

If on the other hand many design alternatives have to be analysed, for instance during optimization processes, the computing time of the tool becomes an important factor. The extent and complexity of the physics in the governing equations should be fine-tuned with the focus of optimization problem. An optimum balance has to be found between the computational effort and accuracy of the simulation model, for each research purpose.

The studies [16, 21, 22] describe and compare models of different complexities. From the reports, it is concluded that a model from the intermediate category is the only valid option for performing wind turbine performance curve optimization studies. Especially if many design evaluations have to be performed and site conditions like the Weibull distribution and the turbulence rose need to be taken into account. Once the optimum performance curves are known, a more sophisticated model can be used to validate the results of the intermediate model.

## 2.4. Wake model validation

The quality of a wind farm-wake simulation tool has to be approved, before it can be used for any research purpose. Although CFD tools are more sophisticated than engineering models, it does not imply that CFD tools provide better results for every intended application of the tool. Validation of a simulation tool is required to demonstrate that the tool produces acceptable results.

The intended research purpose determines the nature and extent of a validation study, although general guidelines on the analysis of wind farm wakes are given in [19]. The required data for a wind farm-wake validation study is the wind farm layout, wind turbine specifications and the wind climate[16, 34]. For validation of wind farm-wake models using empirical data to tune its calculations, it is important that the validation runs are performed in at least one wind farm that has not been used for the tuning.

The validation study [18] validates results of the Park model, Larson model[35] and Fuga[36] with power generation measurement data from the Horns Rev and Lillgrund offshore wind farms. Power generation data obtained within a specific wind speed and direction range is subtracted, from which the average power-loss fraction per wind turbine is calculated. The power-loss fraction of a single-wake wind turbine, as function of free-stream wind direction is also calculated. All measurement data is compared with corresponding simulation data, generated by the investigated simulation tools.

The study [16] compares the average vertical wind profiles in the wake of a free-stream wind turbine rotor, for five different wake models. Simulation data is compared with SOnic Detection And Ranging (SODAR)[37] profiles, measured in the Vindeby offshore wind farm. Small wind speed, wind direction and turbulence intensity ranges are taking into account and multiple distances in the wake from the wind turbine rotor are concerned.

Finally, [38] focusses especially on the turbulence profiles and vertical velocity profiles behind free-stream wind turbines. The average axial wind speed deficit along a wind turbine row is also investigated. Simulations of different engineering models and more sophisticated models are compared with measurement data taken in the Prettin and Colorado Green wind farms. Next to wind farm data, wake measurements from the Netherlands Organisation for Applied Scientific Research (TNO) wind tunnel are used for the validation study.

Instead of subtracting all power generation data within a range of wind speeds and wind directions, other data classifications can be made. For example, [11] subdivides the measurement data in turbulence intensity ranges and atmospheric stability classes. The data classification can be made as specific as the user wants, however [19] recommends that at least 30-60 minutes of measurement data should be available for each flow case. Additionally, the flow case can be such specific that either the measurement devices in the wind farm or the simulation software is not precise enough to guarantee the quality of the results.

For the FarmFlow-fast validation study in the current project it is important that relative power generation losses of wind turbines in a wind farm are adequately calculated. The high accuracy of the power-loss calculations is required, since the focus of the optimization problems is on increasing energy production by reducing wake effects in a wind farm. As the simulations are used for AEP calculations, the simulation scenarios are based on ordinary atmospheric conditions.

It is important that the influence of the wind speed and direction, ambient turbulence intensity, wind turbine spacing and hub height is taken into account. Besides the accuracy and amount of required physics in the model, the calculation time is important since the tool is used for optimization purposes. The optimization purpose implies that many design alternatives have to be analysed before the final solution is known.

Based on the above mentioned requirements, it is concluded that the FarmFlow-fast validation study should investigate relative power generation losses of wind turbines in a wind farm. The power generation losses should be compared with reference data for scenarios comprising different wind speeds and directions, ambient turbulence intensities, wind turbine spacings and hub heights. Meanwhile, the calculation time of the tool has to be monitored in order to judge whether FarmFlow-fast performs quick enough.

## 2.5. Wind farm optimization

Minimizing the cost of wind energy can be a complicated optimization problem, because many factors contribute to the costs. Theoretically, a minimization cost function can be derived taking all variables and constraints into account. Such a minimization problem would however become too complicated to solve in an acceptable time frame, with currently available computing resources. Simplified cost functions can be made up, which are easier to solve. The cost functions are simplified by fixing parameter values or making parameters dependent by using mathematical relations.

An implicit issue of every wind farm optimization problem is that a trade-off has to be made between on the one hand increasing the power generation of the wind farm, but on the other hand decreasing the investment and Operation & Maintenance (O&M) costs. Many variables can be chosen to optimize for; some optimization parameters to consider are the locations, type, size and height of the wind turbines. Constraints and boundary conditions are found in the design of the electrical collector system, the location of the wind farm, environmental & regulation constraints and constructibility[2, 39].

At the time of writing, wind farm design is carried out as follows. First, a windy area is selected to site a wind farm. At this location, a wind resource assessment is carried out to obtain the wind speed and direction distributions. Hereafter, the meteorological data is used for estimating the energy that can potentially be produced over the wind farm's lifetime. The type, number and locations of the wind turbines are afterwards determined by taking into account the prevailing wind direction, the design of the electrical cable infrastructure, geographic features of the environment and other boundary conditions.

Optimization studies focussing on wind farm layout optimization have been carried out. Amongst the layout optimization studies different approaches were used concerning objective functions, optimization parameters, algorithms and wake models. For example, [40] and [41] focus on the maximization of the Net Present Value (NPV) of wind energy by changing the locations, hub heights and rotor diameters of wind turbines in a wind farm. The used optimization algorithm is an evolutionary algorithm called "differential evolution"[42]. Wind turbines are modelled as permeable actuator disks and the Park model[23, 24] is used for power generation calculations.

Optimization studies [2] and [3] on the other hand, solely focus on maximizing the wind farm's power generation. The problems selected the wind turbine locations as optimization parameters; the number of wind turbines and the wind turbine types have remained fixed. An evolutionary algorithm and the Park wake model were used again, similar to the previously mentioned optimization studies. All four optimization studies have taken the wind rose and Weibull distribution into account, but economical factors have been disregarded.

Another strategy is to optimize wind turbine performance parameters, while keeping the layout of the wind farm fixed. Such an investigation has been performed by [4] and [43]. The optimization problems focus on maximizing the instantaneous power generation of a wind farm, by varying the axial induction factor of actuator disk wind turbine models. The Park model was used again and also this time the evolutionary global optimization algorithm has been used.

The studies [7, 44, 45] focus on power maximization by axial induction factor optimization as well. These studies use the Park model too, but now a local gradient-based optimization algorithm has been used. The gradient-based optimization algorithm has shown to converge quicker than the global evolutionary algorithms, although not always to the global optimum. Finally, reports [8] and [46] focus on the same optimization problem, but propose to validate the results with more sophisticated wind farm simulation software.

From the above mentioned optimization studies, it is concluded that most wind farm optimization problems have focussed on wind farm layout optimization. Power maximization by wind turbine performance curve optimization has yet only been performed on a relatively small scale and only with the intention to improve the control system of existing wind turbines. Power maximization studies have shown that the instantaneous power generation of an existing wind farm can potentially be increased in the order of a few percent[4][45]. The increase was solely achieved by using performance parameters optimized for wind farm application, instead of focussing on wind turbine scale.

Common features of all the optimization studies described in the current section are the use of an engineering model for wind farm simulations. Using more sophisticated wake models for wind farm calculations has not yet been performed, according to the author's knowledge. The use of engineering models might be a consequence of using the evolutionary global optimization algorithm in the optimization problems. Global optimization algorithms require a large amount of function evaluations, before the solution converges into optimum design values.

Using a more advanced wake model and a less complex algorithm for wind farm optimization problems might be a combination that brings about new insights. Instead of instantaneous power maximization by means of wind turbine control optimization, the focus of the optimization problem can also be on the design of new rotor concepts; especially developed for wind farm operation. The last mentioned strategy has not yet been used, as far as the author is aware.

# 3

# FarmFlow-fast: Theory and methodology

This chapter provides the theoretical description and methodologies of the aerodynamic wind farm-wake simulation tool FarmFlow-fast. It starts with a general description of the software and its capabilities, in Section 3.1. Hereafter, the models used for simulating the ABL, the wind turbine power generation and the behaviour of the wakes are discussed in Section 3.2. Finally, Section 3.3 explains the differences between the original FarmFlow version and FarmFlow-fast.

## 3.1. Tool description and capabilities

FarmFlow-fast is a wind farm-wake simulation tool especially developed for optimization purposes. It is a quicker variant of the original FarmFlow version. The software calculates the power generation, $P[\mathrm{kW}]$, of each wind turbine in a farm for a specified flow case. Next to the power generation, FarmFlow-fast calculates the increased turbulence intensity in the wake of wind turbine rotors, $TI[\%]$, and the reduced rotor-averaged wind speed, $u_\infty[\mathrm{m/s}]$, for a wind turbine operating in the wake. The free-stream wind directions, $\theta_\infty[^\circ]$, wind speeds, $V_\infty[\mathrm{m/s}]$, and turbulence intensities, $TI_\infty[\%]$, can be specified by the user.

By running sufficient representative simulations, it is possible to estimate the AEP for a given wind farm layout and wind climate. This however requires post-processing by integrating the power generation data over a year, according to the wind climate. The same holds for the calculation of the energy-loss fraction over a range of wind speeds and directions.

The required input data of the FarmFlow-fast tool is summarized below. The input data can be obtained from wind farm assessment reports, wind turbine brochures and met-mast data.

### Wind farm layout

- Locations of the wind turbines $(x_\mathrm{i}, y_\mathrm{i})\ [\mathrm{m}]$.
- Type of wind turbines (Not necessarily all the same).

### Wind turbine data (for every wind turbine type in the wind farm)

- Hub height $z_\mathrm{hub}[\mathrm{m}]$ and rotor diameter $D[\mathrm{m}]$.
- Tip-speed ratio $\lambda[-]$ and maximum tip speed $V_\mathrm{tip,max}[\mathrm{m/s}]$.
- Power curve $P\,(u_\infty)\ [\mathrm{kW}]$.
- Thrust coefficient curve $C_\mathrm{T}\,(u_\infty)\ [-]$.

**Meteorological data**

- Weibull wind speed distribution for each wind direction sector (Parametrized by the scale parameter $A[\mathrm{m/s}]$ and shape parameter $k[-]$).
- Wind rose; probability of occurrence per wind direction $p\left(\theta_{\infty}\right)[\%]$ or probability of occurrence per wind speed and wind direction $p\left(V_{\infty}, \theta_{\infty}\right)[\%]$.
- Turbulence rose $\overline{TI}_{\infty}\left(V_{\infty}, \theta_{\infty}\right)[\%]$ (Average ambient turbulence intensity per free-stream wind speed and wind direction ranges).
- Average air density $\rho[\mathrm{kg/m^3}]$.

## 3.2. Description of the models

FarmFlow-fast forms a combination of five different models. It couples an ABL model, actuator disk rotor models and a near, a transition and a far wake model with each other. A general description of each model is given in Sections 3.2.1 to 3.2.5. For a detailed description and derivation of the governing equations, the reader is referred to [13, 47].

The wake model of FarmFlow-fast is called WakeFarm, which is based on the original UPMWAKE model proposed by Crespo[13, 48, 49]. Wakefarm estimates the wind speed profiles in wind turbine wakes by solving the 3D steady parabolized Navier-Stokes equations in perturbation form. If multiple wind turbines operating in either full-wake or partial-wake conditions are concerned, then the rotor-averaged wind speed is used as input for the performance curve lookup tables of the concerned wind turbine.

A $k-\epsilon$-turbulence model is used to simulate the turbulence[50]. The parabolized Navier-Stokes equations are discretized with central differences and are integrated by employing the semi-implicit Alternating Direction Implicit (ADI) scheme[51]. The pressure term is evaluated by using the Semi-Implicit Method for Pressure Linked Equations (SIMPLE) method[52]. Although parabolized, the near wake region is included by prescribing the forces of the neglected pressure gradients. The forces have been pre-calculated with a free-vortex wake model.

### 3.2.1. Atmospheric boundary layer

The ABL model is based on the logarithmic wind profile using the Monin-Obukhov similarity theory, as described in the Panofsky-Dutton model[53]. The diabatic vertical wind profile is calculated according to Equation (3.1).

$$u = \frac{u_{*0}}{\kappa}\left[\ln\left(\frac{z}{z_0}\right) - \psi_{\mathrm{m}}\left(\frac{z}{L}\right)\right] \tag{3.1}$$

In this equation, $u_{*0}[\mathrm{m/s}]$ represents the near-surface friction velocity, $\kappa[-]$ is the Von Kármán constant, $z[\mathrm{m}]$ is the height above the ground and $z_0[\mathrm{m}]$ represents the aerodynamic roughness length. $\psi_{\mathrm{m}}[-]$ is an empirically determined universal stability function[1], on which more details are provided by [53]. Finally, $L[\mathrm{m}]$ is the Monin-Obukhov length which is defined by the expression shown in Equation (3.2).

$$L = \frac{u_{*0}^3 T}{\kappa g \overline{w'\theta_0'}} \tag{3.2}$$

In Equation (3.2), $T[\mathrm{K}]$ represents the absolute temperature, $g[\mathrm{m/s^2}]$ is the gravitational acceleration, $w'[\mathrm{m/s}]$ is the fluctuating term of the vertical wind speed, $\theta_0[\mathrm{K}]$ the potential temperature and $\overline{w'\theta_0'}[\mathrm{K\cdot m/s}]$ gives the vertical turbulent heat flux.

---

[1] In the current version of FarmFlow-fast, a constant neutral atmospheric stability is assumed. As a result of this assumption, the influence of atmospheric stability on the performance of a wind farm can not be investigated with the tool.

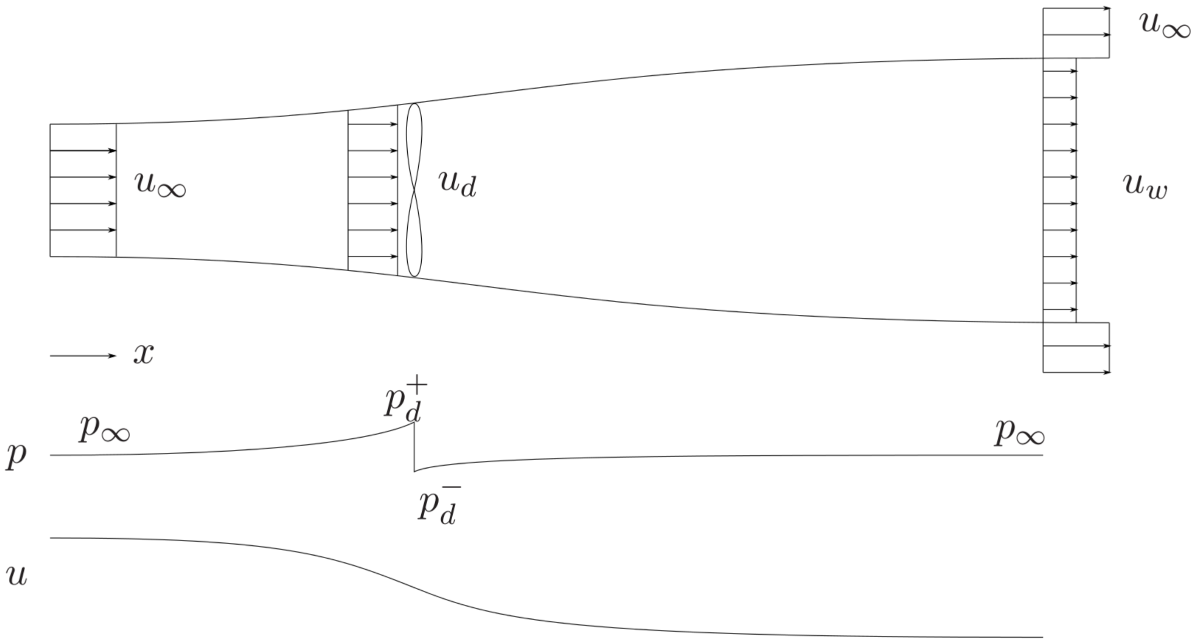

Figure 3.1: 1D flow through a stream tube containing an actuator disk[5]. Top: layout of the stream-tube with the actuator disk, middle: pressure distribution along the stream-tube, bottom: axial velocity distribution along the stream-tube.

### 3.2.2. Actuator disk rotor

Wind turbines are modelled as permeable actuator disks, which is one of the simplest models to represent a wind turbine rotor. As stated in Section 3.1, the behaviour of actuator disk wind turbines is specified by the power, thrust coefficient and rotor speed curves. If aerodynamic wind turbine losses are neglected, then the thrust coefficient curve and the power curve can be related to each other by momentum theory. Momentum theory is used in the optimization problems of the current project to reduce the number of optimization parameters.

A one dimensional flow without aerodynamic losses can be solved by a system of three equations; the continuity, the momentum and the energy equation. An illustration of a 1D flow through a stream tube containing an actuator disk, together with the development of the velocity and pressure profiles along the stream tube is displayed in Figure 3.1.

Momentum theory can be used to calculate the thrust coefficient by Equation (3.3) and the power coefficient with Equation (3.4). In these equations, $a[-]$ represents the axial induction factor at the rotor. The axial induction factor is defined as the axial velocity deficit of the flow through the actuator disk, $u_\mathrm{d}[\mathrm{m/s}]$, compared to the rotor-averaged upstream wind speed, $u_\infty[\mathrm{m/s}]$, as shown in Equation (3.5)[54].

$$C_\mathrm{T} = 4a\left(1-a\right) \tag{3.3}$$

$$C_\mathrm{P} = 4a\left(1-a\right)^2 \tag{3.4}$$

$$a = 1 - \frac{u_\mathrm{d}}{u_\infty} \tag{3.5}$$

The power generation of a wind turbine without aerodynamic losses can be calculated by Equation (3.6). In this equation $\rho\left[\mathrm{kg/m^3}\right]$ represents the average air density and $D[\mathrm{m}]$ is the rotor diameter. Equations (3.3), (3.4) and (3.6) assume that wind turbine rotors operate without blade-tip losses, hub losses and other aerodynamic losses. Correction factors can be applied on Equation (3.6) to generate more realistic power generation results as explained in [55].

$$P = \frac{1}{2}\rho u_\infty^3 \pi \left(\frac{D}{2}\right)^2 C_\mathrm{P} \tag{3.6}$$

### 3.2.3. Near wake

In the near wake, the forces of the pressure gradients are prescribed in the Navier-Stokes equations. The forces are pre-calculated with a free-vortex wake model[56]. The near wake is represented by discrete axisymmetric constant vortex rings. Inviscid potential flow is assumed and stream-wise diffusion and turbulent mixing are neglected. Behind the near wake, the pressure gradients are zero and no forces are prescribed any more.

The actuator disk concept implies that strong helical tip vortices in the near wake region are neglected. In practice, the velocity reduction in the wake is initially preserved by induced flow from helical tip vortices. Simulation results of a wake behind an actuator disk, using disturbance equation-modelling with a $k-\epsilon$-turbulence model, show high production of turbulent kinetic energy already at the edge of the actuator disk. It is a known problem that these type of models produce unrealistically high turbulence levels in the near wake region of wind turbine rotors.

Neglecting helical tip vortices causes an overestimation of the wake recovery in the near wake. The $k-\epsilon$-turbulence model parameters are adjusted in the near wake to compensate for the overestimation of the wake recovery rate. The adjustment is based on measurements from ECN's research wind farms and the Horns Rev wind farm[57].

With the actuator disk assumption, the undisturbed flow in radial and tangential directions are assumed to be zero. This means that flow information is only travelling downstream. Under these assumptions, the Navier-Stokes equations that describe the flow can be written in parabolized form. In the parabolized form, the elliptic terms of the Navier-Stokes equations are not present any more[13].

The pressure gradient in flow direction is negative in the near wake. This causes the axial velocity deficit to increase at the rotor center, resulting in a velocity deficit with a hat-shaped profile. The length of the near wake region is approximately $x_{\mathrm{iw}} - x_{\mathrm{nw}} \approx 2.5D$ rotor diameters for an ambient turbulence intensity of $TI_{\infty} \sim 4\%$. The near wake region becomes shorter with increasing turbulence intensity[47].

### 3.2.4. Transition wake

Atmospheric turbulence and vortex-vortex interaction causes the helical tip vortex structure to slowly destabilize. After some distance $x \sim 1D$ downstream the actuator disk, the helical tip vortex structure starts to break down. The flow transforms into a turbulent flow structure, which accelerates the wake recovery. A region of strong turbulent mixing arises, in which the hat-shaped velocity deficit profile transforms towards a Gaussian-shaped profile with evenly distributed turbulence. A region of fast wake recovery originates, which is underestimated by both the standard $k-\epsilon$-turbulence model and the adapted $k-\epsilon$-turbulence model of the near wake.

To improve the results of the wake model, the wake is divided into three regions corresponding to the processes described above. Between the near wake and the far wake region a transition region with a length of $x_{\mathrm{fw}} - x_{\mathrm{iw}} \approx 2D$ is introduced, as shown in Figure 3.2. The transition wake model uses an adapted $k-\epsilon$-turbulence model that accelerates wake recovery in the transition region[47].

### 3.2.5. Far wake

The flow in the far wake is simulated by solving the 3D steady-parabolized Navier-Stokes equations in disturbance form. This means that the far wake is solved by subtracting the Navier-Stokes equations of the undisturbed flow from the equations behind the rotor. The stream-wise pressure gradient is neglected in the far wake region to remove the elliptic parts of the equations. Turbulence is almost evenly distributed and the velocity deficit profile has a Gaussian shape. The standard $k-\epsilon$-turbulence model is used in the far wake.

A set of seven equations is solved including the continuity equation, the momentum equation in three directions, the energy equation, an equation for the turbulent kinetic energy and an equation for the dissipation rate of turbulent kinetic energy. The latter two equations are used for closure of the model[13].

## 3.3. Differences between FarmFlow and FarmFlow-fast

Two different FarmFlow versions exist. The original version, 'FarmFlow', has already been validated in [47]. The more recently developed quicker version called 'FarmFlow-fast' however, has not yet proven the quality of its performance.

The difference between FarmFlow-fast and the original version is found in the coarseness of the

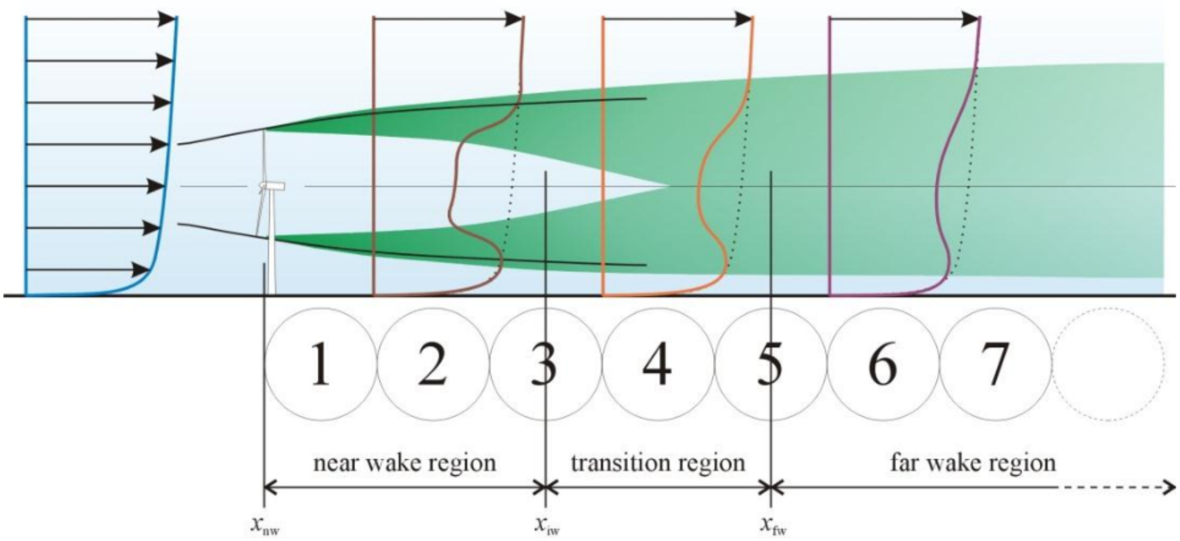

Figure 3.2: Development of the vertical velocity profile downstream of a wind turbine rotor and the distinction between the different wake regions[47].

grid. The grid cells of FarmFlow-fast are 12 times as big as the grid cells in the original version; three times in stream-wise direction and two times in the directions perpendicular to the flow direction.

The original version uses $96 \times 96$ cells in the rotor plane as shown in Figure 3.3, while FarmFlow-fast uses $48 \times 48$ cells. The original version starts with cell lengths of $|\Delta x| = 0.005D$ in axial direction, which increases exponentially up to the next wind turbine rotor or if the maximum step size of $|\Delta x| = 1D$ is reached after $\Delta s = 20D$. The coarser grid speeds up the calculation about 20 times[58], but requires different parameters for the $k - \epsilon$-turbulence model in the near wake region.

As discussed in Section 3.2.3, the prediction of turbulence is improved by tuning the parameters of the $k - \epsilon$-turbulence model in the near wake region. The effect of this tuning is very sensitive to the grid dimensions. Tuning parameters of a near wake turbulence model are only valid for the chosen grid dimensions. Changing the grid size requires the parameters of the $k - \epsilon$-turbulence model in the near wake to be re-tuned.

The original version of FarmFlow can be used for the most accurate results and FarmFlow-fast for quicker simulations. Both versions use their own tuning parameters for the $k - \epsilon$-turbulence model in the near wake. More info about the original version of FarmFlow, along with a description of the computational domain can be found in [47].

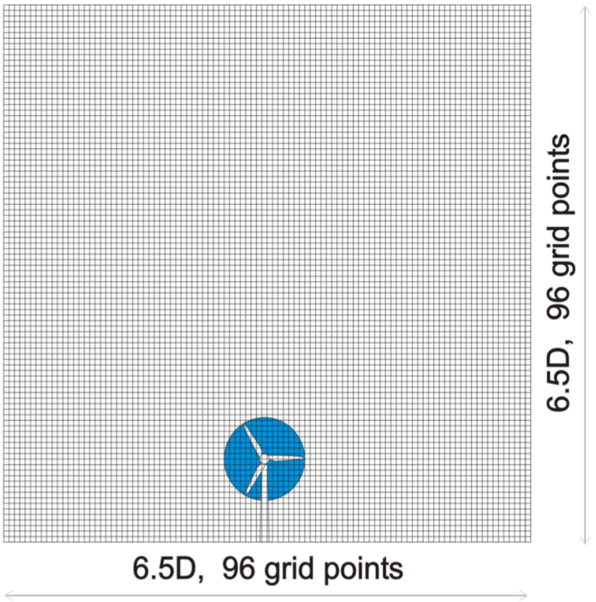

Figure 3.3: 2D computational domain of the original FarmFlow version[47].

# 4

# Validation of FarmFlow-fast

This chapter presents the FarmFlow-fast validation study. Section 4.1 starts with a brief description of the validation approach. The characteristics of the Horns Rev and Lillgrund wind farms, used for the validation cases are presented in Section 4.2. Hereafter, the wind climate used for post-processing of the simulation data is given in Section 4.3. The validation cases and the post-processing steps applied to FarmFlow-fast simulation results are provided in Sections 4.4 to 4.6. Finally, Section 4.7 discusses the results of the validation cases, by comparing simulation data with measurement data.

## 4.1. Validation approach

The purpose of the FarmFlow-fast validation study is to demonstrate that the tool is suitable for optimization purposes. The optimization purpose implies that FarmFlow-fast should simulate as quick as possible, while still producing acceptable results. As a result of the above mentioned requirements, not only the quality of the simulation results is investigated, but also the computation time of the tool is evaluated. Since FarmFlow-fast is a quicker variant of the original FarmFlow, the computation time is compared with the original FarmFlow version.

As explained in Section 3.3, FarmFlow-fast is quicker than the original FarmFlow version due to the coarser grid on which the wakes are modelled. Downside of the coarser grid is that the discretization error grows, which might lead to quality loss of the simulation results. The previous statements suggest that there should be a minimum grid size at which the tool simulates the quickest, while it still produces acceptable results. A grid convergence study is however not carried out for the FarmFlow model. Such a study is not possible due to the empirical nature of the near wake and the required grid-dependent tuning of the $k-\epsilon$-turbulence model parameters.

To obtain quantitative insight into the performance of FarmFlow-fast, simulation data of the software is compared with measurement data taken in existing wind farms. The measurement data consists of power generation measurements per wind turbine, as function of free-stream wind direction and wind speed, $P_\text{i}\left(\theta_\infty, V_\infty\right)$. A selection is made in power generation measurement data belonging to restricted wind speed and direction ranges.

For each discrete wind speed/direction combination within the selected wind speed/direction range, a simulation is performed in FarmFlow-fast and in the original FarmFlow version. The weighted average power generation is calculated from the simulations in the selected range, based on the wind rose and Weibull distributions. The weighted averages of both FarmFlow versions are compared with each other and with measurement data.

The described procedure is followed for two wind farms, from which different wind turbine and wind speed/direction combinations are chosen. The variety of validation cases makes it possible to investigate the influence of the wind direction, wind speed, ambient turbulence intensity, wind turbine spacing, rotor diameter and other parameters on the quality of the results. In the current validation study, the broad spectrum of scenarios is chosen to prove that FarmFlow-fast can be applied to a wide variety of wind farms.

The site layout, wind turbine characteristics, meteorological data and power generation measurements of the Horns Rev and Lillgrund offshore wind farms are used for the validation cases. Measure-

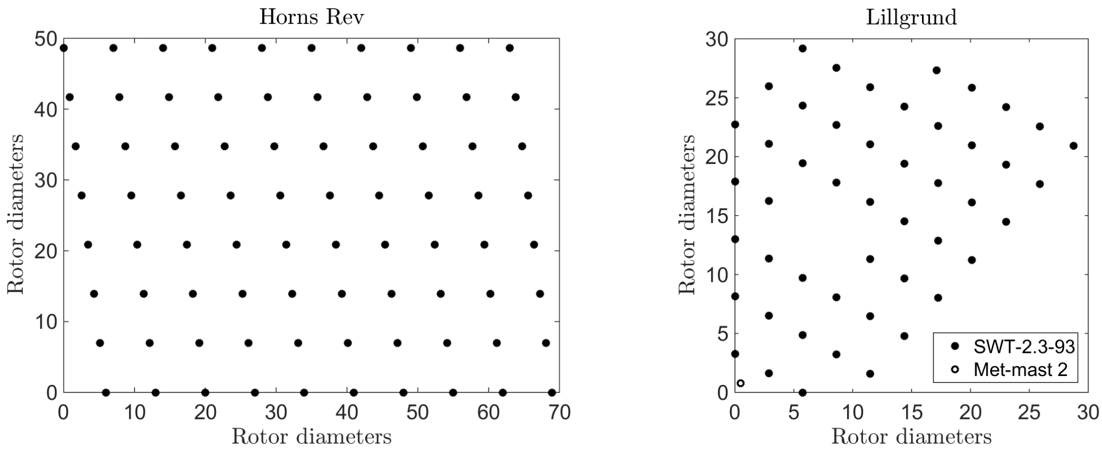

Figure 4.1: Layout of both concerned wind farms. Left: Horns Rev, right: Lillgrund.

ment data is obtained from multiple sources and most of the data has already been used in validation studies of other wind farm aerodynamic simulation tools[11, 34]. The wind farm data can be used to set up a validation study for any wind farm-wake model.

Besides validation of a wind farm-wake model, the meteorological data can be used to estimate a wind farm's AEP. Estimation of the AEP can for example be necessary in optimization studies as explained in Chapter 5.

## 4.2. Wind farm description

As stated previously, measurement data of the Horns Rev and Lillgrund wind farms is used to validate the results of FarmFlow-fast. The characteristics of both wind farms, relevant to the current validation study are described in the upcoming paragraphs.

**Horns Rev** The Horns Rev wind farm is located 14 kilometers from the west-coast of Denmark and consists of 80 Vestas V80[59] wind turbines. The wind farm is structured in a regular array of 8 by 10 wind turbines[11], as shown at the left side of Figure 4.1.

The Vestas V80 has a rotor diameter of $D = 80\text{m}$, a hub height of $z_{\text{hub}} = 70\text{m}$ and a rated power of $P_{\text{rated}} = 2.0\text{MW}$[18, 59]. The tip-speed ratio is $\lambda = 8.0$ and the maximum tip speed is $V_{\text{tip,max}} = 72\text{m/s}$. The power curve and thrust coefficient curve of the Vestas V80 are shown in Figure 4.2[1].

**Lillgrund** The Lillgrund wind farm is located 10 kilometers away from the south-western coast of Sweden, between Copenhagen and Malmö, and consists of 48 Siemens SWT-2.3-93[61] wind turbines. The wind turbine ordering is less structured than the Horns Rev wind farm. Besides the difference in wind turbine ordering, the relative spacings between wind turbines are smaller as shown at the right side of Figure 4.1.

The Siemens SWT-2.3-93 has a rotor diameter of $D = 92.6\text{m}$, a hub height of $z_{\text{hub}} = 65\text{m}$ and a rated power of $P_{\text{rated}} = 2.3\text{MW}$[18]. The tip-speed ratio is $\lambda = 8.5$ and the maximum tip speed is $V_{\text{tip,max}} = 78\text{m/s}$. The power curve and thrust coefficient curve of the Siemens SWT-2.3-93 are displayed in Figure 4.3[1].

---

[1] The black circles in Figures 4.2 and 4.3 represent the data points implemented in FarmFlow-fast. The black lines are constructed from interpolation between the implemented data points. The interpolation is performed according to the Piecewise Cubic Hermite Interpolating Polynomial (PCHIP) method[60]. The same interpolation method is used by FarmFlow-fast.

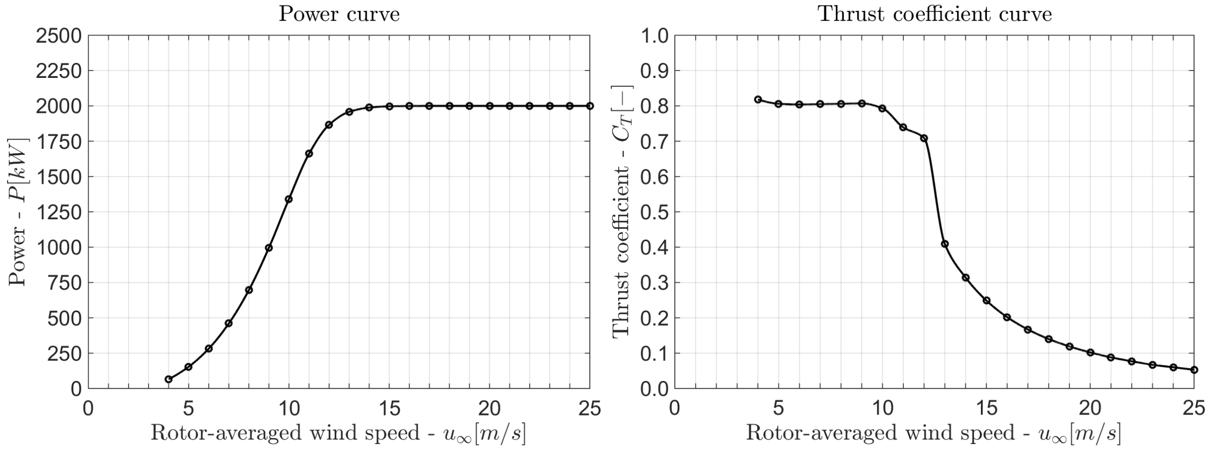

Figure 4.2: Performance curves of the Vestas V80[11]. Left: power curve, right: thrust coefficient curve

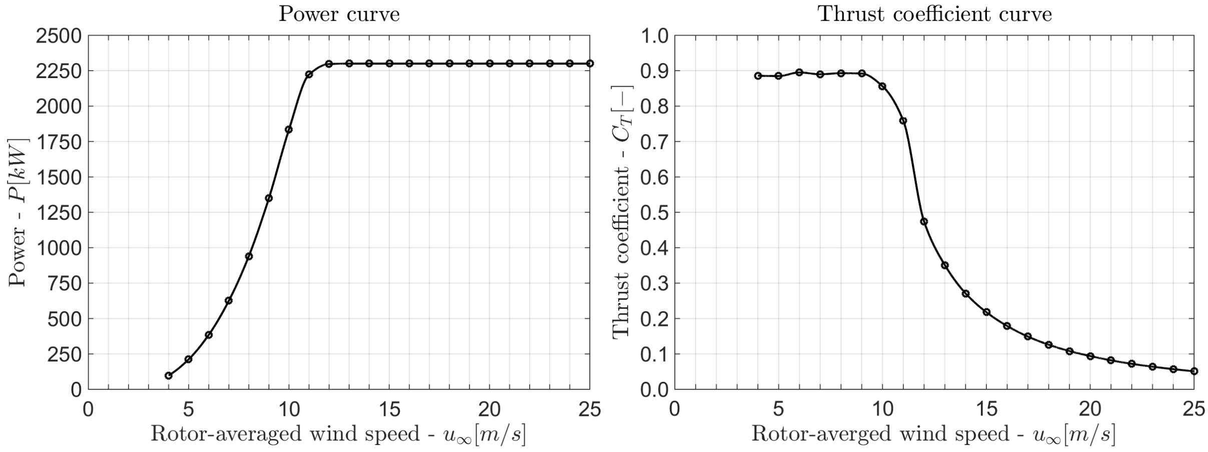

Figure 4.3: Performance curves of the Siemens SWT-2.3-93[61]. Left: power curve, right: thrust coefficient curve.

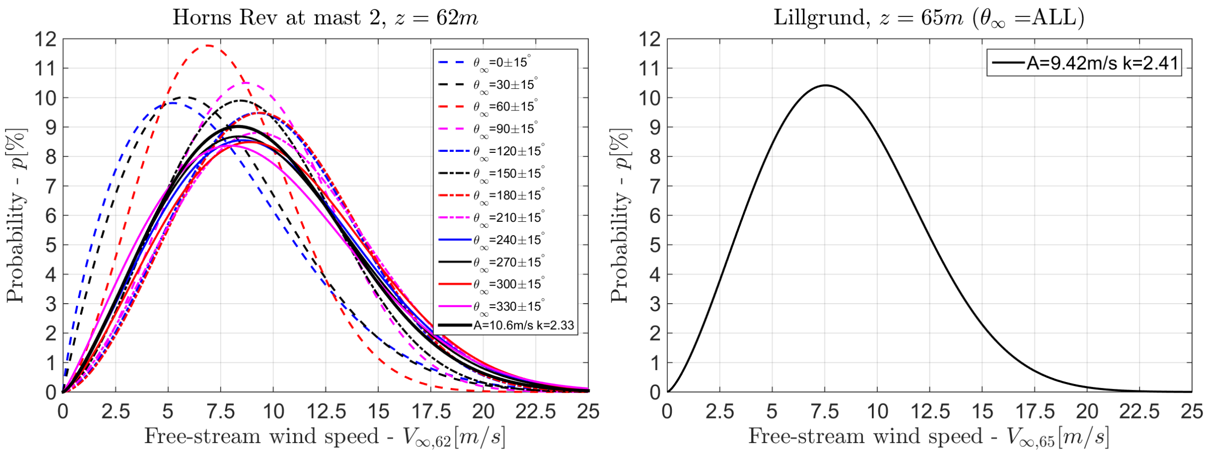

Figure 4.4: Weibull wind speed distributions of both wind farms. Left: Horns Rev, measurement period: *January 1, 2005 - December 31, 2007*. Right: Lillgrund, measurement period: *September 1, 2003 - February 28, 2006*. The thick black line in the left graph represents the averaged Weibull distribution over all wind directions.

## 4.3. Wind climate data

### 4.3.1. Weibull distribution for both wind farms

The Weibull wind speed distributions of both concerned wind farms are displayed in Figure 4.4. Wind direction bins of $|\Delta\theta_\infty| = 30^\circ$ are used for Horns Rev[2], while the Weibull distribution is assumed to be uniform over all wind directions in the Lillgrund wind farm[62]. The scale parameter, $A[\mathrm{m/s}]$, and the shape parameter, $k[-]$, are indicated in both graphs for the averaged Weibull distributions. From the graphs it is concluded that the average wind speed is higher in the Horns Rev wind farm than in the Lillgrund wind farm.

### 4.3.2. Horns Rev - Wind rose and turbulence rose

The Weibull scale and shape parameter values, average free-stream wind speed and wind power density, along with the corresponding frequency of occurrence per wind direction sector are displayed in Table 4.1. This data represents the wind rose of Horns Rev, which is extracted from the WAsP database. WAsP is the wind energy industry standard PC software for bankable wind resource assessment and siting of wind turbines and wind farms[63].

The turbulence rose is obtained from turbulence intensity measurements shown in Figure 4.5. The measurements were taken within the period *May 15, 1999 - May 14, 2002* from met mast 2, which is located north-west of the wind farm. The period of the turbulence intensity measurements does not correspond with the measurement period of the WAsP database.

Despite the difference in measurement period, the turbulence intensity measurements are taken at the same height as the wind speed and direction measurements; $z = 62\mathrm{m}$. This in contrast to the measurements of masts 6 and 7 located east of the wind farm, which measure at hub height; $z_{\text{hub}} = 70\mathrm{m}$. In addition to the corresponding measurement heights, the measurements in Figure 4.5 represent undisturbed meteorological conditions from all directions. The meteorological conditions are undisturbed, because the measurements were taken before the wind farm was installed. It is assumed that the measurement period is long enough to also be representative for the operational period.

The turbulence intensity measurements show that turbulence intensity is minimal around rated wind speed and increases with lower and higher wind speeds. The turbulence intensity is higher from northern and western directions than from southern and eastern directions. The Horns Rev flow cases in the validation study only consider westerly wind directions and wind speeds in the $7 < V_\infty \leq 9\mathrm{m/s}$ range. Due to the limited wind speed and wind direction ranges, a constant ambient turbulence intensity of $TI_\infty = 7\%$ is assumed for all Horns Rev validation cases.

---

[2] The Weibull distribution of Horns Rev originates from the WAsP database, which is based on measurements taken at met mast 2. This met mast is located north-west of the wind farm and has a measurement height of $z = 62\mathrm{m}$.

Table 4.1: Wind resource at Horns Rev met mast 2; anemometer height: $z = 62\mathrm{m}$. Measurement period: *January 1, 2005 - December 31, 2007*.

| $\boldsymbol{\theta}_\infty[\pm\mathbf{15}^\circ]$ | $\mathbf{A}[\mathrm{m/s}]$ | $\mathbf{k}[-]$ | $\overline{\mathbf{V}}_{\infty,\mathbf{62}}[\mathrm{m/s}]$ | $\overline{\mathbf{WPD}}_{\mathbf{62}}[\mathrm{W/m^2}]$ | $\mathbf{p}[\%]$ |
|---:|---:|---:|---:|---:|---:|
| 0 | 8.2 | 1.80 | 7.33 | 516 | 5 |
| 30 | 8.4 | 1.94 | 7.43 | 494 | 4 |
| 60 | 8.5 | 2.47 | 7.54 | 418 | 5 |
| 90 | 10.3 | 2.72 | 9.19 | 709 | 7 |
| 120 | 11.1 | 2.63 | 9.90 | 904 | 10 |
| 150 | 10.3 | 2.53 | 9.15 | 735 | 8 |
| 180 | 11.2 | 2.66 | 9.91 | 901 | 8 |
| 210 | 11.4 | 2.48 | 10.12 | 1006 | 11 |
| 240 | 11.0 | 2.28 | 9.72 | 953 | 12 |
| 270 | 10.8 | 2.27 | 9.59 | 918 | 10 |
| 300 | 11.3 | 2.34 | 9.99 | 1011 | 11 |
| 330 | 10.7 | 2.13 | 9.50 | 944 | 9 |
| **Average** | 10.6 | 2.33 | 9.41 | 849 | 100 |

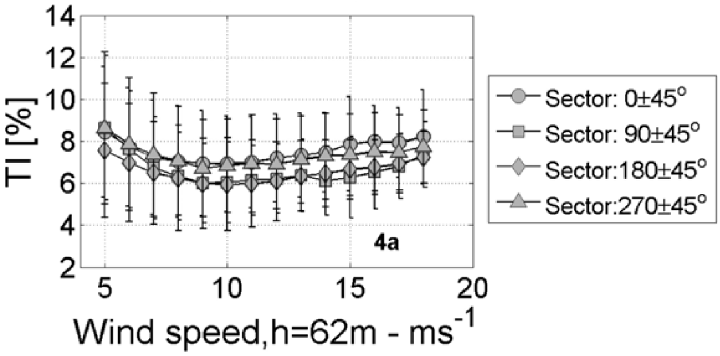

Figure 4.5: Turbulence intensity measurements at Horns Rev met mast 2. Measurement period: May 15, 1999 - May 14, 2002.[11].

Table 4.2: Frequency of occurrence per wind direction sector of the Lillgrund wind farm. Wind vane height: $z = 61\text{m}$; anemometer height: $z = 65\text{m}$. $A = 9.42\text{m/s}$, $k = 2.41$, $\overline{V}_{\infty,65} = 8.35\text{m/s}$, $\overline{WPD}_{65} = 594\text{W/m}^2$. Measurement period: *September 1, 2003 - February 28, 2006.*

| $\boldsymbol{\theta}_\infty[\pm\mathbf{15}°]$ | **Freq**[%] | $\boldsymbol{\theta}_\infty[\pm\mathbf{15}°]$ | **Freq**[%] | $\boldsymbol{\theta}_\infty[\pm\mathbf{15}°]$ | **Freq**[%] | $\boldsymbol{\theta}_\infty[\pm\mathbf{15}°]$ | **Freq**[%] |
|---:|---:|---:|---:|---:|---:|---:|---:|
| 15 | 5.55 | 105 | 7.63 | 195 | 8.93 | 285 | 13.65 |
| 45 | 5.13 | 135 | 9.39 | 225 | 12.22 | 315 | 5.87 |
| 75 | 5.32 | 165 | 7.14 | 255 | 14.44 | 345 | 4.72 |

### 4.3.3. Lillgrund - Wind rose and turbulence rose

As stated in Section 4.3.1, the Weibull wind speed distribution of the Lillgrund wind farm is assumed to be independent of the wind direction. However, the probability of occurrence per wind direction sector is not uniformly distributed. The frequency of occurrence per wind direction sector and the uniform Weibull parameters are given in Table 4.2. The wind direction information is subtracted from [62].

The presented meteorological conditions are based on measurements taken in the period *September 1, 2003 - February 28, 2006*, by the met mast displayed in the right graph of Figure 4.1. The turbulence intensity is assumed to have a constant value of $TI_\infty = 5.6\%$ over all wind directions and winds speeds, similar to the simulations in [18].

## 4.4. Validation cases

The number of validation cases that can potentially be investigated depends on the availability and representation of measurement data in literature, because no raw power generation measurement data is provided. Measurement data is extracted from validation reports of other wind farm-wake models and other papers describing power generation data. The validation cases are based on the simulations and methods, discussed and described in [11, 18, 19, 64].

Two different wake analysis methods are distinguished from the above mentioned sources. Explanations and visualisations of both methods are given in the upcoming paragraphs. As the measurement data originates from different authors and measurement devices, it is not possible to investigate exactly similar validation cases in the Lillgrund wind farm as in the Horns Rev wind farm. A number of cases is defined comprising different turbulence intensities, wind turbine spacings, wind speed ranges and wind direction ranges.

**A-case** The first analysis method, from now on called the 'A-case', investigates the power-loss fraction along a row of multiple wind turbines. The power-loss fraction is averaged over a specified wind speed range and a wind direction sector of $-15° \leq \theta'_\infty \leq +15°$, with respect to the orientation of the row. The power-loss fractions are calculated with respect to the first wind turbine in the row.

**B-case** The other method, the 'B-Case', investigates the power-loss fraction of one single-wake wind turbine. The power-loss fraction of the wind turbine is calculated with respect to the power generation of a wind turbine facing undisturbed meteorological conditions. The power-loss fraction is averaged over a specific wind speed range and is calculated as function of the angle between the wind direction and the orientation of the wind turbine row; $\theta'_\infty$.

### 4.4.1. Horns Rev

Three A-cases are investigated for the Horns Rev wind farm, which are discussed in the subsequent paragraphs. Power generation measurements used for the A-cases are stored in a free-stream wind speed bin of $7.5 < V_\infty \leq 8.5\text{m/s}$. Due to the small wind speed bin, the only simulation wind speed in FarmFlow-fast is $V_\infty = 8\text{m/s}$.

Next to the three A-cases, one B-case is investigated which is discussed in the subsequent paragraph. Power generation measurements for the B-case are stored in a free-stream wind speed bin of $7 < V_{\infty,62} \leq 9\text{m/s}$. FarmFlow-fast simulations are performed for $V_{\infty,62} = 7.5\text{m/s}$ and $V_{\infty,62} = 8.5\text{m/s}$, to represent the concerned wind speed range. It is not possible to investigate other B-cases with the Horns Rev wind farm, because no more power generation measurement data is available in literature.

Free-stream wind conditions are specified at a height of $z = 62\mathrm{m}$ for the B-case. The specification height differs from the A-cases, in which the free-stream conditions are specified at hub height; $z_{\mathrm{hub}} = 70\mathrm{m}$. The specification height of the B-case is different from the A-cases, because a wider wind speed range is concerned. Simulating for more than one wind speed requires the application of the Weibull distribution, which is obtained from met-mast 2 at a height of $z = 62\mathrm{m}$.

The A-cases use wind speed measurements from free-stream wind turbine 7. Wind turbine 7 is the first wind turbine in the seventh horizontal row from above, in the Horns Rev layout plot at the left side of Figure 4.1. It is assumed that the turbulence intensity is independent of measurement height.

**Case A1** Case A1 of the Horns Rev validation cases involves the power-loss fraction distribution along the six highlighted wind turbine rows, displayed in the top left graph of Figure 4.6. The black dots represent the free-stream wind turbines and the cyan dots are the nine wind turbines along each row, operating in the wake of one or more other wind turbines. The black arrows indicate the mean wind direction of the wind direction sector, for each concerned row.

The average wind direction comes from the west; $\theta_\infty = 270°$. The complete $30°$ wind direction sector that is taken into account is $\theta_\infty = 270 \pm 15°$. The distance between the wind turbines is $\Delta s = 7.0D$ along the mean wind direction.

**Case A2** Case A2 involves the power-loss fraction distribution along the two highlighted wind turbine rows, displayed in the bottom left sub-figure of Figure 4.6. The complete wind direction sector that is taken into account is $\theta_\infty = 312 \pm 15°$. The wind turbine spacing is $\Delta s = 10.4D$ along the mean wind direction. In this case, the power-loss fractions of six wind turbines operating in the wake of one or more other wind turbines are investigated.

**Case A3** Case A3 involves the power-loss fraction distribution along the two highlighted wind turbine rows, displayed in the bottom right sub-figure of Figure 4.6. The complete wind direction sector that is taken into account is $\theta_\infty = 221 \pm 15°$. The wind turbine spacing is $\Delta s = 9.4D$ along the mean wind direction. In this case, the power-loss fractions of six wind turbines operating in the wake of one or more other wind turbines are investigated.

**Case B1** Case B1 involves the power-loss fraction of the single-wake wind turbine highlighted in cyan, in the top right sub-figure of Figure 4.6. The power-loss fraction is calculated with respect to the wind turbine printed in black, as function of the angle between the wind direction and the orientation of the wind turbine row; $\theta'_\infty$. The investigated wind direction range is $\theta_\infty = 270 \pm 20°$. The distance between the wind turbines is $\Delta s = 7.0D$ along the mean wind direction. As stated previously, in B-cases the power-loss fraction of only one wind turbine operating in the wake of one other wind turbine is investigated.

### 4.4.2. Lillgrund

One A-case and two B-cases are investigated for the Lillgrund wind farm, which are discussed in the subsequent paragraphs. Power generation measurements used for the Lillgrund validation cases are stored in a free-stream wind speed bin of $4 < V_\infty \leq 10\mathrm{m/s}$. The wind speeds $V_\infty = [4.5, 5.5, 6.5, 7.5, 8.5, 9.5]\mathrm{m/s}$ are simulated to represent the concerned wind speed range. All free-stream conditions are specified at hub height; $z_{\mathrm{hub}} = 65\mathrm{m}$.

**Case A1** Case A1 of the Lillgrund simulations involves the power-loss fraction distribution along the highlighted wind turbine row, shown in the top left graph of Figure 4.7. The investigated wind direction sector comes from the south-west; $\theta_\infty = 222 \pm 15°$. The distance between the wind turbines is $\Delta s = 4.3D$ along the mean wind direction. The power-loss fractions of seven wind turbines operating in the wake of one or more other wind turbines are investigated in this case.

**Case B1** Case B1 involves the power-loss fraction of the single-wake wind turbine highlighted in cyan, in the top right sub-figure of Figure 4.7. The power-loss fraction is calculated with respect to the wind turbine printed in black, as function of the angle between the wind direction and the orientation of the

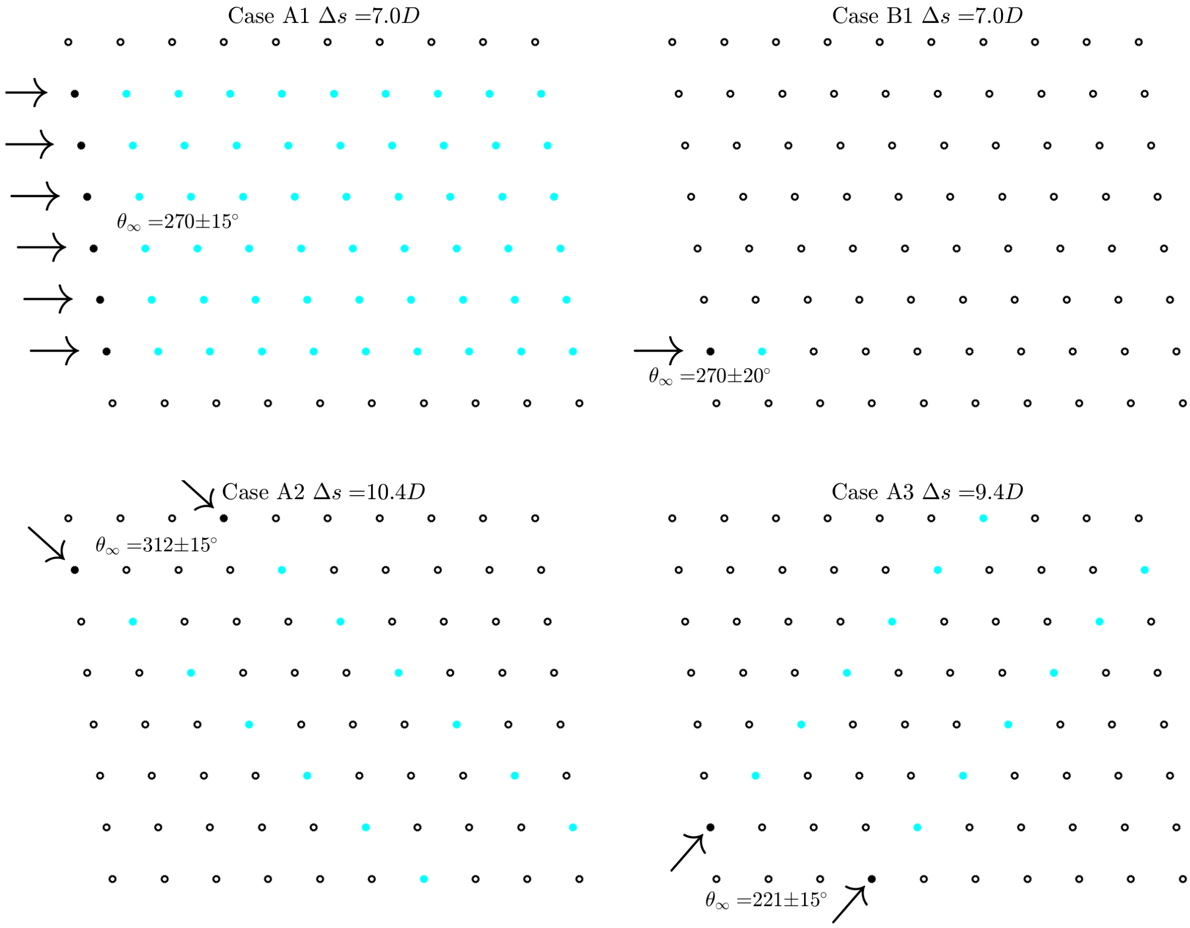

Figure 4.6: Wind direction sectors and investigated wind turbines of the Horns Rev validation cases. Top left: Case A1, top right: Case B1, bottom left: Case A2, bottom right: Case A3.

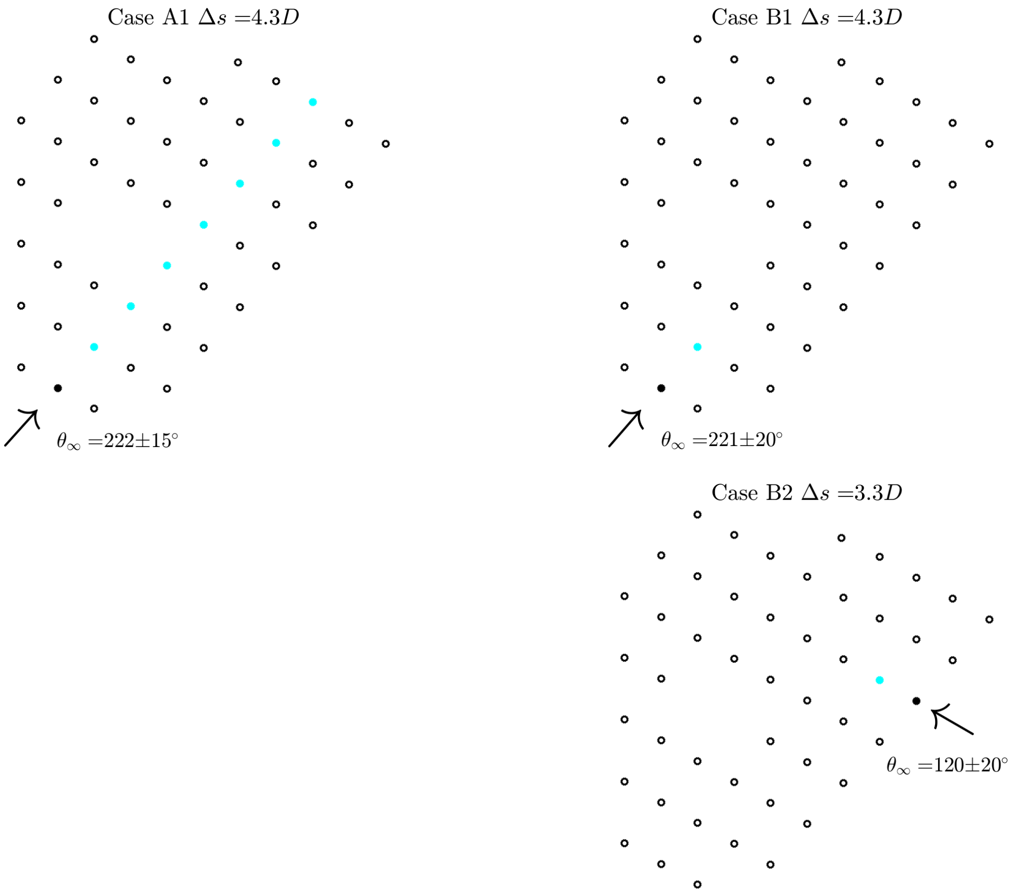

Figure 4.7: Wind direction sectors and investigated wind turbines of the Lillgrund validation cases. Top left: Case A1, top right: Case B1, bottom right: Case B2.

wind turbine row; $\theta'_\infty$. The investigated wind direction range is $\theta_\infty = 222 \pm 20°$. The distance between the two wind turbines is $\Delta s = 4.3D$ along the mean wind direction.

**Case B2** Case B2 involves the power-loss fraction of the single-wake wind turbine highlighted in cyan, in the bottom right graph of Figure 4.7. The power-loss fraction is calculated with respect to the wind turbine printed in black, as function of the angle between the wind direction and the orientation of the wind turbine row; $\theta'_\infty$. The investigated wind direction range is $\theta_\infty = 120 \pm 20°$. The wind turbine spacing is $\Delta s = 3.3D$ along the mean wind direction, which is the closest spacing of all validation cases.

## 4.5. Post-processing of simulations

In validation studies it is important that proper comparisons are made between simulation results and measurement data. Simulations can only be properly compared with measurement data if both data sources are averaged over corresponding wind direction sectors, wind speed ranges and other atmospheric conditions.

Measurement data is stored in wind speed and direction bins, while simulation data is usually generated as discrete points at regular sample intervals. The size of measurement data bins depends on the amount of available measurement data and the precision of the measurement devices. Measurement data bins of rarely occurring atmospheric conditions tend to be larger than bins of ordinary atmospheric conditions[11].

Differences between FarmFlow-fast simulation data and the power generation measurement data of the current validation study are found in the way the power generation data is established. Next

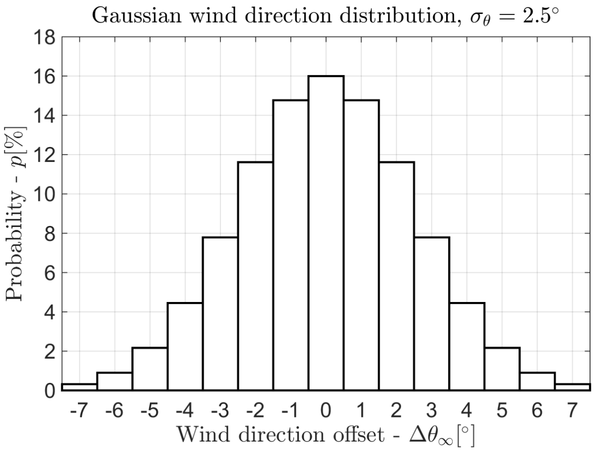

Figure 4.8: Gaussian wind direction distribution with a standard deviation of $\sigma_\theta = 2.5°$.

to the above mentioned difference in bin size/sampling interval, FarmFlow-fast does not take wind direction uncertainty into account. Wind direction uncertainty originates from yaw misalignment of the free-stream wind turbine, spatial variability of the wind direction inside a wind farm and variability of the wind direction within the averaging period[65].

Wind direction uncertainty becomes explicitly important if small wind direction sectors are concerned [65] or when the influence of the wind direction on the power-loss fraction is investigated, as done in the B-cases of the validation study. Post-processing of simulation results is required to account for wind direction uncertainty and to average simulation data over similar wind direction sectors and wind speed ranges as the measurement data.

### 4.5.1. Wind direction uncertainty

Wind direction uncertainty is accounted for by replacing simulation results with a weighted average over several simulations, covering a span of wind directions. The weights are based on a normal distribution that approximates the wind direction uncertainty.

The normal distribution used for the validation cases is shown in Figure 4.8. The distribution has a wind direction standard deviation of $\sigma_\theta = 2.5°$, which is lower than typical offshore conditions[65, 66]. The lower standard deviation is chosen in consultation with the developer of FarmFlow-fast, by assuming that some directionality is already taken into account by the empirical tuning of the near wake model.

The weighted average is calculated from simulation results within three standard deviations from the concerned wind direction, $-3\sigma_\theta \leq \Delta\theta_\infty \leq 3\sigma_\theta$, to ensure a cumulative probability of 99.7%. The weighted average power generation is calculated as function of free-stream wind speed and direction, $P_{\mathrm{WA}}(V_\infty, \theta_\infty)$, by Equation (4.1). In this equation, $P_{\mathrm{sim}}$ is the power generation value obtained by FarmFlow-fast simulations and $\Delta\theta_\infty$ is the discrete direction offset, from the wind direction that is post-processed.

$$P_{\mathrm{WA}}(V_\infty, \theta_\infty) = \frac{\sum\limits_{\Delta\theta_\infty=-7}^{7} P_{\mathrm{sim}}(V_\infty, \theta_\infty + \Delta\theta_\infty)\, e^{\frac{-\Delta\theta_\infty^2}{2\sigma_\theta^2}}}{\sum\limits_{\Delta\theta_\infty=-7}^{7} e^{\frac{-\Delta\theta_\infty^2}{2\sigma_\theta^2}}} \tag{4.1}$$

### 4.5.2. Bin sizing

The difference between the sampling intervals of FarmFlow-fast simulations and bin sizes of the measurement data should be compensated for. This is done by multiplying simulation results per sampling point with the associated probability of occurrence[3]. The probability of occurrence is determined by the Weibull wind speed distribution of the concerned wind direction sector.

---

[3] This is done after the wind direction-uncertainty compensation has been applied to the power generation simulation data.

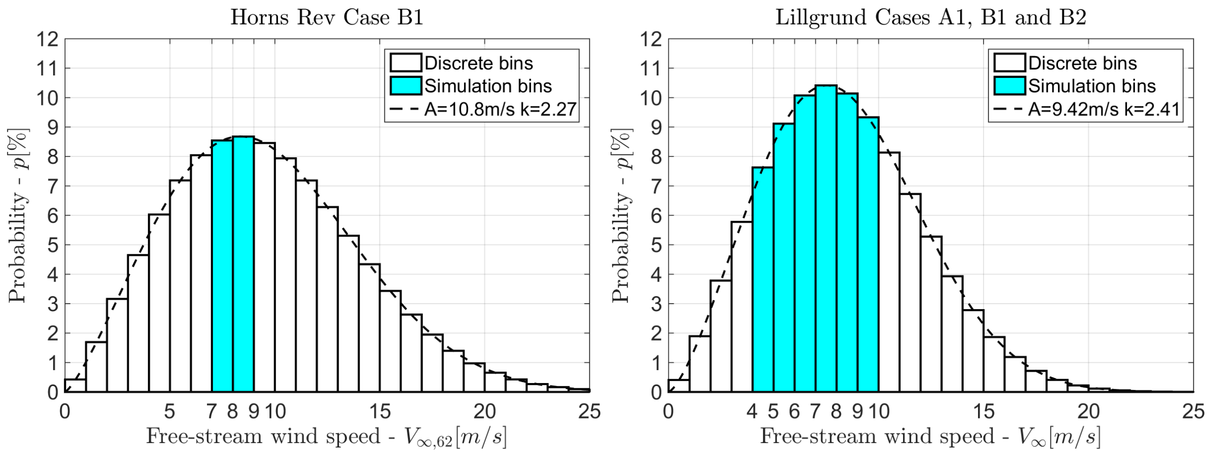

Figure 4.9: Weibull factors used to post-process the power generation simulation data samples. Left: Horns Rev Case B1, right: Lillgrund cases.

If a range of wind speeds is concerned, as in the Lillgrund validation cases and Case B1 of Horns Rev, simulations are performed at wind speed sample intervals of $|\Delta V_\infty| = 1\mathrm{m}/s$. The weighted average power generation over the wind speed range specified by the measurement data is calculated by multiplying the weighted average power generation values, per wind speed sample, with its normalized probability of occurrence. The wind speed samples used for the simulations and their probability of occurrence are displayed in Figure 4.9[4]

**Horns Rev** For Case B1 of the Horns Rev validation cases, the average power generation in the $7 < V_{\infty,62} \leq 9\mathrm{m}/s$ range is concerned. To calculate the average power generation in this wind speed range, Equation (4.2) is applied to the simulation data.

$$\overline{P}\left(7 < V_{\infty,62} \leq 9, \theta_\infty\right) = \frac{\sum\limits_{V_{\infty,62}=7.5}^{8.5} \overline{P}_{\mathrm{WA}}\left(V_{\infty,62}, \theta_\infty\right)\left(\frac{V_{\infty,62}}{A}\right)^{k-1} e^{-\left(\frac{V_{\infty,62}}{A}\right)^k}}{\sum\limits_{V_{\infty,62}=7.5}^{8.5}\left(\frac{V_{\infty,62}}{A}\right)^{k-1} e^{-\left(\frac{V_{\infty,62}}{A}\right)^k}} \tag{4.2}$$

The power generation measurement data of the Horns Rev wind turbines is extracted from [11]. The measurements cover the period *January 1, 2005 - December 31, 2007*, which corresponds to the measurement period of met-mast 2 in the WAsP database. The measurement data is stored in wind direction bins of $|\Delta\theta_\infty| = 5°$[11].

Simulations of the Horns Rev cases are performed at wind direction steps of $|\Delta\theta_\infty| = 1°$. Since simulation data is gathered at smaller wind direction intervals than the measurement data, Equation (4.3) is used to post-process the simulation data[5]. In this equation, $\overline{P}_{5°}$ is the average power generation of a $|\Delta\theta_\infty| = 5°$ wind direction sector.

$$\overline{P}_{5°}\left(7 < V_{\infty,62} \leq 9, \theta_\infty\right) = \sum_{\Delta\theta_\infty=-2}^{2} \frac{\overline{P}\left(V_{\infty,62}, \theta_\infty + \Delta\theta_\infty\right)}{5} \tag{4.3}$$

**Lillgrund** For the Lillgrund validation cases, the average power generation in the $4 < V_\infty \leq 10\mathrm{m}/s$ range is concerned. To calculate the average power generation in this wind speed range, Equation (4.4) is applied to the simulation data.

---

[4] The Weibull distribution for Case B1 of Horns Rev is generated from the $A$ and $k$ parameters for $\theta_\infty = 270 \pm 15°$, in Table 4.1.

[5] This equation smooths the power-loss fraction curve, as function of the wind direction.

$$\overline{P}\left(4 < V_\infty \leq 10, \theta_\infty\right) = \frac{\sum\limits_{V_\infty=4.5}^{9.5} P\left(V_\infty, \theta_\infty\right)\left(\frac{V_\infty}{A}\right)^{k-1} e^{-\left(\frac{V_\infty}{A}\right)^k}}{\sum\limits_{V_\infty=4.5}^{9.5} \left(\frac{V_\infty}{A}\right)^{k-1} e^{-\left(\frac{V_\infty}{A}\right)^k}} \tag{4.4}$$

The power generation measurement data of the wind turbines is extracted from [18] and [64]. The measurements cover the period *December 21, 2007 - February 19, 2009*, which corresponds to the measurement period of the met-mast. The measurement data is stored in wind direction bins of $|\Delta\theta_\infty| = 3°$[18].

Simulations of the Lillgrund cases are also performed with a wind direction step of $|\Delta\theta_\infty| = 1°$. Since the measurement data of Lillgrund is stored in bins of $|\Delta\theta_\infty| = 3°$, Equation (4.5) is used to post-process the simulation data[5]. In this equation, $\overline{P}_{3°}$ is the average power generation of a $|\Delta\theta_\infty| = 3°$ wind direction sector.

$$\overline{P}_{3°}\left(4 < V_\infty \leq 10, \theta_\infty\right) = \sum_{\Delta\theta_\infty=-1}^{1} \frac{\overline{P}\left(V_\infty, \theta_\infty + \Delta\theta_\infty\right)}{3} \tag{4.5}$$

### 4.5.3. Calculation of the power-loss fraction

Once the power generation simulation data is post-processed, simulations can be compared with measurement data. This is done is by comparing the calculated power-loss fractions of the wind turbines highlighted in Figures 4.6 and 4.7 with each other. As stated in Section 2.2, the power-loss fraction is defined as the fractional power generation loss of a wind turbine operating in a wake, with respect to a wind turbine exposed to undisturbed meteorological conditions[11, 19].

The mathematical expression of the power-loss fraction is given by Equation (4.6). In this equation, $P_{\text{free}}[\text{kW}]$ is the power generation of the free-stream wind turbine, to which the power generation of the 'wake' wind turbines are compared. $P_{\text{wake}}[\text{kW}]$ is the power generation of the wind turbine(s), operating in the wake of the free-stream wind turbine. The power-loss fraction can be calculated for single wind speed/direction combinations, but in the validation cases the averaged power-loss fraction over a range of wind speeds and directions is concerned.

$$\xi_{\text{P}} = 1 - \frac{P_{\text{wake}}}{P_{\text{free}}} \tag{4.6}$$

**A-cases** For the A-cases, the average power-loss fraction over a wind direction sector of 30 degrees, $-15 \leq \theta'_\infty \leq 15°$, is calculated from the simulation data by Equation (4.7). The values for $P_{\text{wake}}$ and $P_{\text{free}}$ in this equation are taken from Equations (4.3) and (4.5), for respectively the Horns Rev and the Lillgrund wind farm. $\overline{\theta}_\infty$ is the average wind direction of the investigated wind direction sector, which is aligned with the wind turbine row. The free-stream wind turbine and wake wind turbines are indicated per validation case in Figure 4.6 and Figure 4.7.

$$\overline{\xi}_{\text{P}}\left(-15 \leq \theta'_\infty \leq 15°\right) = 1 - \sum_{\theta'_\infty=-15}^{15} \frac{P_{\text{wake}}\left(\overline{\theta}_\infty + \theta'_\infty\right)}{P_{\text{free}}\left(\overline{\theta}_\infty + \theta'_\infty\right)} \tag{4.7}$$

If multiple rows with similar wind turbine spacing are taken into account like in Case A1, A2 and A3 of Horns Rev, the power-loss fractions of wind turbines at the same position are averaged.

**B-cases** For the B-cases, the power-loss fraction is calculated as function of the wind direction, in the $-20 \leq \theta'_\infty \leq 20°$ domain. This is done by Equation (4.8). The values for $P_{\text{wake}}$ and $P_{\text{free}}$ in this equation are also taken from Equations (4.3) and (4.5). The calculations are performed in steps of $|\Delta\theta_\infty| = 1°$, after application of the post-processing equations.

$$\xi_{\text{P}}\left(\theta'_\infty\right) = 1 - \frac{P_{\text{wake}}\left(\overline{\theta}_\infty + \theta'_\infty\right)}{P_{\text{free}}\left(\overline{\theta}_\infty + \theta'_\infty\right)} \tag{4.8}$$

Table 4.3: Simulation overview of the FarmFlow-fast validation; $z$[m] represents the specification height of the input conditions.

| **Wind Farm** | **Case** | **Sector** | $\mathbf{z}$[m] | $\mathbf{V}_{\infty,\mathbf{z}}$[m/s] | $\boldsymbol{\theta}_{\infty,\mathbf{z}}$[°] | $\mathbf{TI}_{\infty,\mathbf{z}}$[%] |
|---|---|---|---|---|---|---|
| Horns Rev | A1 | $270 \pm 15°$ | 70 | 8 | $246 : 294$ | 7.0 |
| Horns Rev | A2 | $312 \pm 15°$ | 70 | 8 | $288 : 336$ | 7.0 |
| Horns Rev | A3 | $221 \pm 15°$ | 70 | 8 | $197 : 245$ | 7.0 |
| Horns Rev | B1 | $270 \pm 20°$ | 62 | 7.5; 8.5 | $241 : 299$ | 7.0 |
| Lillgrund | A1 | $222 \pm 15°$ | 65 | 4.5; 5.5; 6.5; 7.5; 8.5; 9.5 | $199 : 245$ | 5.6 |
| Lillgrund | B1 | $222 \pm 20°$ | 65 | 4.5; 5.5; 6.5; 7.5; 8.5; 9.5 | $194 : 250$ | 5.6 |
| Lillgrund | B2 | $120 \pm 20°$ | 65 | 4.5; 5.5; 6.5; 7.5; 8.5; 9.5 | $92 : 148$ | 5.6 |

Table 4.4: Properties of the computer system, on which all simulations are performed.

| **Component** | **Value** |
|---|---|
| Processor | Intel(R) Core(TM) i7-2670QM CPU @ 2.20 GHz |
| Installed memory (RAM) | 8.00 GB |
| System type | 64-bit operating System |

For plotting of the B-cases, the power-loss fraction data points are fitted with the expression shown in Equation (4.9). This expression is based on the method used in [11]. The variables $c_0$, $c_1$, $c_2$, $c_3$ and $c_4$ are determined by fitting the expression to the measurement data points or simulation data points. The curve fitting yields a continuous power-loss fraction distribution, as function of wind direction offset. The continuous distribution can be used to quantify the wake expansion and maximum power-loss fraction.

$$f_\xi\left(\theta'_\infty\right) = c_0 + \left(c_1 + c_2\theta'_\infty + c_3\theta'^2_\infty\right) e^{-c_4\theta'^2_\infty} \tag{4.9}$$

## 4.6. Simulation overview

Table 4.3 provides a complete overview of simulations that are performed for the validation study, along with the FarmFlow-fast inputs. Wind conditions are specified at hub height for all cases except for Case B1 of Horns Rev, in which the height of the met mast, $z = 62\mathrm{m}$, is used. For Case B1 of Horns Rev, the wind speed at hub height is automatically calculated by the ABL model of FarmFlow-fast.

The wind direction range used for the simulations is larger than the actual concerned wind direction sector. This is done to guarantee that all wind directions within the sector are adequately post-processed by the wind direction uncertainty and bin size correction equations. The wider simulation range is required, because the post-processing equations use power generation simulation data from wind directions outside the investigated wind direction sector. All simulations are performed on a laptop with the system specifications displayed in Table 4.4.

## 4.7. Results of the validation cases

This section presents the results of the validation cases. It starts with the Horns Rev cases in Section 4.7.1. Hereafter, Section 4.7.2 presents the results of the Lillgrund cases. Finally, Section 4.7.3 gives the main conclusions drawn from comparing FarmFlow-fast simulations with FarmFlow simulations and measurement data.

### 4.7.1. Horns Rev

**Case A1** The results of Case A1 of the Horns Rev validation cases are displayed at the top left of Figure 4.10. Table A.1 in Appendix A provides a numerical presentation of the results, together with the numerical data of the other A-cases. By analysing the simulation results, it can be concluded that the shape of the power-loss fraction build-up along the rows is similar for FarmFlow-fast and the original FarmFlow version. The power-loss fraction build-up is also roughly in line with the measurement data[6].

---

[6] The measured data is obtained from [11].

The measurement data shows that the power-loss fraction at the second wind turbine is $\overline{\xi}_{\mathrm{P}_{2,\mathrm{M}}} = 20.4\%$, which monotonically increases up to $\overline{\xi}_{\mathrm{P}_{10,\mathrm{M}}} = 41.0\%$ at the tenth wind turbine along the rows. From the FarmFlow-fast simulation data, a power-loss fraction of $\overline{\xi}_{\mathrm{P}_{2,\mathrm{S}}} = 19.1\%$ is calculated at the second wind turbine and $\overline{\xi}_{\mathrm{P}_{10,\mathrm{S}}} = 38.5\%$ at the tenth wind turbine. The FarmFlow-fast simulation data shows a minimum power-loss fraction of $\overline{\xi}_{\mathrm{P}_{3,\mathrm{S}}} = 18.6\%$ at the third wind turbine.

For most wind turbines the power-loss fraction is underestimated, while for wind turbines 6 and 7 an overestimation is observed. The maximum absolute difference in power-loss fraction between the FarmFlow-fast simulations and the measurements is $|\Delta\overline{\xi}_{\mathrm{P}_{\mathrm{SM,max}}}| = 2.6 \cdot 10^{-2}$, at wind turbine 4.

The calculated power-loss fractions from the FarmFlow-fast simulations are lower than the original FarmFlow simulations. The maximum absolute difference in power-loss fraction between the two software versions is $|\Delta\overline{\xi}_{\mathrm{P}_{\mathrm{FN,max}}}| = 8.6 \cdot 10^{-3}$, at wind turbine 10. The simulation results of the original FarmFlow version are closer to the measurements for most wind turbines, while for wind turbines 6 and 7 the results of the FarmFlow-fast simulations are closer.

**Case A2** The results of Case A2 are displayed at the bottom left of Figure 4.10. The shape of the power-loss fraction build-up shows again similar behaviour for both software versions and the measurement data. The offset between the FarmFlow-fast simulations and the measurements[6] is however larger than in Case A1. The software versions seem to be equally close to each other as in Case A1.

The measurement data shows that the power-loss fraction at the second wind turbine is $\overline{\xi}_{\mathrm{P}_{2,\mathrm{M}}} = 12.6\%$. The initial power-loss fraction is lower than for Case A1, which is in line with the phenomenon that wake effects reduce with increasing wind turbine spacing. The power-loss fraction increases monotonically up to $\overline{\xi}_{\mathrm{P}_{7,\mathrm{M}}} = 36.1\%$ at the seventh wind turbine. The final power-loss fraction is slightly higher than at the seventh wind turbine in Case A1. The higher power-loss fraction could be caused by the increasing number of interacting wakes, due to the closer wind turbine spacing perpendicular to the wind direction.

From the FarmFlow-fast simulation data, a power-loss fraction of $\overline{\xi}_{\mathrm{P}_{2,\mathrm{S}}} = 14.9\%$ is calculated at the second wind turbine, which monotonically increases up to $\overline{\xi}_{\mathrm{P}_{7,\mathrm{S}}} = 39.0\%$ at the seventh wind turbine. The power-loss fraction is overestimated for all wind turbines. The maximum absolute difference in power-loss fraction between the FarmFlow-fast simulations and the measurements is $|\Delta\overline{\xi}_{\mathrm{P}_{\mathrm{SM,max}}}| = 3.6 \cdot 10^{-2}$, at wind turbine 5.

The calculated power-loss fractions from the FarmFlow-fast simulations are lower than the original FarmFlow simulations. The maximum absolute difference in power-loss fraction between the two software versions is $|\Delta\overline{\xi}_{\mathrm{P}_{\mathrm{FN,max}}}| = 9.9 \cdot 10^{-3}$, at wind turbine 3. The simulation results of FarmFlow-fast are closer to the measurements than the original FarmFlow simulations, for all wind turbines.

**Case A3** The results of Case A3 are displayed at the bottom right of Figure 4.10. The power-loss fraction build-up shows a close relation between both software versions and the measurement data. The offset between the FarmFlow-fast simulations and the measurements[6] is in the same order as in Case A1. The differences between both software versions are larger than in Case A1 and A2.

The measurement data shows that the power-loss fraction at the second wind turbine is $\overline{\xi}_{\mathrm{P}_{2,\mathrm{M}}} = 16.8\%$. The initial power-loss faction lies in between Case A1 and A2, corresponding to the intermediate wind turbine spacing. The power-loss fraction increases monotonically up to $\overline{\xi}_{\mathrm{P}_{7,\mathrm{M}}} = 40.0\%$ at the seventh wind turbine. The final power-loss fraction is higher than at the seventh wind turbine in Cases A1 and A2. The higher power-loss fraction could be caused by the combination of the wind turbine spacing along the wind direction and perpendicular to the wind direction.

From the FarmFlow-fast simulation data, a power-loss fraction of $\overline{\xi}_{\mathrm{P}_{2,\mathrm{S}}} = 14.7\%$ is calculated at the second wind turbine, which monotonically increases up to $\overline{\xi}_{\mathrm{P}_{7,\mathrm{S}}} = 38.6\%$ at the seventh wind turbine. The power-loss fraction is underestimated for all wind turbines. The power-loss fraction build-up calculated from the FarmFlow-fast simulations is even lower than the simulations in Case A2, which might have been caused by underestimation of the wake expansion. The maximum absolute difference in power-loss fraction between the FarmFlow-fast simulations and the measurements is $|\Delta\bar{\xi}_{\mathrm{P}_{\mathrm{SM,max}}}| = 2.1 \cdot 10^{-2}$, at wind turbine 2.

The calculated power-loss fractions from the FarmFlow-fast simulations are higher than the original FarmFlow simulations. The maximum absolute difference in power-loss fraction between the two software versions is $|\Delta\bar{\xi}_{\mathrm{P}_{\mathrm{FN,max}}}| = 1.6 \cdot 10^{-2}$, at wind turbine 4. The simulation results of FarmFlow-fast are closer to the measurements than the original FarmFlow simulations, for all wind turbines.

**Case B1** The results of Case B1 are displayed at the top right of Figure 4.10. The graph shows the measurement and simulation data points and the numerically fitted curves by Equation (4.9). Table A.2 in Appendix A provides a numerical presentation of the results, together with the numerical data of the other B-cases. By analysing the simulation results, it can be concluded that the shape of the power-loss fraction curve as function of the wind direction, is similar for FarmFlow-fast and the original FarmFlow version. The power-loss fraction curve is also roughly in line with the measurements[6].

The measurement data shows that the maximum power-loss fraction at the second wind turbine is $\xi_{\mathrm{P}_{2,\mathrm{M,max}}} = 41.2\%$, when the wind direction is aligned with the orientation of the wind turbine row. The peak power-loss fraction is about two times as high as the average power-loss fraction over the $-15^\circ \leq \theta'_\infty \leq +15^\circ$ range at the second wind turbine in Case A1. The power-loss fraction gradually reduces towards lower values, at larger wind direction offsets. From the FarmFlow-fast simulation data, a maximum power-loss fraction of $\xi_{\mathrm{P}_{2,\mathrm{S,max}}} = 42.0\%$ is calculated at the second wind turbine. The power-loss fraction gradually reduces with increasing wind direction offset, until small power-increase fractions are calculated.

The power-loss fraction is overestimated in the $-7^\circ \leq \theta'_\infty \leq +7^\circ$ range, while it is underestimated for larger incidence angles between the wind direction and the wind turbine row orientation. The maximum absolute difference in power-loss fraction between the FarmFlow-fast curve fit and the measurement data curve fit is $|\Delta\xi_{\mathrm{P}_{\mathrm{SM,max}}}| = 3.7 \cdot 10^{-2}$, which occurs at a wind direction offset of $\theta'_\infty = +20^\circ$.

The most remarkable difference between the FarmFlow-fast results and the measurement data is the negative power-loss fraction observed at wind direction offsets $\theta'_\infty < -15^\circ$ and $\theta'_\infty > +15^\circ$. The power-increase fraction is caused by an increasing wind speed, just outside the edges of wind turbine wakes. This effect is not shown by the measurement data. As no clear evidence is observed for underestimation of wake expansion, the offset in power-loss fraction is most likely caused by improperly accounting for wind direction uncertainty.

The calculated power-loss fractions from the FarmFlow-fast simulations are lower than the original FarmFlow simulations in the $-4^\circ \leq \theta'_\infty \leq +5^\circ$ range and higher for incidence angles outside this range. The maximum absolute difference in power-loss fraction between the two software versions is $|\Delta\xi_{\mathrm{P}_{\mathrm{FN,max}}}| = 8.6 \cdot 10^{-3}$, which occurs at $\theta'_\infty = -10^\circ$. The simulation results of the original FarmFlow version are closer to the measurements for most wind directions, although the differences between the results of both software versions are negligible.

The FarmFlow-fast simulations of Horns Rev took on average 54 seconds per wind speed/direction combination, while it took 17 minutes in the original FarmFlow version. This means that a complete assessment for every integer wind speed between cut-in and cut-out wind speed $V_\infty = (4:25)\,\mathrm{m/s}$ and 72 wind direction sectors of $|\Delta\theta_\infty| = 5^\circ$, would take $\sim 24\mathrm{hrs}$ with FarmFlow-fast and $\sim 450\mathrm{hrs}$ with the original version.

### 4.7.2. Lillgrund

**Case A1** The results of Case A1 of the Lillgrund validation cases are displayed at the top left of Figure 4.11. By analysing the simulation results, it can be concluded that also for this case the shape of the power-loss fraction build-up along the rows is similar for FarmFlow-fast and the original FarmFlow version. The power-loss fraction build-up is again roughly in line with the measurement data[7].

The measurement data shows that the power-loss fraction at the second wind turbine is $\bar{\xi}_{\mathrm{P}_{2,\mathrm{M}}} = 36.4\%$, which increases monotonically up to $\bar{\xi}_{\mathrm{P}_{8,\mathrm{M}}} = 65.8\%$ at the eighth wind turbine. The power-loss fraction curve is higher than the curves of the Horns Rev cases.

---

[7] The measured data is obtained from [18].

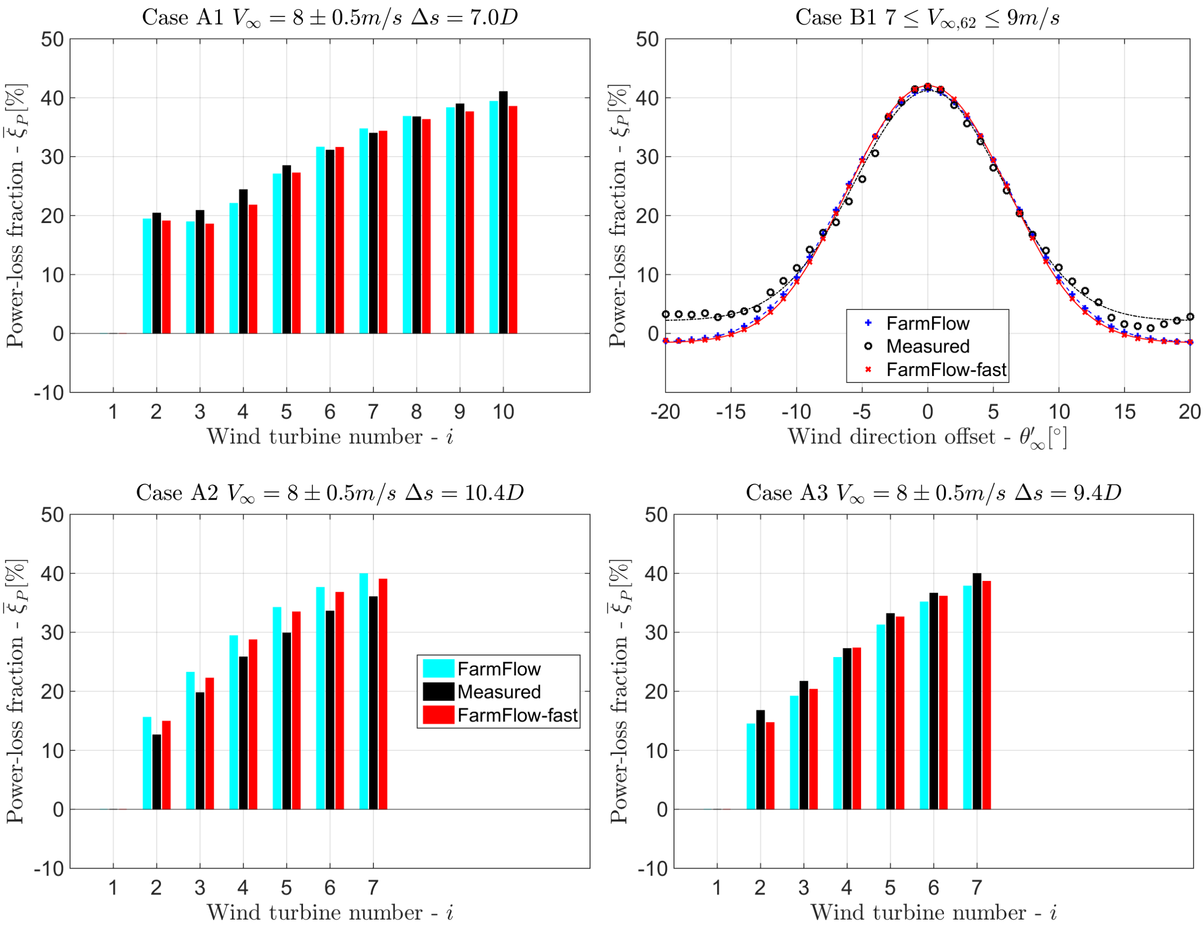

Figure 4.10: Horns Rev validation results. All validation cases use a moving window of $|\Delta\theta_\infty| = 5°$. Top left: Case A1, top right: Case B1, bottom left: Case A2, bottom right: Case A3.

The higher power-loss fractions are caused by multiple reasons. First of all, the wind turbine spacing is closer; both along the wind direction and perpendicular to the wind direction. Secondly, the ambient turbulence intensity is lower. Thirdly, the thrust coefficient of the Siemens SWT-2.3-93 wind turbines is higher than the Vestas V80 in the concerned wind speed range. Finally, the wind speed range includes wind speeds that are close to cut-in wind speed, for which the wind turbines in the wake experience a power-loss fraction of $\overline{\xi}_{\mathrm{P}_{2:8}}\,(V_\infty \approx V_{\mathrm{in}}) = 100\%$.

From the FarmFlow-fast simulation data, a power-loss fraction of $\overline{\xi}_{\mathrm{P}_{2,\mathrm{S}}} = 41.4\%$ is calculated at the second wind turbine and $\overline{\xi}_{\mathrm{P}_{8,\mathrm{S}}} = 65.1\%$ at the eighth wind turbine. The FarmFlow-fast simulation data shows a minimum power-loss fraction of $\overline{\xi}_{\mathrm{P}_{3,\mathrm{S}}} = 38.1\%$ at the third wind turbine. The power-loss fraction is overestimated for the second wind turbine, but the simulations underestimate the power-loss fractions of the wind turbines further downstream. The maximum absolute difference in power-loss fraction between the FarmFlow-fast simulations and the measurements is $|\Delta\overline{\xi}_{\mathrm{P}_{\mathrm{SM,max}}}| = 5.0 \cdot 10^{-2}$, at wind turbine 2.

The calculated power-loss fractions from the FarmFlow-fast simulations are lower than the original FarmFlow simulations. The maximum absolute difference in power-loss fraction between the two software versions is $|\Delta\overline{\xi}_{\mathrm{P}_{\mathrm{FN,max}}}| = 2.6 \cdot 10^{-2}$, at wind turbine 5. The simulation results of the original FarmFlow version are closer to the measurements for wind turbines 3 to 7, while for wind turbines 2 and 8 the results of the FarmFlow-fast simulations are closer.

**Case B1** The results of Case B1 are displayed at the top right of Figure 4.11. By analysing the simulation results, it can also for this case be concluded that the shape of the power-loss fraction curve as function of the wind direction, is similar for FarmFlow-fast and the original FarmFlow version. The power-loss fraction curve is also roughly in line with the measurements[8].

The measurement data shows that the maximum power-loss fraction at the second wind turbine is $\xi_{\mathrm{P_{2,M,max}}} = 70.6\%$. The peak power-loss fraction is about two times as high as the average power-loss fraction over the $-15^\circ \leq \theta'_\infty \leq +15^\circ$ range at the second wind turbine in Case A1, corresponding to the observations of Case A1 and B1 of Horns Rev. The power-loss fraction gradually reduces towards lower values, at larger wind direction offsets. From the FarmFlow-fast simulation data, a maximum power-loss fraction of $\xi_{\mathrm{P_{2,S,max}}} = 71.8\%$ is calculated at the second wind turbine. The power-loss fraction gradually reduces with increasing wind direction offset, until small power-increase fractions are calculated.

The power-loss fraction is overestimated in the $-15^\circ \leq \theta'_\infty \leq +15^\circ$ range, while it is underestimated for larger incidence angles. The maximum absolute difference in power-loss fraction between the FarmFlow-fast curve fit and the measurement data curve fit is $|\Delta\xi_{\mathrm{P_{SM,max}}}| = 6.3 \cdot 10^{-2}$, which is larger than the maximum absolute error in Horns Rev Case B1. The maximum difference occurs at a wind direction offset of $\theta'_\infty = -9^\circ$.

Negative power-loss fractions are also observed in the simulation data of this case, for wind direction offsets $\theta'_\infty < -18^\circ$ and $\theta'_\infty > +18^\circ$. The larger wind direction offset than in Horns Rev Case B1 is a consequence of the closer wind turbine spacing. A closer wind turbine spacing causes the second wind turbine to be in the wake of the first wind turbine for wider wind direction ranges than would be the case with a larger wind turbine spacing.

The calculated power-loss fractions from the FarmFlow-fast simulations are lower than the original FarmFlow simulations in the $-17^\circ \leq \theta'_\infty \leq +17^\circ$ range and higher for larger incidence angles. The maximum absolute difference in power-loss fraction between the two software versions is $|\Delta\xi_{\mathrm{P_{FN,max}}}| = 3.2 \cdot 10^{-2}$, which occurs at $\theta'_\infty = +9^\circ$. The simulation results of FarmFlow-fast are closer to the measurements for most wind directions.

**Case B2** The results of Case B2 are displayed at the bottom right of Figure 4.11. The power-loss fraction curve shows again a close relation between both software versions and the measurement data[8]. The power-loss fractions calculated in this case are the highest of all validation cases.

The measurement data shows that the maximum power-loss fraction at the second wind turbine is $\xi_{\mathrm{P_{2,M,max}}} = 81.6\%$. The power-loss fraction gradually reduces towards lower values, at larger wind direction offsets. From the FarmFlow-fast simulation data, a maximum power-loss fraction of $\xi_{\mathrm{P_{2,S,max}}} = 77.5\%$ is calculated at the second wind turbine. The power-loss fraction gradually reduces towards lower values, with increasing wind direction offset.

The power-loss fraction is underestimated in the $-8^\circ \leq \theta'_\infty \leq +10^\circ$ range and for angles $\theta'_\infty \leq -19^\circ$ and $\theta'_\infty \geq +19^\circ$, while it is overestimated in the intermediate ranges. The maximum absolute difference in power-loss fraction between the FarmFlow-fast curve fit and the measurement data curve fit is $|\Delta\xi_{\mathrm{P_{SM,max}}}| = 5.9 \cdot 10^{-2}$, which occurs at a wind direction offset of $\theta'_\infty = +5^\circ$. Negative power-loss fractions are not observed in the simulation data of this case, which is a consequence of the even closer wind turbine spacing than in Case B1.

The calculated power-loss fractions from the FarmFlow-fast simulations are lower than the original FarmFlow simulations in the $-9^\circ \leq \theta'_\infty \leq +9^\circ$ range and higher for larger incidence angles. The maximum absolute difference in power-loss fraction between the two software versions is $|\Delta\xi_{\mathrm{P_{FN,max}}}| = 6.6 \cdot 10^{-3}$, which occurs at $\theta'_\infty = +16^\circ$. The simulation results of the original FarmFlow version are closer to the measurements for most wind directions, although the differences between the results of both software versions are negligible.

The FarmFlow-fast simulations of Lillgrund took on average 60 seconds per wind speed/direction combination, while it took 19 minutes in the original FarmFlow version. This means that a complete assessment for every integer wind speed between cut-in and cut-out wind speed $V_\infty = (4:25)\,\mathrm{m/s}$ and 72 wind direction sectors of $|\Delta\theta_\infty| = 5^\circ$, would take $\sim 26\mathrm{hrs}$ with FarmFlow-fast and $\sim 500\mathrm{hrs}$ with the original version.

---

[8] The measured data is obtained from [64].

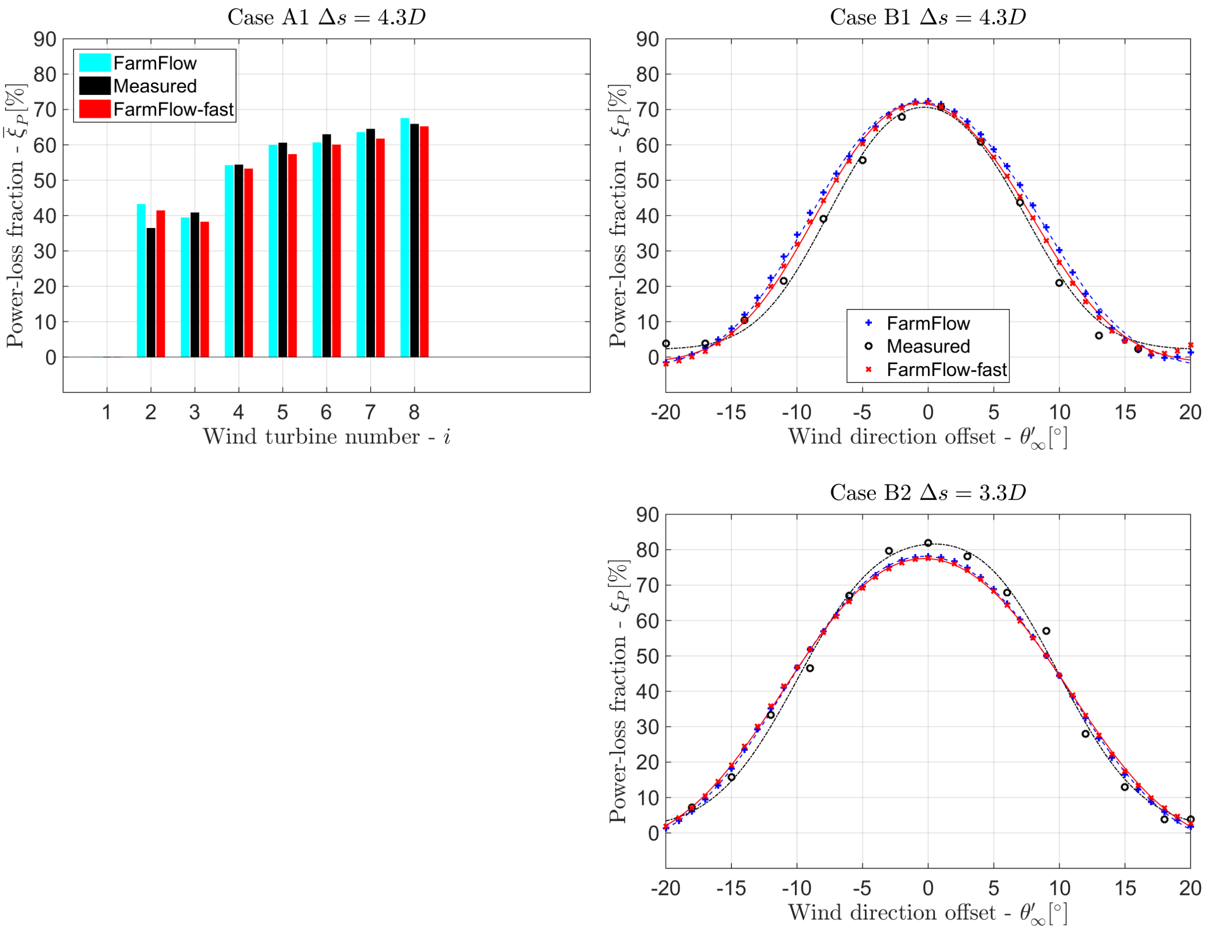

Figure 4.11: Lillgrund validation results. All validation cases concerned a velocity range of $4 < V_\infty \leq 10\mathrm{m/s}$ and a moving window of $|\Delta\theta_\infty| = 3°$. Top left: Case A1, top right: Case B1, bottom right: Case B2.

### 4.7.3. Conclusions

From the results of the validation runs, it is observed that both software versions; the original Farmflow and FarmFlow-fast, show a close agreement with the measurement data. The maximum absolute error in power-loss fraction, averaged over a $-15° \leq \theta'_\infty \leq +15°$ wind direction sector, is $|\Delta\bar{\xi}_{\mathrm{P_{SM,max}}}| = 0.050$. The maximum absolute error, per wind direction step of $|\Delta\theta_\infty| = 1°$, is $|\Delta\xi_{\mathrm{P_{SM,max}}}| = 0.063$.

It can be concluded that FarmFlow-fast does not show a worse agreement with the measurement data than the original FarmFlow version. The power-loss fraction is alternately under and over estimated by both software versions. At first sight, the simulations of the Horns Rev wind farm seem to show better agreement with the measurement data than the Lillgrund simulations. It is however hard to compare the quality of the results amongst the two wind farms, because the quality and amount of available measurement data as well as the concerned wind speed/direction combinations are not similar.

It can not be concluded whether the turbulence intensity, wind turbine spacing or wind speed range is of any influence on the quality of the simulation data. Comparison of additional validation cases is required before firm conclusions can be drawn about the influence of the aforementioned parameters on the quality of the results. With the current validation data it is demonstrated that the usage of FarmFlow-fast is a valid choice for parameter ranges close to the investigated scenarios.

**A-cases** All A-cases show that the shape of the power-loss fraction development along the wind turbine rows is similar for both software versions. Although the shape of the development is the same, differences in absolute values are recognized. The absolute differences are caused by round-off errors due to the difference in grid-dimensions. The different tuning parameters of the $k - \epsilon$-turbulence model have reduced the absolute differences. Without the tuning, the differences would have been much larger, mostly due to increased numerical diffusion in FarmFlow-fast.

For all A-cases, except for Case A3 of Horns Rev, the power-loss fraction is lower in FarmFlow-fast than in the original FarmFlow version. The maximum absolute difference between the power-loss fractions of both software versions is $|\Delta\bar{\xi}_{\mathrm{P_{FN,max}}}| = 0.026$, which is about half of the maximum difference with the measurement data.

A remarkable observation is that the power-loss fractions, found by FarmFlow-fast at a wind turbine spacing of $\Delta s = 9.4D$, are lower than the power-loss fractions calculated at a wind turbine spacing of $\Delta s = 10.4D$. This is most probably caused by the larger wind turbine spacing in the direction perpendicular to the wind direction. The larger perpendicular spacing causes downstream wind turbines to profit from the increased wind speed close to the edge of wind turbine wakes.

The wind speed increments are a result of the steady Navier-Stokes equations, solved by FarmFlow-fast. The effects of the increasing wind speed are in reality less observable, due to unsteady processes causing wind direction changes and wind speed variations. Unsteady processes are not taken into account by the steady Navier-Stokes equations of the FarmFlow-fast wake model. Average power generation simulations over a wide range of wind directions can correspond very well to measurement data, but errors can originate if smaller wind direction sectors are investigated and peaks in the power generation simulation results are not properly smoothed out.

**B-cases** All B-cases show that the shape of the power-loss fraction curves over the $-20^\circ \leq \theta'_\infty \leq +20^\circ$ range is similar for both software versions. The maximum absolute difference in power-loss fraction is $|\Delta\xi_{\mathrm{P_{FN,max}}}| = 0.032$. The absolute difference between both software versions is about half the difference with the measurement data, just like in the A-cases.

As becomes clear from Case B1 of Horns Rev and Case B1 of Lillgrund, wind direction uncertainty is not correctly taken into account. On average, the simulation results seem to correspond very well to the measurement data. Simulating for small wind direction ranges within a wind direction offset of $+15^\circ \leq \theta'_\infty \leq +20^\circ$ however, seems to overestimate the power generation of the wind turbines.

Another issue to reconsider is the assumed wind direction standard deviation of $\sigma_\theta = 2.5^\circ$. The chosen standard deviation seems to be an acceptable choice for the purpose of the concerned validation cases, but this does not guarantee that it is a valid approach for other scenarios. The wind direction standard deviation influences the averaged peak power-loss fraction and the wake expansion.

The following conclusions are drawn from the validation study:

- It must be kept in mind that the power generation data in this validation study is averaged over a number of wind directions and wind speeds. If the averaged simulation and measurement data show a good agreement with each other, it does not imply that the tool is performing equally well for smaller wind direction sectors and wind speed ranges. Especially if peaks in the power-loss fraction as function of the wind direction are investigated or when small wind direction sectors are taken into account, the validity of the simulations can not be guaranteed.

- An agreement in power-loss fraction values between measurement data and simulations does not guarantee that the absolute power generation values are properly calculated. This is because the power-loss fraction is calculated with respect to the power generation of a wind turbine exposed to free-stream conditions. The power generation value of the free-stream wind turbine is different for the FarmFlow-fast simulations than for the measurements, making it not a fixed reference value. The absolute power generation values become important if the AEP of a wind farm has to be calculated.

- FarmFlow-fast provides acceptable results for the investigated validation cases. It is capable to be used for optimization purposes, involving wind farm-wake calculations. It is however recommended to validate the results of a FarmFlow-fast optimization run with the original version of FarmFlow. If AEP calculations need to be performed, it is also recommended to use the original FarmFlow version.

- The quality of both FarmFlow-fast and the original FarmFlow version is worse for wind directions generating a wake that narrowly passes downstream wind turbines. Wind turbines close to the edge of the wake experience higher rotor-averaged wind speeds and generate more power than the upstream wind turbine. This phenomenon is not observed in reality, due to unsteady aerodynamic processes in the wind causing wind direction changes and wind speed variations. The wind direction changes and wind speed variations cause the actual average wind speed experienced by the wind turbines in the wake to be lower than the wind speed calculated by the steady Navier-Stokes equations.

- The influence of the ambient turbulence intensity, wind turbine spacing and the wind speed range on the quality of the results can not be judged. More validation cases have to be investigated for getting a better impression of these influences. Investigation of more validation cases requires additional measurement data.
- FarmFlow-fast is approximately 19 times quicker than the original version. A full assessment of a wind farm taking a complete day might however still be considered too long, especially when multiple assessments need to be carried out.
- It may be considered use parallel processing, by using all processors in a computer simultaneously instead of using only one processor. The calculation time can be reduced by a factor four with the laptop used for the validation cases, but a computer cluster can run even more processes in parallel.

# 5

# Theory and methodology of the optimization problems

This chapter describes the theory and methodology of the optimization problems. Section 5.1 starts with the governing equations for creating wind turbine performance curves, AEP calculation and calculation of power-loss and energy-loss fractions. Hereafter, Section 5.2 continues with the description of the optimization cases including their purpose, wind farm layouts and wind conditions, optimization parameters and the optimization problem formulation.

## 5.1. Governing equations

### 5.1.1. Assumptions

As discussed in Section 3.2.2, wind turbines are modelled as permeable actuator disks in FarmFlow-fast. Relevant actuator disk model equations, applicable to the optimization problems, are given by Equations (3.3) to (3.6). For the sake of optimization problem simplification, it is assumed that the actuator disks operate without wind turbine losses. Neglecting wind turbine losses means that no power-loss factor is applied to Equation (3.6).

By neglecting wind turbine losses, wake effects are the only contribution to the power losses that remain in wind farm simulations. As wake effects are the only cause of power losses, the governing equations are appropriate for wake loss investigation.

### 5.1.2. Performance curve parametrization

Three different performance curve parametrization methods are used in the optimization problems. The first parametrization method uses a constant axial induction factor value for all wind speeds below rated wind speed. Above rated wind speed, the axial induction factor is reduced such that the power generation of the wind turbine is limited to rated power.

The second method specifies discrete axial induction factor points at rotor-averaged wind speed intervals of $|\Delta u_\infty| = 1\mathrm{m/s}$. The third method uses Bézier control points to define the axial induction factor curve. A description of the methods is given in the paragraphs below.

**Fixed axial induction factor** As the axial induction factor has a constant value when using the 'fixed axial induction factor' method, the rated wind speed of the wind turbines can be calculated from Equation (5.1). Equation (5.1) is obtained from rewriting Equation (3.6).

$$u_{\mathrm{rated}} = \sqrt[3]{\frac{2P_{\mathrm{rated}}}{\rho\pi D^2 a\left(1-a\right)^2}} \tag{5.1}$$

The FarmFlow-fast performance curve inputs are specified at each $|\Delta u_\infty| = 0.25\mathrm{m/s}$ wind speed step in the $V_{\mathrm{in}} < u_\infty \leq V_{\mathrm{out}}$ range. Next to the uniformly distributed data points, the rated wind speed is submitted as an additional point. For all specified wind speeds in the $V_{\mathrm{in}} < u_\infty \leq u_{\mathrm{rated}}$ range, the

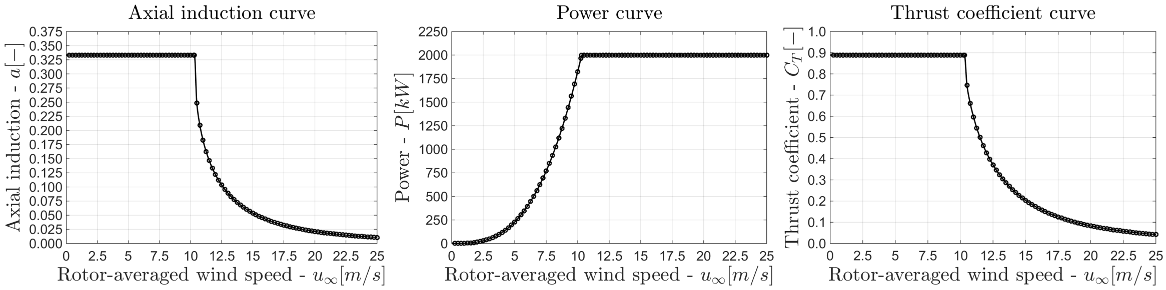

Figure 5.1: Performance curves of the Betz wind turbines. Left: axial induction, center: power, right: thrust coefficient.

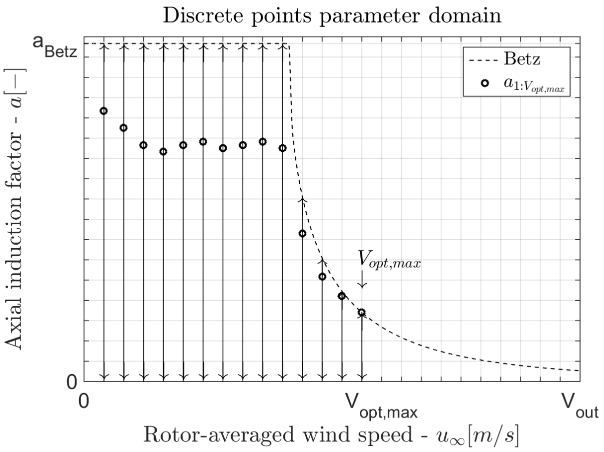

Figure 5.2: Discrete points axial induction factor curve parametrization and parameter bounds. The vertical arrows indicate the domain over which the axial induction points are allowed to move.

axial induction factor curve has a fixed value $a$. The power curve in the same range is calculated from Equation (3.6).

All data points on the power curve in the $u_{\text{rated}} < u_\infty \leq V_{\text{out}}$ range are limited to rated power. The axial induction factors in the same range are calculated by solving Equation (3.6) for $a$, in each specified wind speed point. The complete thrust coefficient curve is calculated from Equation (3.3), based on the axial induction factor curve.

A wind turbine operating at the 'Betz' limit has an axial induction factor of $a = a_{\text{Betz}} = \frac{1}{3}$, which is the optimum axial induction factor for a stand-alone wind turbine[67]. The Betz performance curves of a wind turbine with a rotor diameter of $D = 80\text{m}$, a rated power of $P_{\text{rated}} = 2.0\text{MW}$, a cut-in wind speed of $V_{\text{in}} = 0\text{m/s}$ and a cut-out wind speed of $V_{\text{out}} = 25\text{m/s}$ are shown in Figure 5.1. In Figure 5.1, the black circles represent the data points implemented in FarmFlow-fast and the black lines are a result of interpolation between the data points with the PCHIP method.

**Parametrization by discrete points** The axial induction factor curve is with the 'discrete points' method parametrized by discrete points at $|\Delta u_\infty| = 1\text{m/s}$ intervals, using integer rotor-averaged wind speeds. The axial induction points are variable for $u_\infty \leq V_{\text{opt,max}}$ and the points $u_\infty > V_{\text{opt,max}}$ are kept at the values of the Betz curve. The statements above imply that the axial induction factor curve is defined by $V_{\text{opt,max}}$ parameters; $\mathbf{a} = a_{\text{u}_\infty}$, with $u_\infty = 1 : V_{\text{opt,max}}$. The velocity $V_{\text{opt,max}}$ can be arbitrarily chosen, but in optimization problems it is recommended to set $V_{\text{opt,max}}$ to the highest wind speed for which wake losses occur in a wind farm. This is further explained in Section 5.2.

In order limit the power curve of the wind turbine to rated power, the axial induction points are bounded between zero and the Betz curve. This means that the axial induction points can move vertically over the ranges specified in Figure 5.2[1], between the $a = 0$ axis and the Betz curve. The example values of the discrete axial induction factor points are only used for illustrative purposes.

---

[1] The axial induction factor at $u_\infty = 0\text{m/s}$ is assumed to be similar to the axial induction factor at $u_\infty = 1\text{m/s}$; $a_0 = a_1$.

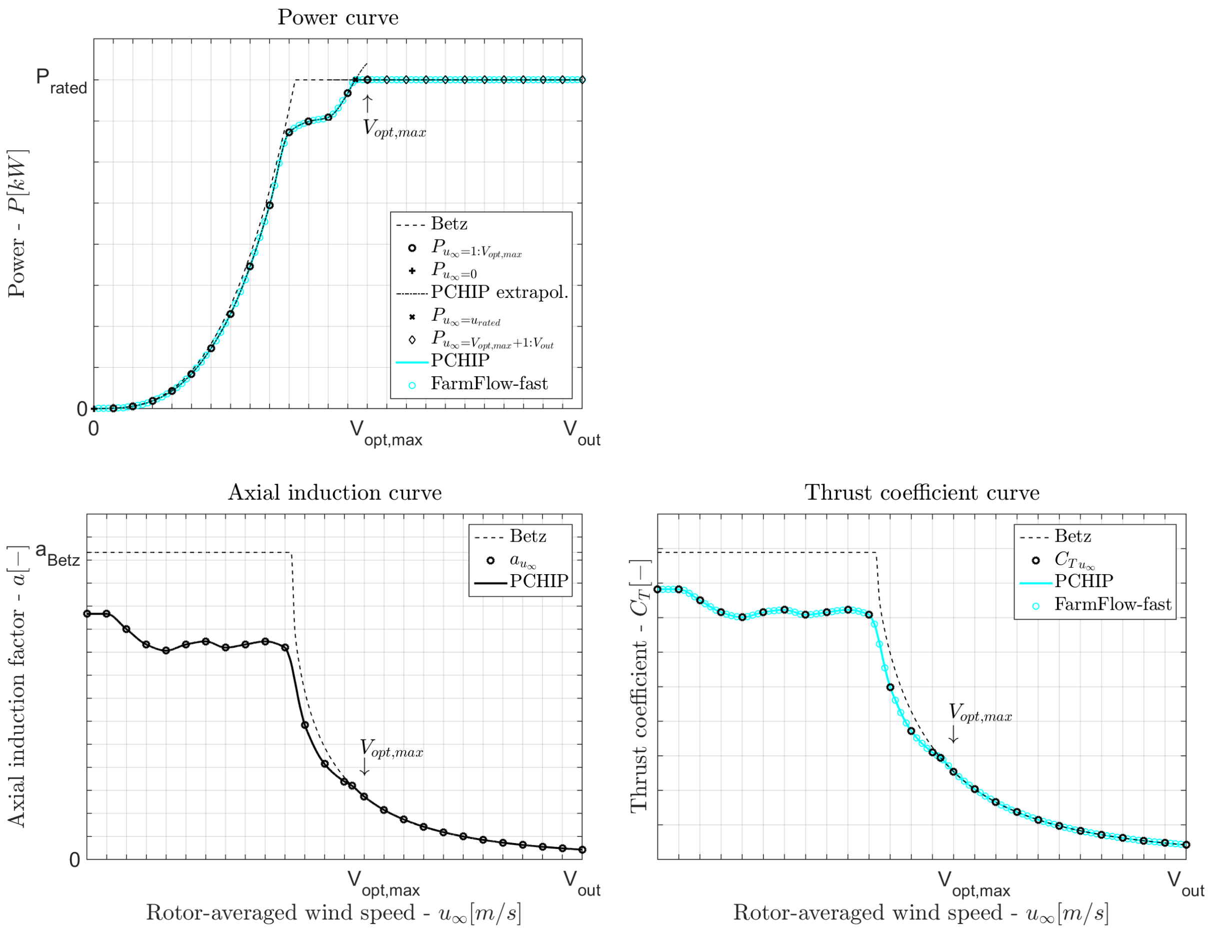

Figure 5.3: Procedure for creating FarmFlow-fast performance curves by the discrete points parametrization method. Top left: PCHIP extrapolation through the power points calculated from the discrete axial induction factor points and the $P_{u_\infty=0}$ point, for estimation of the rated wind speed. After adding the rated wind speed and the other rated power points, the FarmFlow-fast implementation points are obtained by PCHIP interpolation. Bottom left: all axial induction factor points and the interpolated curve. Bottom right: all thrust coefficient points, the interpolated curve and the FarmFlow-fast implementation points.

The procedure for creating power and thrust coefficient curves for FarmFlow-fast, from the example axial induction factor points, is displayed in Figure 5.3. First, the axial induction points are converted to power values by Equation (3.6) and an additional point is added at $u_\infty = 0\mathrm{m}/s$. The power points are displayed in the top left graph of Figure 5.3.

A PCHIP extrapolation is performed with the power points below rated power, to estimate the rated wind speed. By adding the rated wind speed point to the power points and adding the remaining rated power points, the complete power curve is obtained by using all points in a PCHIP interpolation. Adding the rated wind speed point is necessary to reduce round-off errors; otherwise the optimization process will try to reduce the negative effects of round-off errors, instead of actually improve the wind farm performance.

From the power points, the axial induction points are calculated by solving Equation (3.6) for $a$ at each rotor-averaged wind speed. This procedure yields the axial induction points displayed at the bottom left of Figure 5.3. From the axial induction points, the thrust coefficient curve is calculated by Equation (3.3) as shown in the bottom right graph of Figure 5.3. The points that are implemented in FarmFlow-fast are obtained from PCHIP interpolation between the black points displayed in the top left and bottom right graphs of Figure 5.3. The FarmFlow-fast implementation points are shown as cyan circles.

**Parametrization by Bézier control points** The axial induction curve is with the 'Bézier control points' method defined by a pre-specified number of Bézier control points. The papers [68, 69] ex-

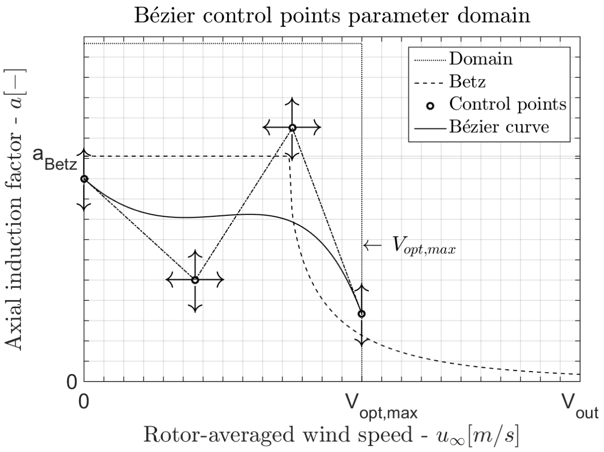

Figure 5.4: Bézier control points axial induction factor curve parametrization and parameter bounds. The arrows indicate the directions in which the control points are allowed to move.

plain how Bézier curves are generated from control points. The application of Bézier control point parametrization in the current project is explained in Figures 5.4 and 5.5. The number of example control points and their locations are arbitrarily chosen and are only used for illustrative purposes.

Figure 5.4 shows four Bézier control points in the design space. The arrows indicate the directions in which the control points are allowed to move. The end points at $u_\infty = 0\mathrm{m/s}$ and $u_\infty = V_{\text{opt,max}}$ are allowed to move only vertically, while all other points can move both vertically and horizontally. The solid black line is the Bézier curve, which is created from the control points.

In order to limit the power curve of the wind turbine to rated power, the axial induction curve should stay below the Betz curve. As shown by Figure 5.4, the axial induction factor curve does not stay below the Betz curve in the current example. The points on the Bézier curve beyond the crossing with the Betz curve are replaced by the values of the Betz curve. The crossing point is determined by PCHIP extrapolation through the points below the Betz curve. Below it is described how this is done.

In the top left graph of Figure 5.5, it is shown that the data points on the axial induction Bézier curve of Figure 5.4 are converted to power points by using Equation (3.6). Part of the data points on the power curve have values above rated power. After discarding those points, PCHIP extrapolation is used with the points below rated power to estimate the rated wind speed. The rated wind speed is indicated by the '□'-symbol, at the top left of Figure 5.5.

Adding rated wind speed and the remaining rated power points to the power points below rated power, yields data points that can directly be implemented into FarmFlow-fast. Interpolating between the data points with the PCHIP method yields the solid cyan power curve, displayed in the top left graph of Figure 5.5.

From the data points on the power curve, the axial induction factor points are calculated by solving Equation (3.6) for $a$ as shown in the bottom left graph of Figure 5.5. Finally, the data points on the thrust coefficient curve are calculated by applying Equation (3.3) to the axial induction factor points as shown in the bottom right graph of Figure 5.5. The data points of the thrust coefficient curve can also directly be used as input for FarmFlow-fast.

### 5.1.3. Calculation of the AEP

The annual energy yield of a wind farm is calculated by summation of the yearly energy production of every individual wind turbine, as shown in Equation (5.2). The yearly energy production of an individual wind turbine is calculated by integrating the wind turbine's power generation over all wind speeds and directions, occurring during one year. The probability of occurrence of a specific wind speed/direction combination is specified by the wind rose and the Weibull wind speed distributions.

$$AEP = T_{\text{year}} \sum_{i=1}^{N_{\text{wt}}} \int_{0}^{2\pi} \int_{V_{\text{in}}}^{V_{\text{out}}} p\left(V_\infty, \theta_\infty\right) P_{\text{i}}\left(V_\infty, \theta_\infty\right) \mathrm{d}V_\infty \mathrm{d}\theta_\infty \tag{5.2}$$

In Equation (5.2), $p\left(V_\infty, \theta_\infty\right)$ represents the probability of occurrence of the undisturbed wind speed,

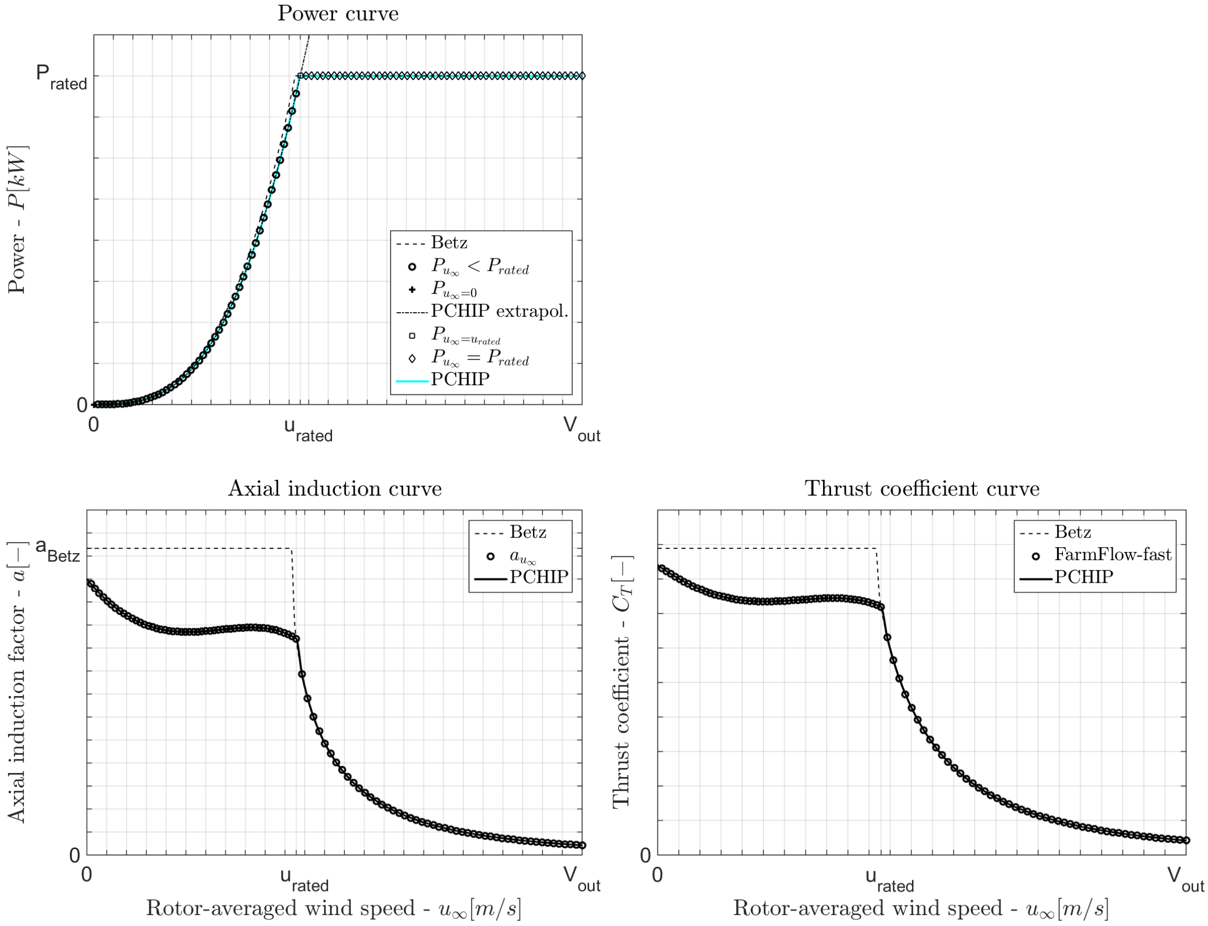

Figure 5.5: Procedure for creating FarmFlow-fast performance curves by the Bézier control points method. Top left: PCHIP extrapolation through the power points below rated power and the $P_{u_\infty=0}$ point, for estimation of the rated wind speed. After adding the rated wind speed and the other rated power points, the FarmFlow-fast implementation points are obtained by PCHIP interpolation. Bottom left: all axial induction factor points and the interpolated curve. Bottom right: FarmFlow-fast thrust coefficient data points and the interpolated curve.

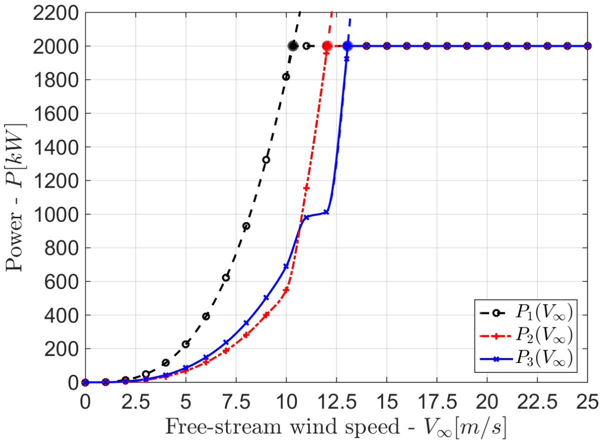

Figure 5.6: Power generation per wind turbine, as function of the undisturbed wind speed. The discrete simulation points, the PCHIP extrapolations through the simulation points, the extrapolation crossings and the resulting continuous functions are displayed.

$V_\infty$, and wind direction, $\theta_\infty$, combination. $P_i$ is the power generation of an individual wind turbine as function of the undisturbed wind speed and direction and $N_{\text{wt}}$ is the number of wind turbines. The expression is multiplied with the number of hours per year, $T_{\text{year}} = 8766\text{hrs}$, such that the AEP is expressed in kilowatt-hours, $[\text{kWh}]$, if $P_i$ is expressed in kilowatts, $[\text{kW}]$.

The power generation of a wind turbine in FarmFlow-fast depends on the rotor-averaged wind speed; $u_\infty$. The rotor-averaged wind speed results from the behaviour of wakes through the wind farm and is different for each wind turbine.

The AEP without wake losses is calculated by the expression shown in Equation (5.3). The power generation without wake losses, $P_{\text{ref}}$, is estimated by using power generation values of a Betz wind turbine facing undisturbed meteorological conditions.

$$AEP_{\text{no loss}} = T_{\text{year}} N_{\text{wt}} \int_0^{2\pi} \int_{V_{\text{in}}}^{V_{\text{out}}} p\left(V_\infty, \theta_\infty\right) P_{\text{ref}}\left(V_\infty, \theta_\infty\right) \mathrm{d}V_\infty \mathrm{d}\theta_\infty \tag{5.3}$$

Below, an example is given of the AEP calculation procedure of a wind farm consisting of $N_{\text{wt}} = 3$ wind turbines. The power and thrust coefficient curve, implemented in FarmFlow-fast for the example simulations, are displayed in Figure 5.1. Only one wind direction is concerned, which is aligned with a row of three wind turbines. It is assumed that the wind is continuously coming from this direction, meaning 8766 hours per year.

Since all undisturbed wind speeds in the $V_{\text{in}} < V_\infty \leq V_{\text{out}}$ range are concerned, all integer free-stream wind speeds between cut-in and cut-out velocity are simulated in FarmFlow-fast. The discrete power generation values per wind turbine, as function of the undisturbed wind speed, are represented by the small marks in Figure 5.6. From the graph it can be concluded that power generation values are lower at wind turbines 2 and 3 than at wind turbine 1, for the same free-stream wind speed.

Although the shape of the power generation curves becomes clear from the discrete simulation points, the points do not constitute a continuous function. AEP calculation with Equation (5.2) however, requires continuous integration of the power generation per wind turbine over the free-stream wind speed range $V_{\text{in}} \leq V_\infty \leq V_{\text{out}}$.

Generating a continuous function from the discrete power values is established by using the PCHIP method. Forward extrapolation is applied to the data points below rated power, $P_i\left(V_\infty\right) < P_{\text{rated}}$, and backward extrapolation to the data points equal to rated power, $P_i\left(V_\infty\right) = P_{\text{rated}}$. In this way, the point where both extrapolations cross can be found as shown by the thick marks in Figure 5.6. The crossings are the points where rated power is first established for each wind turbine, which are the rated free-stream wind speeds; $V_{\infty,\text{rated,i}}$. Adding the points $\left[V_{\infty,\text{rated,i}} \quad P_{\text{rated}}\right]$ to the simulation results and interpolating between all data points with the PCHIP method, yields the continuous power generation functions shown in Figure 5.6.

With the continuous power generation curves and a continuous Weibull wind speed curve, the AEP can be calculated by using Equation (5.2). The methodology for estimating the AEP is described below.

The explanation uses an example Weibull wind speed curve with a scale factor of $A = 10.6\mathrm{m/s}$ and a shape factor of $\mathrm{k} = 2.33$.

- The first step in the AEP calculation is the multiplication of the Weibull wind speed curve with the continuous power generation curves of the wind turbines. The Weibull distribution used for this purpose is the probability density function in number of hours per year, such that $T_{\mathrm{year}}$ is taken inside the integral of Equation (5.2). The multiplication of the curves is shown in Figure 5.7; the Weibull distributions at the top are multiplied with the power generation curves in the middle, yielding the energy density distributions at the bottom of the figure. From left to right, wind turbines 1, 2 and 3 are displayed.

- The second step is to integrate the energy density curves over the complete operational wind speed range; $V_{\mathrm{in}} \leq V_{\infty} \leq V_{\mathrm{out}}$. Integration of the individual energy density curves yields the cumulative AEP distribution curves in the left graph of Figure 5.8.

- The third step is to sum the integrated AEP values per wind turbine. This is done by adding the values at $V_{\infty} = V_{\mathrm{out}}$ of the cumulative AEP distribution curves. The sum of the yearly energy productions of the individual wind turbines is displayed at the right side of Figure 5.8.

The total AEP of the three Betz wind turbines is calculated by the above explained procedure to be $AEP_{\mathrm{Betz}} = 24.6\mathrm{GWh}$. The AEP without wake losses is calculated by multiplying the AEP of the first (free-stream) wind turbine, $AEP_1$, with the number of wind turbines, $N_{\mathrm{wt}}$, as shown by Equation (5.4).

$$AEP_{\mathrm{no\ loss}} = N_{\mathrm{wt}} AEP_1 = 32.0\mathrm{GWh} \tag{5.4}$$

### 5.1.4. Calculation of the power-loss and energy-loss fractions

Wake losses become apparent if the wind direction is aligned with a row of wind turbines. The power-loss fraction of a wind turbine is defined as the fractional loss in power generation, compared to a wind turbine facing undisturbed meteorological conditions. The mathematical expression for the power-loss fraction of a wind turbine is given by Equation (4.6).

The average power-loss fraction of a wind turbine row or complete wind farm is defined as the fractional loss in accumulated power generation of all wind turbines, due to wake effects. The power-loss fraction of a wind turbine row is calculated by comparing the cumulative power generation of all wind turbines together, with the power that would have been generated by the same number of Betz wind turbines exposed to free-stream meteorological conditions. The mathematical expression for the average power-loss fraction of a wind turbine row is given by Equation (5.5).

$$\xi_{\mathrm{P,row}} = 1 - \frac{\sum_{i=1}^{N_{\mathrm{wt}}} P_{\mathrm{i}}}{N_{\mathrm{wt}} P_{\mathrm{ref}}} \tag{5.5}$$

If wind turbines are assumed to operate under ideal conditions, i.e. without operational losses and shut-downs, then the only energy losses in a wind farm are caused by wake effects. The energy-loss fraction is mathematically expressed by Equation (5.6). Equation (5.6) calculates the fractional energy loss between the actual actual AEP and the AEP without wake losses.

$$\xi_{\mathrm{AEP}} = 1 - \frac{AEP}{AEP_{\mathrm{no\ loss}}} \tag{5.6}$$

From the values of the AEP and the AEP without wake losses obtained by Equations (5.2) and (5.3), the average energy-loss fraction of a wind farm can be calculated with Equation (5.7).

$$\xi_{\mathrm{AEP,farm}} = 1 - \frac{\sum_{i=1}^{N_{\mathrm{wt}}} AEP_{\mathrm{i}}}{N_{\mathrm{wt}} AEP_{\mathrm{ref}}} \tag{5.7}$$

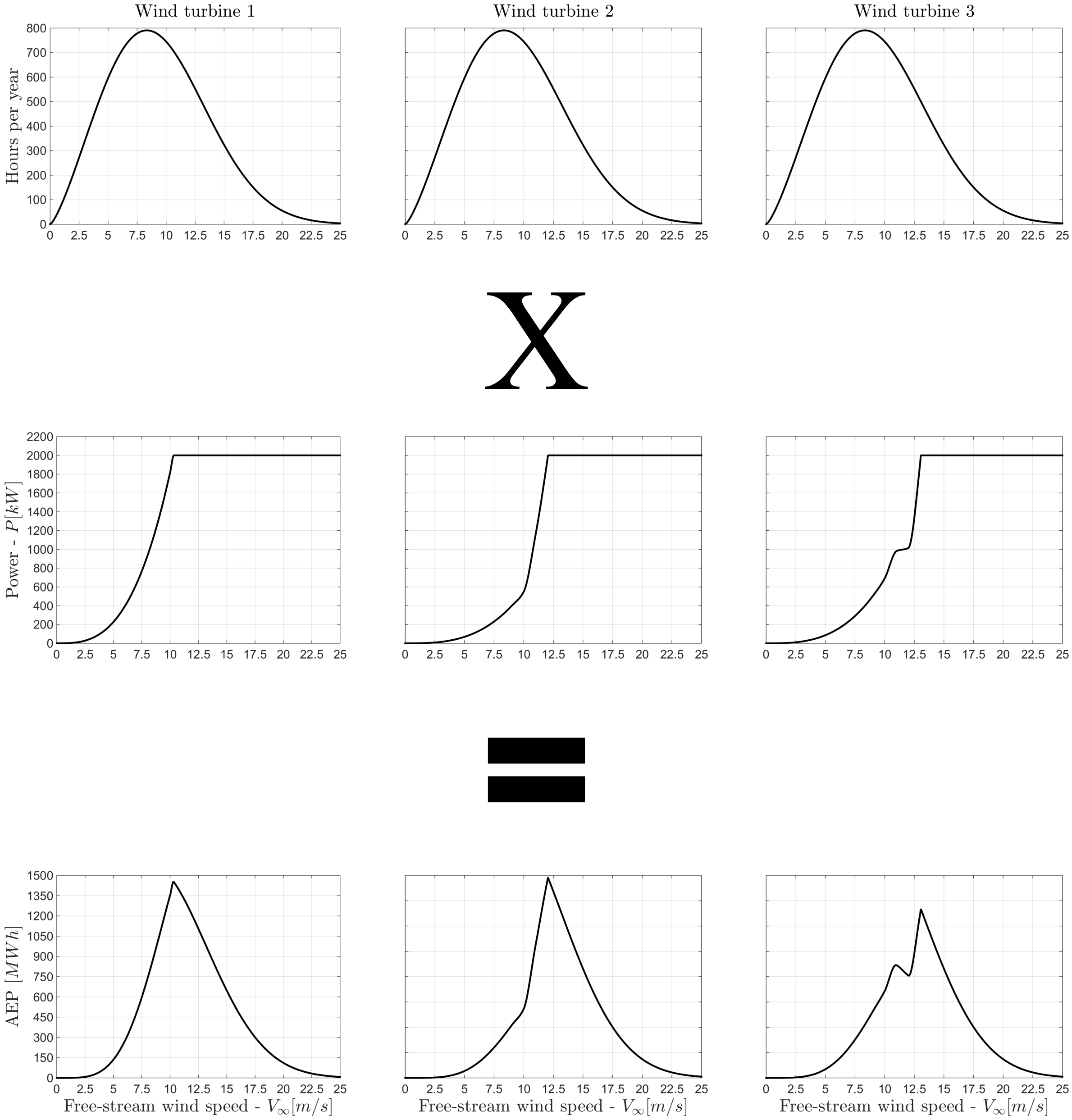

Figure 5.7: Example of the AEP calculation. From left to right wind turbines 1, 2 and 3 are displayed. Top: Weibull probability density function of the free-stream wind speed in number of hours per year, middle: wind turbine power generation as function of free-stream wind speed, bottom: AEP density.

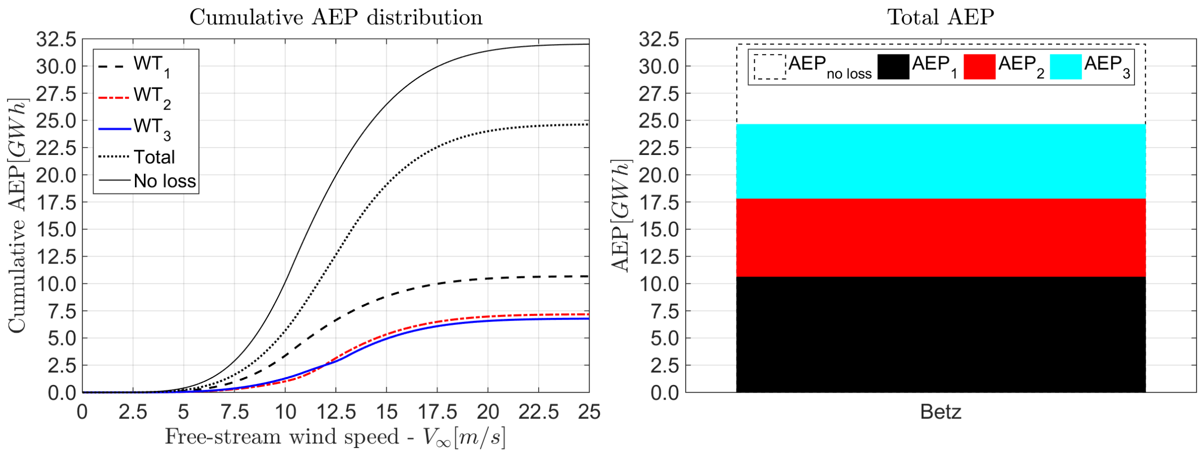

Figure 5.8: AEP example of three Betz wind turbines. Left: cumulative AEP as function of free-stream wind speed, right: total AEP.

## 5.2. Description of the optimization problems

### 5.2.1. Overview

This section describes the optimization problems. As stated in Section 1.3, two different optimization problems are investigated; the axial induction factor optimization problem and the performance curve optimization problem.

**Axial induction factor optimization** The axial induction factor optimization problem deals with power-loss fraction minimization of a wind turbine row, with an aligned wind direction. The wind turbines are oriented along a straight line and a single constant wind speed is concerned. The axial induction factor optimization problem can be considered as a simplified, unconstrained, verifiable worst case scenario optimization problem, with few optimization parameters.

One axial induction factor optimization case is defined, which is presented in Section 5.2.2. The case is used to investigate the suitability of five different optimization algorithms for wind turbine performance curve optimization. The assessed optimization algorithms are described in Appendix B.

**Performance curve optimization** The performance curve optimization problem involves energy-loss fraction minimization by optimization of complete wind turbine performance curves, in the $V_{\text{in}} \leq u_\infty \leq V_{\text{out}}$ range. The performance curve optimization problem is more complex than the axial induction factor optimization problem. The performance curve optimization problem uses more optimization parameters and in addition to parameter bounds, also linear and non-linear constraints are imposed. The performance curve optimization problem has a wider applicability range and provides more insight into the possibilities of wind turbine performance curve optimization.

Six performance curve optimization cases are defined, which are presented in Sections 5.2.3 to 5.2.8. Different scenarios are investigated concerning wind directions: either one wind direction aligned with a single wind turbine row, or the complete wind rose of a square symmetrical wind farm is concerned. The *patternsearch* algorithm[70] is used for all performance curve optimization cases. Different termination criteria, algorithm settings and performance curve parametrization methods are compared with each other and the wind farm layout is varied. Finally, the impact of free-stream wind turbine performance curves on the energy production of a complete wind turbine row is investigated.

**Boundary conditions** The wind turbine dimensions in all optimization cases are equal to the dimensions of the Vestas V80, which is used in the Horns Rev wind farm. The rotor diameter is $D = 80\text{m}$ and the hub height is $z_{\text{hub}} = 70\text{m}$. The cut-out velocity of the wind turbines is $V_{\text{out}} = 25\text{m/s}$ and the rated power is $P_{\text{rated}} = 2.0\text{MW}$, both similar to the Vestas V80.

As wind turbine losses are neglected, the cut-in velocity is assumed to be $V_{\text{in}} = 0\text{m/s}$. The tip-speed ratio of the wind turbines is $\lambda = 6$ and the maximum tip-speed is $V_{\text{tip,max}} = 78\text{m/s}$. The minimum

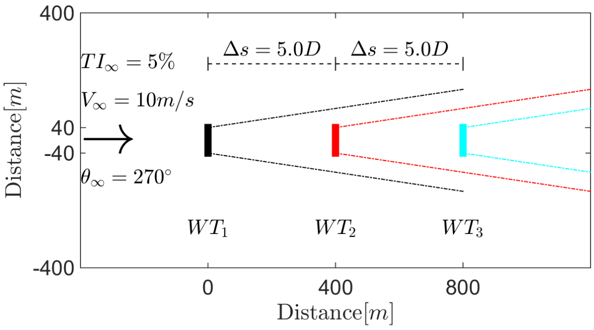

Figure 5.9: Top view of axial induction factor optimization problem Case A1.

distance between the wind turbines is $\Delta s = 400\mathrm{m} = 5.0D$ for all optimization cases, irrespective of the wind farm layout.

The wind rose is uniformly distributed, with a Weibull scale and shape factor of respectively $A = 10.6\mathrm{m}/s$ and $k = 2.33$. The wind speed distribution corresponds to the average Weibull distribution of the Horns Rev wind farm, as shown by the thick solid black line at the left side of Figure 4.4. In optimization cases involving a single wind direction, it is assumed that the wind is always aligned with the orientation of the wind turbine row. The ambient turbulence intensity at all wind speeds and directions is assumed to be $TI_\infty = 5\%$.

The uniform wind climate is chosen to simplify the post-processing procedure for AEP estimation and to keep overview during comparisons between energy-loss fractions from different wind directions. The uniform character of the wind climate ensures that a simulation for a wind direction in a square symmetrical wind farm gives results that can be reused for other wind directions. This reduces the number of wind directions that need to be simulated.

### 5.2.2. Case A1: Optimization algorithm analysis

**Purpose** The purpose of Case A1 is to gain insight into the working procedure and functioning of different optimization algorithms. The performance of the algorithms is assessed by analysis of the reduction in power-loss fraction, the extent to which the algorithm converges to the global optimum from different starting points and the total optimization time. Case A1 is investigated to determine which algorithm can be best used for performance curve optimization. The wind farm layout, objective function, constraints and other relevant information are presented in the upcoming paragraphs.

**Wind farm layout, wind direction and wind speed** The current case involves a row of three wind turbines with an equal distance between them, as shown in Figure 5.9. The wind direction is aligned with the row, $\theta_\infty = 270°$.

Running simulations for all integer wind speeds in the $V_{\mathrm{in}} < V_\infty \leq V_{\mathrm{out}}$ range with unoptimized Betz wind turbines[2], yields the graphs in Figure 5.10. The graphs show the power generation of the wind turbines and the power-loss fraction of the complete wind turbine row; both as function of free-stream wind speed. The power-loss fraction of the row is calculated by Equation (5.5), where $P_{\mathrm{ref}}$ is the power generation of the first wind turbine along the row.

As stated in Section 2.2, wake effects are most severe in the region around rated wind speed. Figure 5.10 shows that this statement is correct; the maximum absolute power-loss occurs at $V_\infty = 10\mathrm{m}/s$, which is just below rated wind speed.

The power-loss fraction however, is continuous for all wind speeds below rated wind speed. In reality, a maximum power-loss fraction would be expected around rated wind speed. The constant power-loss fraction for wind speeds below rated wind speed is caused by the assumption that the turbulence intensity is constant over all wind speeds. In general, the turbulence intensity has a minimum value around rated wind speed[11].

The free-stream wind speed for the current optimization case is chosen to be $V_\infty = 10\mathrm{m}/s$, on the basis of the simulations with the unoptimized Betz wind turbines. The low ambient turbulence intensity, the small wind turbine spacing and the particular wind speed/direction combination are chosen such

---

[2] The FarmFlow-fast performance curves for running the simulations are shown in Figure 5.1

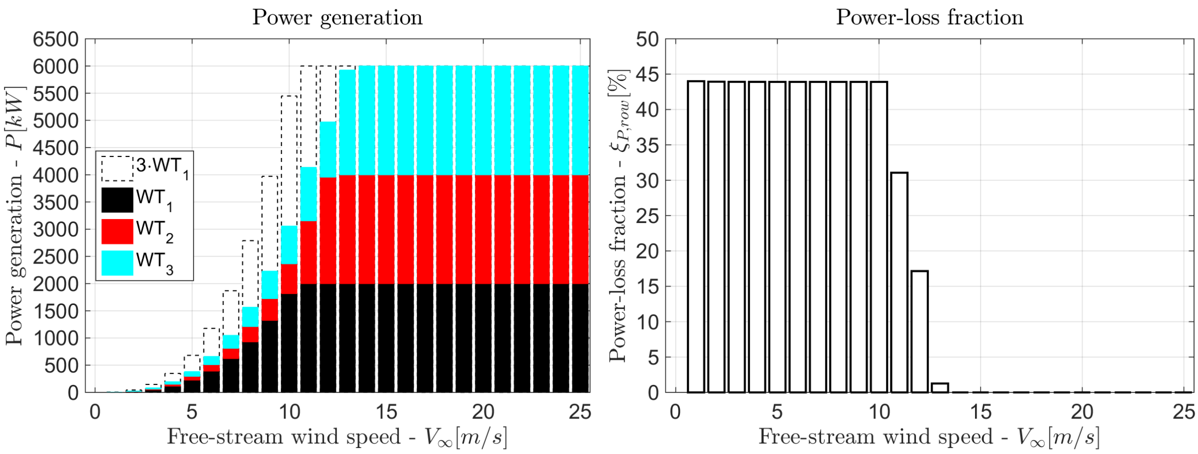

Figure 5.10: Results of the FarmFlow-fast simulations with the unoptimized Betz wind turbines, as function of integer free-stream wind speed. Left: power generation, right: power-loss fraction.

that wake effects are most severe. In this 'worst-case' scenario, the biggest difference in power-loss fraction is expected between the unoptimized Betz performance curves and the optimum wind turbine performance curves.

**Optimization parameters** The wind turbine performance curves are parametrized by the fixed axial induction factor method[3], in the current case. The power-loss fraction of the wind turbine row is minimized by optimizing the performance curves of the first two wind turbines. The two optimization parameters are the axial induction factors of the first and the second wind turbine; respectively $a_1$ and $a_2$. The third wind turbine keeps operating at Betz conditions, $a_3 = a_{\text{Betz}} = \frac{1}{3}$.

Since only two optimization parameters are involved; $a_1$ and $a_2$, the case is suitable for design space exploration and for visualization of results. It is possible to investigate a broad domain of parameter values at a high resolution. From such an investigation, insight is obtained in the layout of the design space and the location of optimum parameter values. With this information in mind, it can be judged whether the performance of an optimization algorithm is satisfactory or not.

**Optimization problem formulation** As stated before, the goal of the axial induction factor optimization problem is to minimize the power-loss fraction of the wind turbine row, which is calculated by Equation (5.5). As explained in the previous paragraph, the only two optimization parameters involved are the constant axial induction factor values of wind turbine 1 and 2.

The constraints of the optimization problem are that the thrust and power coefficients of the wind turbines should be positive and that Betz theory is only valid for axial induction factors $a \leq \frac{1}{2}$[67]. For $C_{\text{T}}$ and $C_{\text{P}}$ to be positive, the axial induction factor should be in the $0 \leq a \leq 1$ range; $C_{\text{T}} = 4a(1-a) \geq 0 \rightarrow 0 \leq a \leq 1$, $C_{\text{P}} = 4a(1-a)^2 \geq 0 \rightarrow a \geq 0$. By enforcing both previously mentioned constraints, the axial induction factor parameter values should be within the range $0 \leq a_{\text{i}} \leq \frac{1}{2}$. In this way, the constraints are implicitly enforced by parameter bounds.

Based on the statements above, the optimization problem is defined by Equation (5.8).

---

[3] See Section 5.1.2 for a description of the performance curve parametrization methods.

$$\min_{a_1,a_2} \xi_{\mathrm{P,row}}\left(a_1,a_2\right) \tag{5.8}$$

$$\text{subject to}$$

$$0 \leq a_1 \leq \frac{1}{2}$$

$$0 \leq a_2 \leq \frac{1}{2}$$

The power-loss fraction of the unoptimized wind farm is based on $N_{\mathrm{wt}} = 3$ wind turbines operating at the Betz limit. This means that as long as the power curve stays below rated power, $P\left(u_\infty\right) < P_{\mathrm{rated}}$, the axial induction factor of all three wind turbines is $a = a_{\mathrm{Betz}} = \frac{1}{3}$.

Before any optimization run is started, Matlab and FarmFlow-fast are used to run simulations for all axial induction factor combinations in the range $0 < a_{\mathrm{i}} \leq \frac{1}{2}$ in steps of $\Delta a_{\mathrm{i}} = 0.005$. The simulations are performed to explore the design space. All possible axial induction factor combinations of the first two wind turbines are simulated; meaning $100 \cdot 100 = 10\,000$ function evaluations. The design space exploration gives an impression of the optimum parameter value locations and the possible existence of local optima.

After the design space exploration, optimization runs are performed with the five algorithms shown below. A description of the algorithms is given in Appendix B.

- *fminsearch*: unconstrained, non-linear optimization algorithm that uses the 'Nelder-Mead simplex' algorithm[71].
- *fmincon*: constrained, non-linear gradient-based optimization algorithm[72–75].
- *patternsearch*: Pattern Search (PS) is a direct search method that does not require any information about the gradient of the objective function. The algorithm searches a set of points around the current point, looking for one where the value of the objective function is lower than the value at the current point[70].
- *Simulated annealing*: Simulated Annealing (SA) is a method for solving unconstrained and bound-constrained optimization problems. The method models the physical process of heating a material and then slowly lowering the temperature to decrease defects, i.e. minimizing the system energy[76].
- *Genetic algorithm*: The Genetic Algorithm (GA) is a method for solving both constrained and unconstrained optimization problems that is based on natural selection; the process that drives biological evolution[77, 78].

The optimization runs are performed with three different starting points, in order to evaluate the global convergence characteristics of the algorithms. The three different initial optimization parameter value combinations are: $\mathbf{a}_{\mathrm{init,A}} = \begin{bmatrix}\frac{1}{3} & \frac{1}{3}\end{bmatrix}$, $\mathbf{a}_{\mathrm{init,B}} = \begin{bmatrix}\frac{53}{600} & \frac{53}{600}\end{bmatrix}$ and $\mathbf{a}_{\mathrm{init,C}} = \begin{bmatrix}\frac{1}{300} & \frac{1}{300}\end{bmatrix}$. The particular initial parameter value combinations are chosen such that the *fminsearch* and the pattern search algorithm, which use fixed steps to evaluate optimization parameter values, do not end up evaluating the same parameter values during the first few iterations when starting from different points.

As five different algorithms and three different starting points are concerned, 15 optimization runs are performed for the current case. The algorithms are assessed upon objective function value decrement, optimization time and whether or not the algorithm converges to the global optimum. From the assessment, the best optimization algorithm is picked for the performance curve optimization problems.

### 5.2.3. Case B1: Convergence tolerance sensitivity analysis

**Purpose** The purpose of Case B1 is to evaluate the termination criterion of the pattern search algorithm. The termination criterion is varied in order to determine when the pattern search algorithm solution converges. Stopping the algorithm earlier can save computation time, but the algorithm should not be stopped too early as the lowest objective function value might not have been reached yet. The termination criteria are assessed upon objective function value decrement and optimization time. From the assessment, the most suitable termination criterion is determined for the remaining performance curve optimization cases.

**Wind farm layout, wind speeds and wind direction** The current case uses the same wind farm layout as Case A1; three wind turbines with a $\Delta s = 5.0D$ distance between them, as shown in Figure 5.9. A single wind direction is concerned again, which is aligned with the wind turbine row; $\theta_\infty = 270°$. This time however, the complete wind speed range $V_{\text{in}} < V_\infty \leq V_{\text{out}}$ is taken into account.

**Optimization parameters** The wind turbine performance curves are parametrized by the discrete points method[3], in the current case. The energy-loss fraction of the wind turbine row is minimized by optimizing the wind turbine performance curves. The same performance curves are assigned to all three wind turbines.

From the simulations with the Betz wind turbines in Figure 5.10, it can be concluded that the maximum discrete wind speed for which power losses occur is $V_\infty = 13\text{m/s}$. As the maximum wind speed for which wake losses occur should be located between $V_\infty = 13\text{m}/s$ and $V_\infty = 14\text{m/s}$, the maximum optimization wind speed is chosen to be $V_{opt,max} = 14\text{m/s}$. This means that Case B1 is an optimization problem with 14 optimization parameters; $\mathbf{a} = a_{\text{u}_\infty}$, with $u_\infty = 1:14$.

**Optimization problem formulation** As stated before, the goal of the performance curve optimization problem is to minimize the energy-loss fraction of a wind farm, which is calculated by Equation (5.7). As explained in the previous paragraph, the optimization parameters are the 14 discrete axial induction factor points as function of the rotor-averaged wind speed.

The constraint of the performance curve optimization problems is that the power curve should be limited to rated power. By the discrete points parametrization method, the constraint is satisfied by keeping the optimization parameters bounded between $a = 0$ and the Betz axial induction factor curve. The discrete axial induction factor parameter values should be within the range $0 \leq a_{\text{u}_\infty} \leq a_{\text{u}_\infty,\text{Betz}}$, for $u_\infty = 1:14$

Based on the statements above, the optimization problem of Case B1 is defined by Equation (5.9).

$$\begin{aligned} &\min_{a_{\text{u}_\infty=1:14}} \quad \xi_{\text{AEP,farm}} \\ &\text{subject to} \\ &\quad 0 \leq a_{\text{u}_\infty} \leq a_{\text{u}_\infty,\text{Betz}} \end{aligned} \tag{5.9}$$

The energy-loss fraction of the unoptimized wind farm is based on $N_{\text{wt}} = 3$ wind turbines operating at the Betz limit. The unoptimized Betz axial induction curve is used as starting point of the current optimization scenario. The curve is shown at the left side of Figure 5.1.

The pattern search algorithm is used for the current case, with mostly default settings. The mesh tolerance however is varied, which is the most important termination criterion of the pattern search algorithm. The mesh tolerance is the minimum distance over which the pattern search algorithm is allowed to evaluate parameter values from the current best point[70]. The standard mesh tolerance of the pattern search algorithm is $\epsilon = 10^{-6}$, but in the current case the following mesh tolerances are assessed: $\epsilon = \begin{bmatrix}10^{-2} & 10^{-3} & 10^{-4} & 10^{-5} & 10^{-6}\end{bmatrix}$.

As five different mesh tolerances are investigated and only one starting curve is concerned, five optimization runs are performed for the current case. The mesh tolerances are assessed upon objective function value decrement and optimization time. From the assessment, the most suitable mesh tolerance is used for the remaining performance curve optimization cases.

### 5.2.4. Case B2: Search strategy analysis

**Purpose** The purpose of Case B2 is to evaluate two different strategies by which the pattern search algorithm searches through the design space and eventually finds the optimum parameter values. One methodology may be more efficient than the other; resulting in either a shorter optimization time, a better global convergence or both. The strategies are assessed upon objective function value decrement, optimization time and the extent to which the search method facilitates convergence to

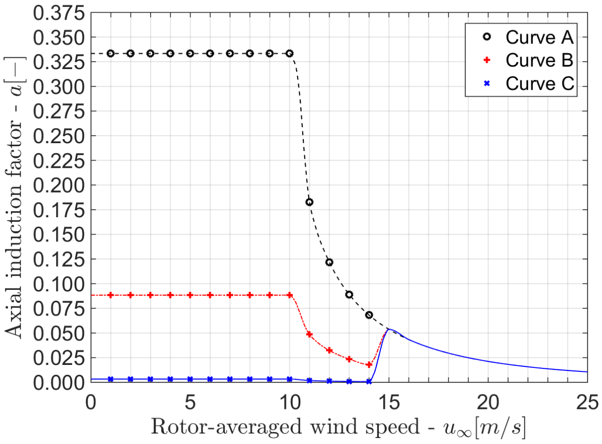

Figure 5.11: Alternatives for initial axial induction factor curves, when using the discrete points parametrization method.

the global optimum from different starting points. From the assessment, the search method for the remaining performance curve optimization cases is determined.

**Wind farm layout, wind speeds and wind direction** Case B2 closely corresponds to Case B1. The current case uses the same wind farm layout as Case A1 and B1; three wind turbines with a $\Delta s = 5.0D$ distance between them, as shown in Figure 5.9. The single concerned wind direction is aligned with the wind turbine row; $\theta_\infty = 270°$.

**Optimization parameters** The wind turbine performance curves are parametrized by the discrete points method[3], in the current case. The energy-loss fraction of the wind turbine row is minimized by optimizing the wind turbine performance curves. The same performance curves are assigned to all three wind turbines.

In line with Case B1, the maximum optimization wind speed is chosen to be $V_{\text{opt,max}} = 14\text{m}/s$. Like Case B1, the current case is an optimization problem with 14 optimization parameters; $\mathbf{a} = a_{\text{u}_\infty}$, with $u_\infty = 14\text{m}/\text{s}$.

**Optimization problem formulation** The optimization problem of Case B2 is defined by Equation (5.10), which is the same as the definition of Case B1. The explanation for the definition is given in Section 5.2.4.

$$\min_{a_{\text{u}_\infty=1:14}} \xi_{\text{AEP,farm}} \tag{5.10}$$

$$\text{subject to}$$

$$0 \leq a_{\text{u}_\infty} \leq a_{\text{u}_\infty,\text{Betz}}$$

The energy-loss fraction of the unoptimized wind farm is based on $N_{\text{wt}} = 3$ wind turbines operating at the Betz limit. The three different initial axial induction factor curves used in the current scenario are displayed in Figure 5.11.

The pattern search algorithm in the current case uses a mesh tolerance of $\epsilon = 10^{-4}$, the other algorithm settings remain at default values. The search method is however varied, which determines the number of points that are evaluated at each iteration, the directions in which the algorithm searches and according to which procedure the points are evaluated.

The default search method of the pattern search algorithm is the ‘GPSPositiveBasis2N’ method, that does not make complete polls. This strategy defines two times as many search points as optimization parameters during each iteration and the points are evaluated in fixed directions. As soon as the algorithm finds a point with a lower objective function value than the current point, the algorithm stops searching and starts a new iteration.

The other investigated method is the 'GPSPositiveBasisNp1' method that makes complete polls. This strategy defines one more search point than the number of optimization parameters during each iteration and provides more flexibility in search directions than the GPSPositiveBasis2N method. The algorithm keeps searching after it finds a better point than the current point. Once all points in an iteration are evaluated, the next iteration starts from the point with the lowest objective function value of the previous iteration.

A pattern search will generally run faster by using GPSPositiveBasisNp1 rather than using GPSPositiveBasis2N as search method, because the algorithm searches fewer points at each iteration. For problems with several local minima, it may preferable to make the pattern search evaluate all the mesh points at each iteration and choose the one with the lowest objective function value. A complete poll enables the pattern search to explore more points at each iteration and thereby potentially avoid a local minimum that is not the global minimum[70].

As two search strategies are investigated and three different starting curves are used, a total number of six optimization runs are performed. The search strategies are assessed upon objective function value decrement, optimization time and the extent to which the algorithm settings facilitate convergence to the global optimum. From the assessment, the search method for the remaining performance curve optimization problems is determined.

### 5.2.5. Case B3: Bézier control points analysis

**Purpose** The purpose of Case B3 is to reduce the optimization time, in order to also make optimization of larger wind farms and more wind directions possible in an acceptable time frame. The optimization time can be shortened by reducing the number of optimization parameters. To reduce the number of optimization parameters, Bézier control points parametrization is applied in the current case.

The number of Bézier control points is varied, in order to determine how many points are required to model the optimum axial induction factor curve. The optimization runs are assessed upon objective function value decrement and optimization time. The optimum number of control points is used for the remaining performance curve optimization problems.

**Wind farm layout, wind speeds and wind direction** The current case uses the same wind turbine row, wind speeds and wind direction as Case B1 and B2. The layout is displayed in Figure 5.9 and the wind speeds and wind direction can be found in Section 5.2.3.

**Optimization parameters** The wind turbine performance curves are parametrized by the Bézier control points method[3], in the current case. The same performance curves are assigned to all wind turbines. In line with Case B1 and B2, the maximum optimization wind speed is chosen to be $V_{\mathrm{opt,max}} = 14\mathrm{m/s}$. The number of optimization parameters in the current case depends on the number of Bézier control points, $N_{\mathrm{B}}$. The number of optimization parameters is $2N_{\mathrm{B}} - 2$, because the rotor-averaged wind speed of the first and last control point are fixed.

**Optimization problem formulation** The power constraint is satisfied by keeping the optimization parameters bounded between $a = 0$ and the Betz axial induction factor curve. The points on the Bézier curve beyond the crossing with the Betz curve are replaced by the values of the Betz curve. The control points are bounded in a domain, as shown in Figure 5.4.

The maximum allowed axial induction factor value of a control point (CP) is $a = \frac{1}{2}$ and the rotor-averaged wind speed of the control points is bounded between $u_\infty = 0$ and $u_\infty = V_{\mathrm{opt,max}} = 14\mathrm{m/s}$. Additional constraints are that the control points should remain in the same horizontal order as initially specified. Based on the statements above, the optimization problem of Case B3 is defined by Equation (5.11).

$$\min_{CP_{\mathrm{j=1:N_B}}} \xi_{\mathrm{AEP,farm}} \tag{5.11}$$

subject to

$$\begin{bmatrix} 0 & 0 \end{bmatrix} \leq CP_{\mathrm{j}} \leq \begin{bmatrix} 14 & \frac{1}{2} \end{bmatrix}$$
$$CP_{\mathrm{j}}(1) < CP_{\mathrm{j+1}}(1)$$

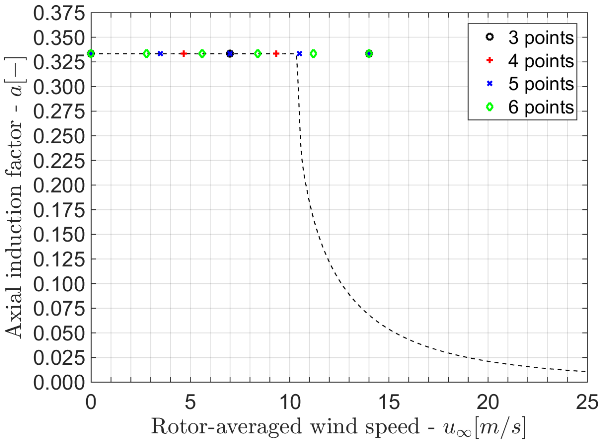

Figure 5.12: Alternatives for initial Bézier control points axial induction factor curves.

The energy-loss fraction of the unoptimized wind farm is based on $N_{\mathrm{wt}} = 3$ wind turbines operating at the Betz limit. Optimization runs are performed for three, four, five and six control points, with the initial values displayed in Figure 5.12[4].

The pattern search algorithm of the current case uses a mesh tolerance of $\epsilon = 10^{-4}$ and the GPSPositiveBasisNp1 search strategy is used, for which a complete poll is applied. Four different optimization runs are performed for the current case. The performance of the runs is assessed upon objective function value decrement and optimization time. The optimum number of control points is used for the remaining performance curve optimization problems.

### 5.2.6. Case B4: Analysis of free-stream wind turbine performance curves

**Purpose** The purpose of Case B4 is to obtain insight into the influence of the free-stream wind turbine performance curves on the energy production of a complete row.

**Wind farm layout and wind directions** The current case uses the same wind turbine row, wind speeds and wind direction as Case B1, B2 and B3. The layout is displayed in Figure 5.9 and the wind speeds and wind direction can be found in Section 5.2.3.

**Optimization parameters** The wind turbine performance curves are parametrized by the Bézier control points method[3]. Only the performance curves of the first wind turbine are optimized, in the current case. The second and third wind turbine keep operating at Betz conditions. In line with Case B1 and B2, the maximum optimization wind speed is chosen to be $V_{\mathrm{opt,max}} = 14\mathrm{m/s}$. Optimization runs are performed for three, four and five control points, meaning that 4, 6 and 8 optimization parameters are used ($2N_{\mathrm{B}} - 2$).

**Optimization problem formulation** The power constraint is satisfied by keeping the optimization parameters bounded between $a = 0$ and the Betz axial induction factor curve. The points on the Bézier curve beyond the crossing with the Betz curve are replaced by the values of the Betz curve.

The maximum allowed axial induction factor value of a control point is $a = \frac{1}{2}$ and the rotor-averaged wind speed of the control points is bounded between $u_\infty = 0$ and $u_\infty = V_{\mathrm{opt,max}} = 14\mathrm{m/s}$. Additional constraints are that the control points should remain in the same horizontal order as initially specified. Based on the statements above, the optimization problem of Case B4 is defined by Equation (5.12). The formulation is the same as the formulation of Case B3, but now only the performance curve of the first wind turbine is optimized.

---

[4] The control points are uniformly distributed over the $0 \leq u_\infty \leq V_{\mathrm{opt,max}}$ range and all have the values $a = a_{\mathrm{Betz}} = \frac{1}{3}$.

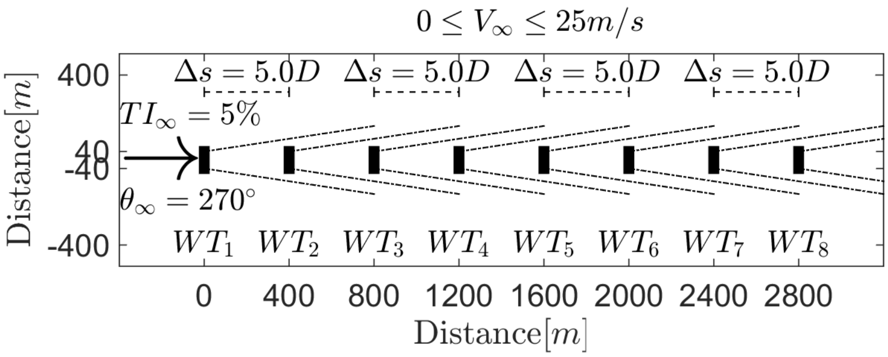

Figure 5.13: Top view of performance curve optimization Case B5, with eight wind turbines.

$$\min_{CP_{j=1:N_B}} \quad \xi_{\text{AEP,farm}} \tag{5.12}$$

subject to

$$\begin{bmatrix}0 & 0\end{bmatrix} \leq CP_j \leq \begin{bmatrix}14 & \frac{1}{2}\end{bmatrix}$$

$$CP_j(1) < CP_{j+1}(1)$$

The energy-loss fraction of the unoptimized wind farm is based on $N_{\text{wt}} = 3$ wind turbines operating at the Betz limit. Optimization runs are performed for three, four and five control points, with the initial values displayed in Figure 5.12[4].

The pattern search algorithm of the current case uses a mesh tolerance of $\epsilon = 10^{-4}$ and the GPSPositiveBasisNp1 search strategy is used, for which a complete poll is applied. Three different optimization runs are performed for the current case. The performance of the runs is assessed upon objective function value decrement and optimization time.

### 5.2.7. Case B5: Influence of the number of wind turbines

**Purpose** The purpose of Case B5 is to obtain insight into the influence of the number of wind turbines in a row, on the optimum performance curves and the average energy-loss fraction.

**Wind farm layout, wind speeds and wind direction** The current case involves optimization of a wind turbine row with $N_{\text{wt}} = 8$ wind turbines, as shown in Figure 5.13. The wind speeds and wind direction are similar to Case B1, B2, B3 and B4 and can be found in Section 5.2.3.

**Optimization parameters** The wind turbine performance curves are parametrized by the Bézier control points method[3]. The same performance curves are assigned to all wind turbines. Before defining the optimization problem, simulations were performed for all integer wind speeds in the $V_{\text{in}} < V_\infty \leq V_{\text{out}}$ range with unoptimized Betz wind turbines[5]. The simulations with the Betz wind turbines showed that the maximum optimization wind speed should also in the current case be set to $V_{\text{opt,max}} = 14\text{m/s}$. Optimization runs are performed for three and four control points, meaning that 4 and 6 optimization parameters are used.

**Optimization problem formulation** The power constraint is satisfied by keeping the optimization parameters bounded between $a = 0$ and the Betz axial induction factor curve. The points on the Bézier curve beyond the crossing with the Betz curve are replaced by the values of the Betz curve.

The maximum allowed axial induction factor value of a control point is $a = \frac{1}{2}$ and the rotor-averaged wind speed of the control points is bounded between $u_\infty = 0$ and $u_\infty = V_{\text{opt,max}} = 14\text{m/s}$. Additional constraints are that the control points should remain in the same horizontal order as initially specified. Based on the statements above, the optimization problem of Case B5 is defined by Equation (5.13).

---

[5] The FarmFlow-fast performance curves for running the simulations are shown in Figure 5.1

The formulation is the same as the formulation of Case B3, but now the number of wind turbines is increased from three to eight.

$$
\begin{aligned}
&\min_{CP_{\mathrm{j=1:N_B}}} \quad \xi_{\mathrm{AEP,farm}} \\
&\text{subject to} \\
&\qquad \begin{bmatrix} 0 & 0 \end{bmatrix} \leq CP_{\mathrm{j}} \leq \begin{bmatrix} 14 & \tfrac{1}{2} \end{bmatrix} \\
&\qquad CP_{\mathrm{j}}(1) < CP_{\mathrm{j+1}}(1)
\end{aligned}
\tag{5.13}
$$

The energy-loss fraction of the unoptimized wind farm is based on $N_{\mathrm{wt}} = 8$ wind turbines operating at the Betz limit. Optimization runs are performed for three and four control points, with the initial values displayed in Figure 5.12[4].

The pattern search algorithm of the current case uses a mesh tolerance of $\epsilon = 10^{-4}$ and the GPSPositiveBasisNp1 search strategy is used, for which a complete poll is applied. Two different optimization runs are performed for the current case. The performance of the runs is assessed upon objective function value decrement and optimization time.

### 5.2.8. Case B6: Wind farm optimization by taking the complete wind rose into account

**Purpose** The purpose of Case B6 is to obtain insight into the potential of wind turbine performance curve optimization when a complete wind rose and wind farm are concerned.

**Wind farm layout, wind speeds and wind directions** The current case involves the performance curve optimization of a square wind farm consisting of $N_{\mathrm{wt}} = 16$ wind turbines. The layout of the wind farm is displayed at the left side of Figure 5.14. The minimum distance between the wind turbines is $\Delta s = 5.0D$.

The performance curves are again optimized for the $V_{\mathrm{in}} \leq u_{\infty} \leq V_{\mathrm{out}}$ range and the complete wind rose is taken into account; $V_{\mathrm{in}} \leq V_{\infty} \leq V_{\mathrm{out}}$ and $0 \leq \theta_{\infty} \leq 2\pi$. The Weibull wind speed distribution is the same as for the previous performance curve optimization cases and the wind rose is uniformly distributed. Due to the symmetrical wind farm layout and wind climate, simulations can be reused when analysing the wind farm. Running simulations with the Betz wind turbines for $\theta_{\infty} = (0:1:45)^{\circ}$ and calculating the energy-loss fraction per wind direction, yields the graph at the right side of Figure 5.14.

From the energy-loss fractions of Figure 5.14, the complete $0 \leq \theta_{\infty} \leq 2\pi$ range can be covered by mirroring the energy-loss fractions per wind direction over the symmetry axes of the wind farm. After mirroring, the average energy-loss fraction of the wind farm is by Equations (5.2), (5.3) and (5.7) calculated to be $\xi_{\mathrm{AEP_{tot}}} = 7.51\%$.

Due to limited computing resources, it is not possible to simulate all wind directions in the $\theta_{\infty} = (0:1:45)^{\circ}$ range during every function evaluation of the optimization run. A compromise is achieved by simulating only for the five wind directions $\boldsymbol{\theta}_{\infty} = \begin{bmatrix} 8 & 17 & 26 & 35 & 44 \end{bmatrix}^{\circ}$. The average energy-loss fraction of these wind directions is calculated to be $\overline{\xi}_{\mathrm{AEP}_{\boldsymbol{\theta}_{\infty}}} = 7.46\%$. The average energy-loss fractions of the complete wind rose and the concerned wind directions are displayed in the right graph of Figure 5.14, by respectively the black and red dashed lines. It is assumed that the five wind directions are representative for the complete wind rose.

The left graph of Figure 5.14 shows the simulated wind directions as solid arrows and the dashed arrows with the same colours represent the symmetrically similar mirrored wind directions.

**Optimization parameters** The wind turbine performance curves are parametrized by the Bézier control points method[3]. The same performance curves are assigned to all wind turbines. From the runs with the unoptimized Betz wind turbines[6], it turned out that the maximum optimization wind speed in current case should be set to $V_{\mathrm{opt,max}} = 13\mathrm{m/s}$. An optimization run is performed with three control points, meaning that four optimization parameters are used.

---

[6] The FarmFlow-fast performance curves for running the simulations are shown in Figure 5.1

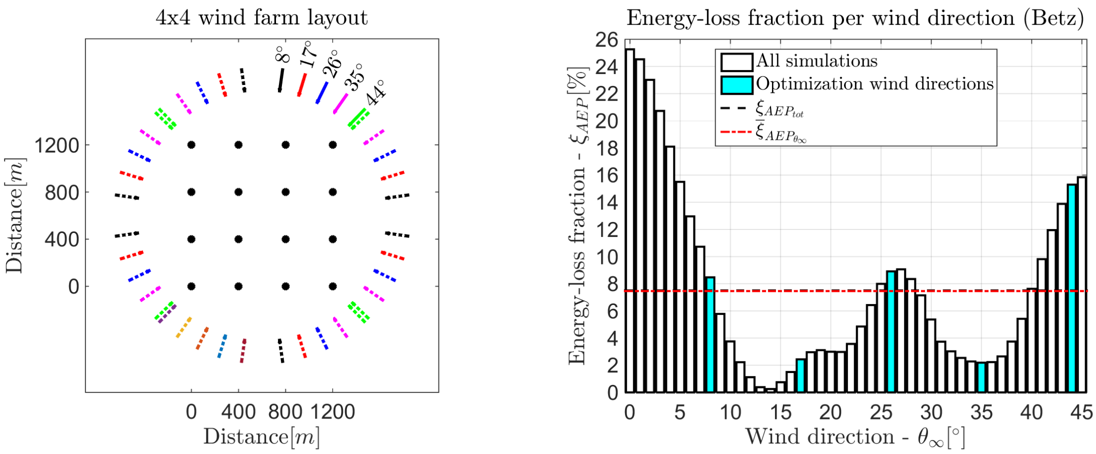

Figure 5.14: Explanation of performance curve optimization Case B6. Left: top view of the 4x4 wind farm layout, with the concerned wind directions and their symmetrically similar mirrored wind directions. Right: energy-loss fractions per wind direction with Betz wind turbines; the cyan bars represent the wind directions that are used for the optimization runs, the dashed lines are the average energy-loss fractions of the complete wind rose(black) and optimization wind directions(red).

**Optimization problem formulation** The power constraint is satisfied by keeping the optimization parameters bounded between $a = 0$ and the Betz axial induction factor curve. The points on the Bézier curve beyond the crossing with the Betz curve are replaced by the values of the Betz curve.

The maximum allowed axial induction factor value of a control point is $a = \frac{1}{2}$ and the rotor-averaged wind speed of the control points is bounded between $u_\infty = 0$ and $u_\infty = V_{\text{opt,max}} = 13\text{m/s}$. Additional constraints are that the control points should remain in the same horizontal order as initially specified. Based on the statements above, the optimization problem of Case B6 is defined by Equation (5.14).

$$\begin{aligned} &\min_{CP_{\text{j=1:N}_\text{B}}} \quad \xi_{\text{AEP,farm}} \\ &\text{subject to} \\ &\quad \begin{bmatrix} 0 & 0 \end{bmatrix} \leq CP_{\text{j}} \leq \begin{bmatrix} 13 & \frac{1}{2} \end{bmatrix} \\ &\quad CP_{\text{j}}(1) \leq CP_{\text{j+1}}(1) \end{aligned} \tag{5.14}$$

The energy-loss fraction of the unoptimized wind farm is based on $N_{\text{wt}} = 16$ wind turbines operating at the Betz limit. One optimization run is performed using three control points, with the initial values displayed in Figure 5.12[4]. The pattern search algorithm of the current case uses a mesh tolerance of $\epsilon = 10^{-4}$ and the GPSPositiveBasisNp1 search strategy is used, for which a complete poll is applied. One optimization run is performed for the current case, which is assessed upon objective function value decrement.

# 6

# Results of the optimization problems

This chapter presents the results of all optimization cases described in Section 5.2. It starts with the axial induction factor optimization problem in Section 6.1. Hereafter, it continues with the performance curve optimization cases in Section 6.2.

## 6.1. Axial induction factor optimization

**Case A1: Optimization algorithm analysis** The graphical results of axial induction factor optimization Case A1 are displayed in Figures 6.1 and 6.2. The numerical results are displayed in Table C.1 of Appendix C.

At the left side of Figure 6.1, the surface plot of the design space exploration is shown. The vertical axis displays the total power generation of the three wind turbines together and the other two axes represent the axial induction factor values of the first two wind turbines; $a_1$ and $a_2$. From the graph, the location of the global optimum can roughly be estimated. The solution surface has a wavy character, which might has been caused by numerical noise. The wavy surface can be problematic for gradient based algorithms like *fmincon*, because such algorithms treat the minima of the waves as local optima.

The graph at the right side of Figure 6.1 shows the 2D contour plot of the design space exploration. From the contour plot, it becomes clear that the optimum parameter values are located in the vicinity of $a_{1,\mathrm{opt,robust}} = 0.23$ and $a_{2,\mathrm{opt,robust}} = 0.34$ and that $P_{\mathrm{tot,opt}} > 3175\mathrm{kW}$.

Figure 6.2 compares the performance of the investigated optimization algorithms with each other. For the top graphs, $a_{1,\mathrm{init}} = a_{2,\mathrm{init}} = \frac{1}{3}$ is used as initial optimization parameter values. The middle graphs used $a_{1,\mathrm{init}} = a_{2,\mathrm{init}} = \frac{53}{600}$ and the bottom graphs used $a_{1,\mathrm{init}} = a_{2,\mathrm{init}} = \frac{1}{300}$.

The left graphs show bar charts of the optimum power generation per wind turbine. The first bar represents the power generation while operating at Betz conditions. The total power generation of the three Betz wind turbines is $P_{\mathrm{tot,Betz}} = 3056\mathrm{kW}$. It is shown that the first wind turbine generates more than half of the total power. The other bars represent the optima found by the optimization algorithms.

In the top left graph, the total power generation is increased for all algorithms. The power generation of the first wind turbine is decreased, resulting in an increased power generation of the second and third wind turbine. The total power generation lies between $P_{\mathrm{tot,fmincon}} = 3164\mathrm{kW}$ for the *fmincon* algorithm and $P_{tot,opt} = 3188kW$ of the *fminsearch*, pattern search and the genetic algorithm. The simulated annealing algorithm and the design space exploration (Robust) have found intermediate total power generation values, with respectively $P_{\mathrm{tot,SA}} = 3186\mathrm{kW}$ and $P_{\mathrm{tot,robust}} = 3187\mathrm{kW}$.

The relative total power generation increase fraction between the found optima and the Betz conditions is calculated by Equation (6.1).

$$I_{\mathrm{P}} = \frac{P_{\mathrm{tot,opt}} - P_{\mathrm{tot,Betz}}}{P_{\mathrm{tot,Betz}}} \tag{6.1}$$

The relative power generation increase fractions lie in the range $3.52 \leq I_{\mathrm{P}} \leq 4.31\%$, for the different optimization methods when starting from $a_{1,\mathrm{init}} = a_{2,\mathrm{init}} = \frac{1}{3}$. The average power-loss fraction of the three wind turbines is reduced from $\xi_{\mathrm{P,Betz}} = 43.90\%$ to $41.49 \leq \xi_{\mathrm{P,opt}} \leq 41.93\%$, depending on the algorithm.

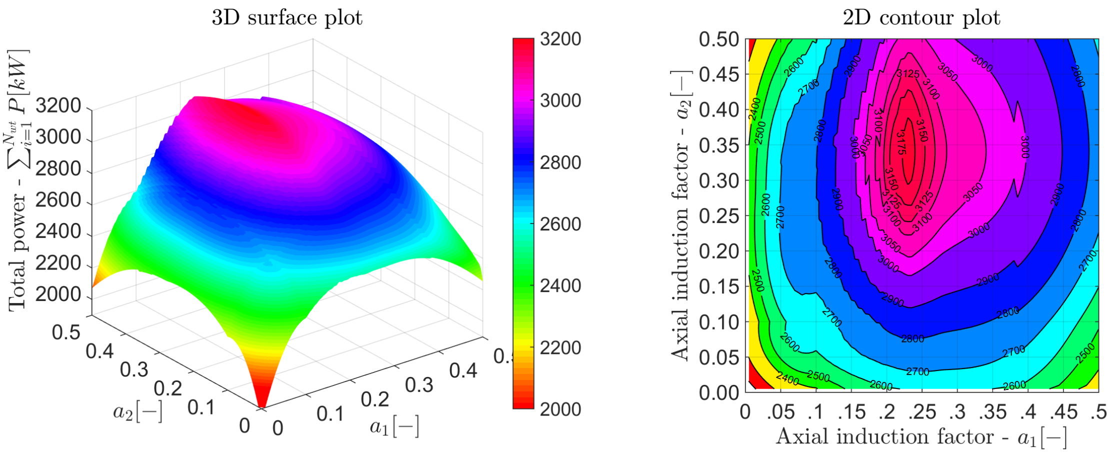

Figure 6.1: Plots of the total power generation of three wind turbines, as function of the axial induction factors of the first two wind turbines. Left: 3D surface plot, right: 2D contour plot.

The right graphs of Figure 6.2 show the locations of the optimum axial induction factors and the initial axial induction factors, on a 2D contour plot. From the top right graph it can be concluded that the *fminsearch*, pattern search and genetic algorithm converge to the global optimum, but the *fmincon* and simulated annealing algorithms find an optimum point at an offset from the global optimum.

The middle graphs of Figure 6.2 present the same information as the top graphs, but now for the initial axial induction factor values $a_{1,\text{init}} = a_{2,\text{init}} = \frac{53}{600}$. The most notable difference with the top graphs is that the *fminsearch* and *fmincon* algorithms both converge to a local optimum at $a_{1,\text{opt}} < 0.1$ and $a_{2,\text{opt}} < 0.1$, which results in more than $13.5\%$ power reduction compared to the Betz wind turbines. The other algorithms behave similar as in the top graphs. The behaviour of the algorithms in the bottom graphs corresponds to the behaviour in the top graphs of Figure 6.2, although the *fmincon* algorithm performs better in this case.

The *fminsearch* and *fmincon* algorithms took on average $t_{\text{opt}} \approx 5\text{min}$, before the optimization run was terminated. The pattern search algorithm took $t_{\text{opt,PS}} \approx 8\text{min}$ and the simulated annealing and genetic algorithm took respectively $t_{\text{opt,SA}} \approx 2\text{hrs}$ and $t_{\text{opt,GA}} \approx 3.5\text{hrs}$. The design space exploration took $t_{\text{opt,robust}} \approx 5.5\text{hrs}$. It has to be noted that the optimization times were found for standard optimization algorithm settings and that single core processing was used. Changing algorithm settings and using parallel processing might change the proportions.

From the axial induction factor optimization results, it can be concluded that there is a potential for wind turbine performance curve optimization. The total power generation of this 'worst-case scenario' can be increased with more than $4\%$. The average power increase will however be lower when more wind directions and wind speeds above rated wind speed are included. It is observed that the difference between the optimum axial induction factor value and the Betz axial induction factor is larger for the free-stream wind turbine than for the second wind turbine.

The global optimization algorithms, i.e. pattern search, simulated annealing and the genetic algorithm, showed better global convergence characteristics than the local optimization algorithms, i.e. *fminsearch* and *fmincon*. The optimization times of the simulated annealing and the genetic algorithms are however considered as being too long. As the optimization time scales strongly with the number of optimization parameters, it is concluded that the last two mentioned algorithms are not suitable for performance curve optimization due to limited availability of computational resources.

Keeping the statements of the above paragraph in mind, it is concluded that pattern search is the most suitable algorithm for performance curve optimization. It should however be noted that the performance curve optimization cases in the current project are more complex than the axial induction factor optimization problem, especially when Bézier control points parametrization is used. As a result of the difference in complexity, a good performance with the axial induction factor optimization problem does not guarantee that the global optimum will be found in the performance curve optimization cases.

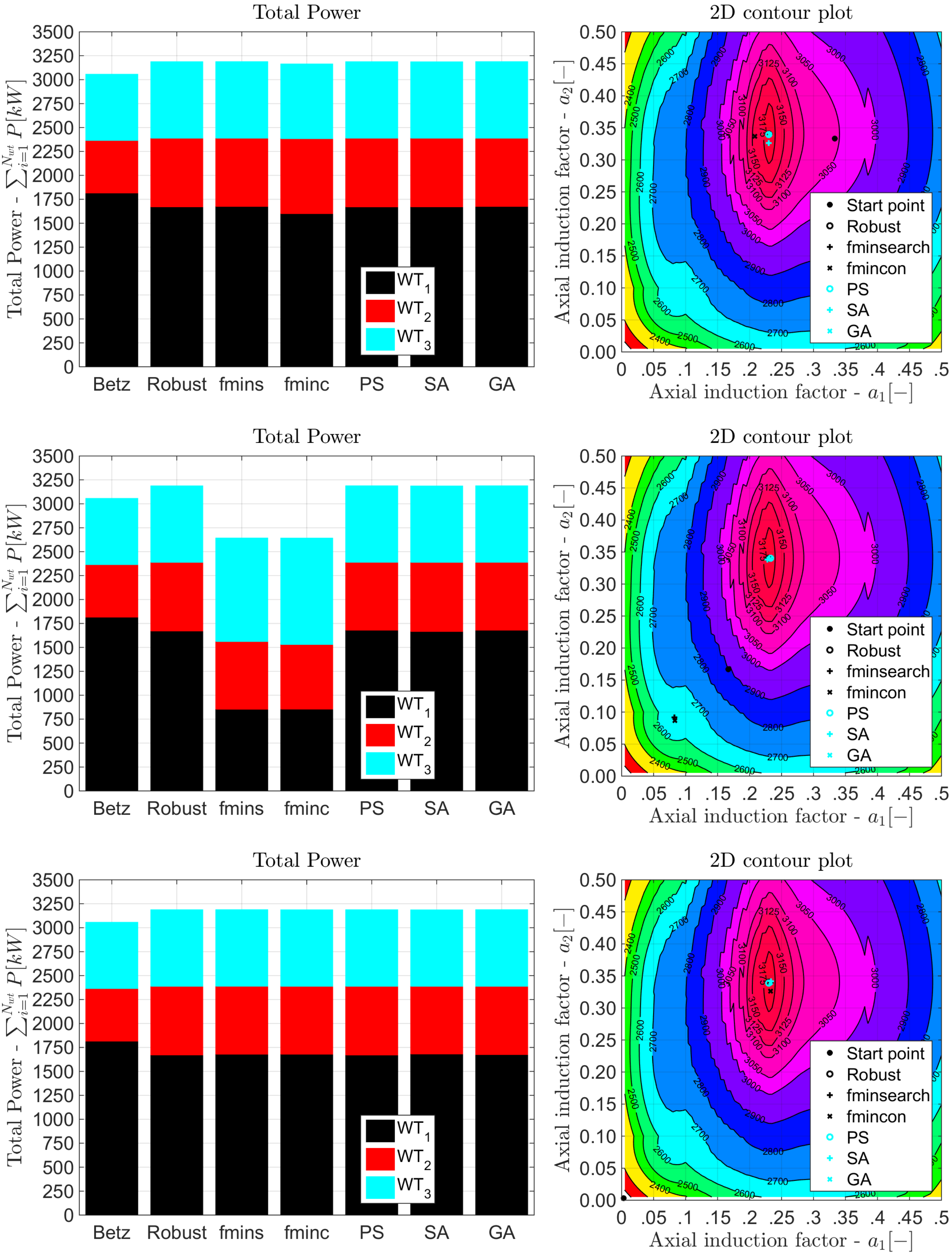

Figure 6.2: Comparison between the optima found by the optimization algorithms, for different starting points; left: bar charts of the power generation of the optimum wind turbines, right: location of the optimum parameter values in a 2D contour plot. Top: $a_{1,\text{init}} = a_{2,\text{init}} = \frac{1}{3}$, middle: $a_{1,\text{init}} = a_{2,\text{init}} = \frac{53}{600}$, bottom: $a_{1,\text{init}} = a_{2,\text{init}} = \frac{1}{300}$.

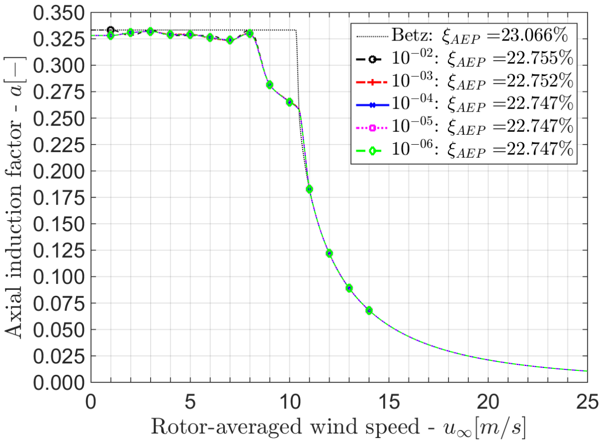

Figure 6.3: Case B1: Comparison between the optima with different termination criteria.

## 6.2. Performance curve optimization

This section presents the results of the six performance curve optimization cases. All cases have used parallel processing in order to reduce the computation time of the optimization runs.

**Case B1: Convergence tolerance sensitivity analysis** Figure 6.3 shows the graphical results of performance curve optimization Case B1. The numerical results can be found in Table D.1 of Appendix D.

Figure 6.3 compares the optimum axial induction factor curves, found by the pattern search algorithm when using different termination criteria. The optimum curves and the Betz curve are displayed together with their associated energy-loss fractions. Since the focus of the current case is on convergence, more decimals are displayed than the number of significant digits.

In line with the theory presented in Section 2.2, the axial induction factor values are further reduced in the area just below rated wind speed than for lower wind speeds. The rated wind speed has moved right towards a higher velocity. The above described observations imply that loads on the wind turbine rotors in the vicinity of the rated wind speed are reduced, because the thrust coefficient is lowered in this area.

The relative annual energy production increase fraction, between Betz performance curves and the optimum performance curves, is calculated by Equation (6.2).

$$I_{\text{AEP}} = \frac{AEP_{\text{tot,opt}} - AEP_{\text{tot,Betz}}}{AEP_{\text{tot,Betz}}} \tag{6.2}$$

As can be seen from the Figure 6.3, the energy-loss fraction is reduced from $\xi_{\text{AEP,Betz}} \approx 23.07\%$ to $\xi_{\text{AEP,opt}} \approx 22.75\%$. This corresponds to an AEP increase of $I_{\text{AEP}} \approx 0.4\%$. As explained in Section 6.1, the relative increase in AEP is smaller than the relative power generation increase found by the axial induction optimization problem. It is observed that the AEP of the first wind turbine is reduced, yielding an increase in AEP of the second and third wind turbine.

The optimum axial induction factor curves found by using different mesh tolerances have a similar shape. The shape of the optimum curves is too complex to be transformed into exact design parameters. A rotor design based upon a smoothed version of the presented optimum curves can never be such optimized as the theoretical curves displayed in Figure 6.3.

From Figure 6.3, only the curve obtained with $\epsilon = 10^{-2}$ seems to deviate from the other optimum curves. By analysing the numerical results however, it is concluded that a mesh tolerance of $\epsilon \leq 10^{-4}$ has to be used to obtain a three decimal convergence. It is assumed that a three decimal convergence is acceptable for the optimization problems of the current project.

The optimization runs took between two and 31 hours for respectively $\epsilon = 10^{-2}$ and $\epsilon = 10^{-6}$. The optimization run with $\epsilon = 10^{-4}$ took almost eight hours, which is assumed to be the most suitable combination of optimization time and order of convergence. For the remaining optimization cases, a mesh tolerance of $\epsilon = 10^{-4}$ is therefore used.

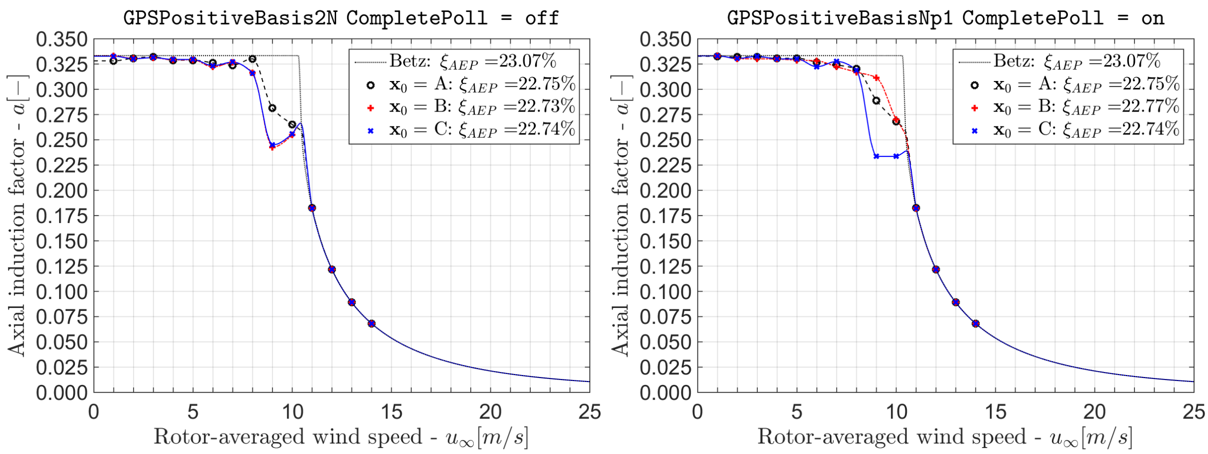

Figure 6.4: Case B2: Comparison between the optima found by the pattern search algorithm using different search strategies.

**Case B2: Search strategy analysis** Figure 6.4 shows the graphical results of performance curve optimization Case B2. The numerical results can be found in Table D.2 of Appendix D.

Figure 6.4 compares the optimum axial induction factor curves with each other, which were found by the pattern search algorithm by using different search strategies and initial conditions. Again, the optimum curves and the Betz curve are displayed together with their associated energy-loss fractions. The behaviour of the optimization runs roughly corresponds to the runs of Case B1. The shape of the curves are again too complex to be exactly transformed into a wind turbine rotor design. The only way to obtain such complex operational curves is by changing the pitch angle of the rotor blades, for which a complicated wind turbine controller would be required. All optimum curves increase the energy production with $I_{\text{AEP}} \approx 0.4\%$, but the optimization parameters do not converge to the same values.

By comparing the search methods, it can be concluded that the GPSPositiveBasis2N strategy without making complete polls yields (on average) lower objective function values than the GPSPositiveBasisNp1 method making complete polls. It can however not be stated whether the method is performing better or that both methods incidentally end up into better or worse local optima.

A remarkable observation is the 'kink' in the optimum curves, when started from initial curve C (displayed in Figure 5.11). As the optimum energy-loss fraction is lower for both search strategies, when starting from curve C than when started from curve A, it is assumed that all optimization runs have ended up in local optima. The optimization runs took on average approximately 10 hours, where the GPSPositiveBasisNp1 making complete polls performed quicker with initial curves A and B, while the GPSPositiveBasis2N method without making complete polls was quicker when starting from curve C.

As the GPSPositiveBasisNp1 method making complete polls was not clearly outperformed by the GPSPositiveBasis2N method without making complete polls and the strategy provides more flexibility in search directions, it is assumed that the GPSPositiveBasisNp1 method making complete polls is the best search strategy for optimization problems using Bézier control points parametrization. The higher search direction flexibility might be beneficial, because the constraints potentially prohibit a number of search directions when using Bézier control points parametrization. For the remaining optimization cases, the GPSPositiveBasisNp1 method making complete polls is therefore used.

**Case B3: Bézier control points analysis** Figure 6.5 shows the graphical results of performance curve optimization Case B3. The numerical results can be found in Table D.3 of Appendix D.

Figure 6.5 compares the optimum axial induction factor curves with each other, which were found by the pattern search algorithm by using a varying number of Bézier control points. The optimum curves and the Betz curve are displayed together with their associated energy-loss fractions. Again it is observed that the axial induction factor values are further reduced in the area just below rated wind speed than for lower wind speeds and that the rated wind speed has moved right.

The optimum curves are smoother than the curves found by the discrete parametrization method. The curves are therefore easier to be transformed into design parameters. The objective function value

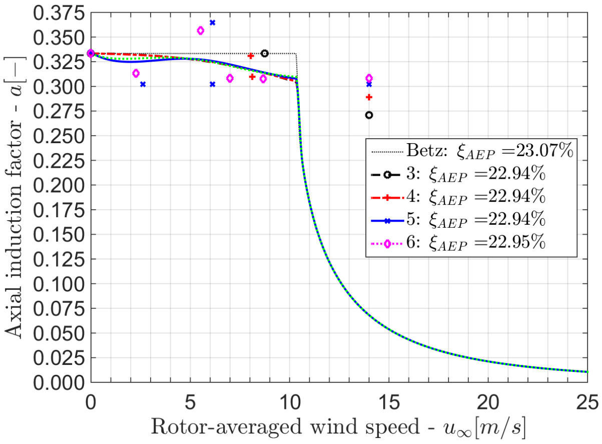

Figure 6.5: Case B3: Comparison between the optima found by using a different number of control points.

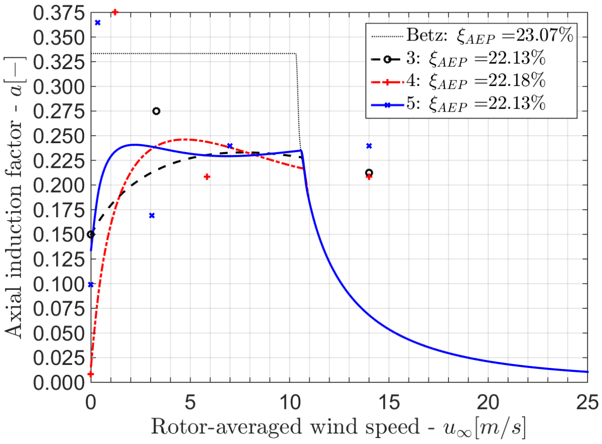

Figure 6.6: Case B4: Comparison between the optima found by using a different number of control points.

reduction is however less pronounced; the increase in AEP now lies in the range $0.15 \leq I_{\text{AEP}} \leq 0.17\%$. The optimization times of the runs using Bézier control points parametrization are substantially shorter than for the discrete points parametrization. The run that used three control points took $t_{\text{opt}} = 19\text{min}$, with four and five control points it took somewhat more than half an hour and it took almost two hours with six control points.

The optimum curves with a different number of control points show similar behaviour, although the curve with five control points shows a remarkable trough in the curve around $u_\infty = 2\text{m/s}$. The remainder of the optimum curves follow the same shape, which can easily be represented by a Bézier curve with three or four control points. The optimum curve that used six control points resulted into a higher objective function value than the curves that used less parameters.

It is assumed that the resulting axial induction factor curves are local optima and it is therefore hard to determine how many control points are required to represent the optimum curve. As using six control points takes substantially longer than using three, four or five points, it is concluded that using more than five points does not provide any improvement. The next scenario is therefore performed with three, four and five control points, to get a better impression on the required number of control points. It is opted to continue with Bézier control points parametrization due to the quicker optimization runs and the smoother optimum performance curves.

**Case B4: Analysis of free-stream wind turbine performance curves** Figure 6.6 shows the graphical results of performance curve optimization Case B4. In this case, only the performance curves of the first wind turbine are manipulated as explained in Section 5.2.6. The numerical results can be found in Table D.4 of Appendix D.

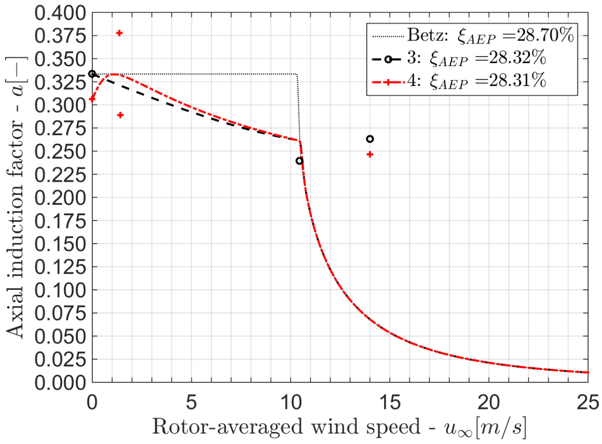

Figure 6.7: Case B5: Comparison between the optima found by using a different number of control points.

Figure 6.6 compares the optimum axial induction factor curves with each other, which were found by the pattern search algorithm by using a varying number of Bézier control points. The optimum curves and the Betz curve are displayed together with their associated energy-loss fractions. It is observed that the behaviour of the optimum curves is different from the optimum curves in the previous cases. The optimum curves differ more from the Betz curves and the gain in AEP is higher than in the previous performance curve optimization cases.

The optimum curves found by the different number of control points differ clearly from each other. It is assumed that local optima are found again. A remarkable observation is that the axial induction factor is further reduced close to the cut-in wind speed than around rated wind speed. The increase in AEP lies between $I_{\text{AEP}} = 1.15\%$ for using four control points and $I_{\text{AEP}} = 1.22\%$ when using three or five control points. It seems that the curve with four control points can not escape from a local optimum.

The optimization runs took between $t_{\text{opt}} = 37\text{min}$ when using three control points and $t_{\text{opt}} = 61\text{min}$ when using five control points. The runs took somewhat longer than the runs in Case B3, which originates from the fact that the optimum curves lie further away from the initial curve than in Case B3. It can still not be clearly stated how many control points are required for representing the optimum curve, although three points should be sufficient to represent the curves displayed in Figure 6.6. As the next case involves longer simulations due to the increasing number of wind turbines, Case B5 only uses three and four control points to save computation time.

It is concluded that the performance curves of the free-stream wind turbine are most important in the performance curve optimization problem. Only changing the performance curves of the free-stream wind turbine and keeping the other wind turbines at Betz conditions yields more additional AEP than using the strategy of Case B3. The aforementioned statements indicate that there is a potential for considering different rotors for the first wind turbine row of a wind farm than the rotors of the other wind turbines.

**Case B5: Influence of the number of wind turbines** Figure 6.7 shows the graphical results of performance curve optimization Case B5. In this case, a row of eight wind turbines is analysed as explained in Section 5.2.7. The numerical results can be found in Table D.5 of Appendix D.

Figure 6.7 compares the optimum axial induction factor curves with each other, which were found by the pattern search algorithm by using a varying number of Bézier control points. The optimum curves and the Betz curve are displayed together with their associated energy-loss fractions. It is observed that the energy-loss fractions are higher than for the cases with three wind turbines and the energy gain between the optimum curves and the Betz curve is bigger.

The optimum curves show the same behaviour as Cases B1, B2 and B3; with lower axial induction factors around rated wind speed than around cut-in wind speed. The optimum curves found with three and four control points are almost identical, although a remarkable 'kink' is observed for the curve with four points. The relative increase in AEP is $I_{\text{AEP}} = 0.53\%$ for three control points and $I_{\text{AEP}} = 0.54\%$ for four control points, which is a higher gain than with three wind turbines. The optimization time with three control points was $t_{\text{opt}} = 117\text{min}$ and $t_{\text{opt}} = 227\text{min}$ with four control points.

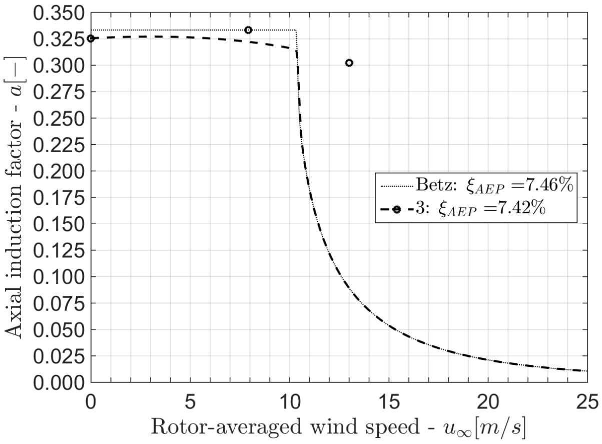

Figure 6.8: Case B6: Optimum axial induction curve for the 4x4 wind farm.

As the difference between both optimum curves is small, the curves can easily be represented by three control points and the optimization time with three control points is about twice as short as for four control points, it is decided to use only three control points for Case B6. The optimization time becomes important for Case B6, because the number of wind turbines as well as the number of wind directions increases.

**Case B6: Wind farm optimization by taking the complete wind rose into account** Figure 6.8 shows the graphical results of performance curve optimization Case B6. In this case, a square wind farm with 16 wind turbines is analysed as explained in Section 5.2.8. The numerical results can be found in Table D.6 of Appendix D.

Figure 6.8 shows the optimum axial induction factor curve, found by the pattern search algorithm by using three Bézier control points. The optimum curve and the Betz curve are displayed together with their associated energy-loss fraction. It is observed that the energy-loss fraction is lower in this case than for the previous cases, which is in line with the consulted literature during the project. The difference between the optimum curve and the Betz curve is smaller than in the previous cases, although the behaviour of the optimum curve is similar as the optimum curves in Case B1, B2, B3 and B5.

The AEP of the complete wind farm is increased with $I_{\text{AEP}} = 0.046\%$, which is a substantially smaller increase than in the previous cases. The energy-loss fraction is reduced from $\xi_{\text{AEP,Betz}} = 7.46\%$ to $\xi_{\text{AEP,opt}} = 7.42\%$ and the optimization run took $t_{\text{opt}} = 430\text{min}$.

A remarkable observation is that the 'inner' four wind turbines (type C in Table D.6) produce more energy than the wind turbines at the sides of the wind farm (type A are the corner wind turbines and type B are the remaining eight wind turbines). It is unclear whether this observation is realistic or not, it might however be that the results are incorrect due to not accounting for wind direction variation. It is expected that this phenomena will not be observed when using a wind farm with more wind turbines. The only wind turbines that produce more energy with the optimum curves than with the Betz curves are the B-type wind turbines.

# 7

# Conclusions and recommendations

This chapter provides conclusions drawn from the current project and recommendations for further research. It starts with the conclusions in Section 7.1, providing the main conclusions drawn from the FarmFlow-fast validation study and the investigated optimization problems. Afterwards, Section 7.2 provides the recommendations for further research based upon the findings of the current project.

## 7.1. Conclusions

This section provides the conclusions drawn from the current project. It starts with the conclusions related to the first research objective in Section 7.1.1, involving the validation of FarmFlow-fast. Hereafter, the conclusions related to the second research objective are given in Section 7.1.2, involving the wind turbine performance curve optimization.

### 7.1.1. Validation of the FarmFlow-fast software

From the FarmFlow-fast validation study, it is observed that FarmFlow-fast simulations show a close agreement with both simulations of the original FarmFlow version and power generation measurement data. The difference between FarmFlow-fast simulations and the measurement data gets bigger as simulation scenarios get more specific; averaging numerous simulations over large wind direction and wind speed ranges however, averages out the simulation errors. It is concluded that FarmFlow-fast provides acceptable results for the investigated validation cases. FarmFlow-fast is capable to be used for optimization purposes involving wind farm-wake calculations.

FarmFlow-fast does not show a worse agreement with measurement data than the original FarmFlow version. Results were alternately under and over estimated by both software versions. Simulations of the Horns Rev wind farm seemed to show a better agreement with measurement data than simulations performed in the Lillgrund wind farm. It is however hard to compare the quality of simulation results amongst two different wind farms, because the quality and amount of available measurement data as well as the concerned wind speed/direction combinations are never completely similar.

FarmFlow-fast was approximately 19 times quicker than the original FarmFlow version, for the investigated validation cases. Simulating a wind farm with 80 wind turbines, for 72 wind direction sectors and 22 different wind speeds, will however still take about 24 hours on an average desktop pc. Such computational requirements may be considered too long, especially when multiple assessments need to be carried out.

It can not be concluded whether the turbulence intensity, wind turbine spacing or wind speed range is of any influence on the quality of the FarmFlow-fast simulation data. Comparison of additional validation cases is required before firm conclusions can be drawn about the influence of the aforementioned parameters. With the current validation data, it was demonstrated that the usage of FarmFlow-fast is a valid choice for parameter ranges close to the investigated scenarios.

The power generation data of the FarmFlow-fast validation study was averaged over a number of wind directions and wind speeds. If the averaged simulation and measurement data show a good agreement with each other, it does not imply that the tool is performing equally well for smaller wind direction sectors and wind speed ranges. Especially when small wind direction sectors are taken into account, the validity of the simulations can not always be guaranteed.

The quality of both FarmFlow-fast and the original FarmFlow version is worse for wind directions generating a wake that narrowly passes downstream wind turbines. Wind turbines close to the edge of the wake experience higher rotor-averaged wind speeds and generate more power than the upstream wind turbine. This phenomenon is not observed in reality, due to unsteady aerodynamic processes in the wind causing wind direction changes and wind speed variations. The wind direction changes and wind speed variations cause the actual average wind speed experienced by the wind turbines in the wake to be lower than the wind speed calculated by FarmFlow-fast.

### 7.1.2. Optimization of wind turbine performance curves

From the investigated optimization problems, it can be concluded that there is a potential for increasing the annual energy production of a wind farm by wind turbine performance curve optimization. The most suitable algorithm for the optimization problems was the pattern search algorithm. The pattern search algorithm was most suitable due to its favourable combination of objective function value decrement and optimization time and its global convergence characteristics, during the optimization runs.

It was concluded that the termination criterion of the pattern search algorithm could best be set less sharp than the default settings. Relaxing the termination criterion led to shorter optimization runs, without compromising the reduction in objective function value. The most suitable termination criterion was chosen due to its favourable combination of objective function value decrement and optimization time. The default methodology by which the pattern search algorithm searches through the design space was also changed, because the currently used method provides more flexibility in search directions than the default method.

Using Bézier curves to parametrize the wind turbine performance curves proved to be almost 20 times quicker than using discrete axial induction factor specification points. Additionally, the optimum curves found with Bézier control points parametrization are smoother, which may be easier to transform into rotor design parameters than volatile performance curves. The annual energy production increase is however smaller with Bézier control points parametrization. Besides the lower energy production increase, Bézier curve parametrization turned out to not always be an ideal combination with the pattern search algorithm. The use of this combination turned out to be prone to end up in local optima during the performance curve optimization cases.

The extent to which wind turbine performance curve optimization can increase the annual energy production of a wind farm depends on the accounted wind speed and direction ranges, the wind farm layout and the used optimization strategy. It turned out that the most substantial power generation increase was established when:

- A single wind speed/direction combination is concerned.
- The free-stream wind speed is just below the rated wind speed of the wind turbines.
- The wind direction is aligned with a row of wind turbines
- The wind turbines are individually optimized

Increasing the number of wind speeds and directions and using similar performance curves for all wind turbines, reduced the potential benefit of wind turbine performance curve optimization. The increase in annual energy production of a square wind farm with 16 wind turbines, taking the complete wind rose into account, was almost negligible when the same optimized performance curves were assigned to all wind turbines.

It was found that increasing the number of wind turbines in a wind farm results into higher energy losses due to wake effects. The relative gain in annual energy production after optimization was however higher and the wind turbine performance curves optimized for wind farm operation move further away from Betz conditions.

The contribution of the free-stream wind turbine performance curves to the total energy-loss fraction of a wind farm proved to be substantial. It turned out that it is more beneficial to only manipulate the performance curves of the free-stream wind turbines, than to use the same performance curves for all wind turbines. This implies that there is a potential for considering different rotors for the first wind turbine row of a wind farm than the rotors of the other wind turbines.

Although the potential increase in annual energy production can be considered rather small, the thrust reduction on the wind turbine rotors around rated wind speed can as well be an important outcome of the optimization runs. The thrust reduction can result in cheaper wind turbine designs, which may even be a more promising result in terms of costs of energy reduction than the increase in annual energy production.

The above mentioned thrust reduction is currently widely applied in practice and is formally known as 'peak shaving'. In the optimization problems of the current project, the unoptimized wind turbines were assumed to operate at the Betz limit. The potential annual energy production increase of a wind farm, by applying wind turbine performance curve optimization to real wind turbines, will be lower than the margins that were found from the optimization problems in the current project.

The optimization cases have used scenarios in which wake effects were exaggeratedly well represented. The wake effects were such severe due to the chosen wind farm layout, wind climate and the accounted wind directions. On the other hand, the optimization cases were all based on a small number of wind turbines. Increasing the number of wind turbines will generally increase the energy losses of a wind farm.

## 7.2. Recommendations for further research

The assumption of using a wind direction standard deviation of $\sigma_\theta = 2.5^\circ$ might be reconsidered for analysing wind turbine wakes with FarmFlow-fast. It may even be worth considering to implement a model in FarmFlow-fast that implicitly includes wind direction variation in its calculations.

The influence of the ambient turbulence intensity, wind turbine spacing and the wind speed range on the quality of FarmFlow-fast simulation results can not be judged based on the FarmFlow-fast validation study. More validation cases have to be investigated for getting a better impression of the above mentioned influences. Investigation of more validation cases however requires additional measurement data.

The thrust reduction on the wind turbine rotors can be an interesting research topic to further investigate. Another optimization strategy to further investigate can be to use different performance curves for all wind turbines, which proved to result into a higher annual energy production gain than using the same curves for all wind turbines. Such a strategy however involves more optimization parameters and requires more computational resources. In order to compensate for the additional computational demands from the increasing number of optimization parameters, a less sophisticated wind farm-wake model or optimization algorithm may be envisaged.

It might be worthwhile to investigate different optimization scenarios and to validate the current runs with the original FarmFlow version or another wind farm-wake model, to get a better impression of the wind turbine performance curve optimization potential. The above described investigations might also lead to new insights concerning the combination of Bézier curve parametrization with the pattern search algorithm. Wind farms with more wind turbines may be investigated and it can be useful to make sure whether the wind direction variation is of any influence on the results of the investigated optimization scenarios.

# Bibliography

[1] J. Moccia, J. Wilkes, I. Pineda, and G. Corbetta, *Wind energy scenarios for 2020*, Tech. Rep. (European Wind Energy Association, 2014).

[2] A. Kusiak and Z. Song, *Design of wind farm layout for maximum wind energy capture,* Renewable Energy **35**, 685 (2010).

[3] A. Emami and P. Noghreh, *New approach on optimization in placement of wind turbines within wind farm by genetic algorithms,* Renewable Energy **35**, 1559 (2010), special Section: {IST} National Conference 2009.

[4] J. Marden, S. Ruben, L. Pao, R. Gopalakrishnan, J. Marden, A. Wierman, J. Marden, H. P. Young, L. Pao, N. Li, *et al.*, *Surveying game theoretic approaches for wind farm optimization,* in *Proceedings of the 50th IEEE Conference on Decision and Control*, Vol. 38 (2012) pp. 584–596.

[5] B. Sanderse, *Aerodynamics of wind turbine wakes: Literature review*, Tech. Rep. (ECN, 2009).

[6] G. Corten and P. Schaak, *Heat and flux,* Patent Number WO2004111446 (2003).

[7] K. E. Johnson and N. Thomas, *Wind farm control: Addressing the aerodynamic interaction among wind turbines,* in *American Control Conference, 2009. ACC'09.* (IEEE, 2009) pp. 2104–2109.

[8] P. M. O. Gebraad and J. W. van Wingerden, *Maximum power-point tracking control for wind farms,* Wind Energy , n/a (2014).

[9] J. Olauson and M. Bergkvist, *Modelling the swedish wind power production using {MERRA} reanalysis data,* Renewable Energy **76**, 717 (2015).

[10] R. J. Barthelmie, K. Hansen, S. T. Frandsen, O. Rathmann, J. Schepers, W. Schlez, J. Phillips, K. Rados, A. Zervos, E. Politis, *et al.*, *Modelling and measuring flow and wind turbine wakes in large wind farms offshore,* Wind Energy **12**, 431 (2009).

[11] K. S. Hansen, R. J. Barthelmie, L. E. Jensen, and A. Sommer, *The impact of turbulence intensity and atmospheric stability on power deficits due to wind turbine wakes at horns rev wind farm,* Wind Energy **15**, 183 (2012).

[12] J.-S. Guillemette and L. Woodward, *Maximizing wind farm energy production in presence of aerodynamic interactions,* International Conference of Control, Dynamic Systems, and Robotics (2014).

[13] *Improvements in ECN Wake Model*, ECN (Presented at: ICOWES2013 Conference, Lyngby, 17-19 June 2013, 2013).

[14] F. van Dam, P. Gebraad, and J.-W. van Wingerden, *A maximum power point tracking approach for wind farm control,* Proceedings of The Science of Making Torque from Wind (2012).

[15] F. González-Longatt, P. Wall, and V. Terzija, *Wake effect in wind farm performance: Steady-state and dynamic behavior,* Renewable Energy **39**, 329 (2012).

[16] R. J. Barthelmie, G. C. Larsen, S. T. Frandsen, L. Folkerts, K. Rados, S. C. Pryor, B. Lange, and J. Schepers, *Comparison of wake model simulations with offshore wind turbine wake profiles measured by sodar,* Journal of Atmospheric and Oceanic Technology **23**, 888 (2006).

[17] B. Lange, H.-P. Waldl, A. G. Guerrero, D. Heinemann, and R. J. Barthelmie, *Modelling of offshore wind turbine wakes with the wind farm program flap,* Wind Energy **6**, 87 (2003).

[18] M. Gaumond, P. Réthoré, A. Bechmann, S. Ott, G. Larsen, A. Peña, and K. Hansen, *Benchmarking of wind turbine wake models in large offshore wind farms,* in *Proceedings of the Science of Making Torque from Wind Conference* (2012).

[19] R. J. Barthelmie, S. T. Frandsen, O. Rathmann, K. S. Hansen, E. Politis, J. Prospathopoulos, J. Schepers, K. Rados, D. Cabezón, W. Schlez, *et al.*, *Flow and wakes in large wind farms: final report for upwind wp8* (Danmarks Tekniske Universitet, Risø Nationallaboratoriet for Bæredygtig Energi, 2011).

[20] J. G. Schepers, *Engineering models in wind energy aerodynamics: Development, implementation and analysis using dedicated aerodynamic measurements* (TU Delft, Delft University of Technology, 2012).

[21] P. Torres, J.-W. van Wingerden, and M. Verhaegen, *Modeling of the flow in wind farms for total power optimization,* in *Control and Automation (ICCA), 2011 9th IEEE International Conference on* (IEEE, 2011) pp. 963–968.

[22] J. Annoni, P. Seiler, K. Johnson, P. Fleming, and P. Gebraad, *Evaluating wake models for wind farm control,* in *American Control Conference (ACC), 2014* (IEEE, 2014) pp. 2517–2523.

[23] N. O. Jensen, *A note on wind generator interaction* (Risø National Laboratory, 1983).

[24] I. Katic, J. Højstrup, and N. Jensen, *A simple model for cluster efficiency,* in *European Wind Energy Association Conference and Exhibition* (1986) pp. 407–410.

[25] N. G. Mortensen, L. Landberg, I. Troen, and E. Lundtang Petersen, *Wind atlas analysis and application program (wasp),* Risø National Laboratory (1993).

[26] P. A. Fleming, P. M. Gebraad, S. Lee, J.-W. van Wingerden, K. Johnson, M. Churchfield, J. Michalakes, P. Spalart, and P. Moriarty, *Evaluating techniques for redirecting turbine wakes using sowfa,* Renewable Energy (2014).

[27] O. Ltd, *Openfoam,* (2014).

[28] L. A. Martínez-Tossas, M. J. Churchfield, and S. Leonardi, *Large eddy simulations of the flow past wind turbines: actuator line and disk modeling,* Wind Energy (2014).

[29] A. AB10, *A comparison of wake model performances in an offshore environment,* ENDOW project (2001).

[30] G. WindFarmer, *Wind farm design software: Theory manual,* (2010).

[31] K. Rados, G. Larsen, R. Barthelmie, W. Schlez, B. Lange, G. Schepers, T. Hegberg, and M. Magnisson, *Comparison of wake models with data for offshore windfarms,* Wind Engineering **25**, 271 (2001).

[32] B. Lange, H. peter Waldl, R. Barthelmie, A. G. Guerrero, and D. Heinemann, *Improvement of the wind farm model flap for offshore applications,* (2002).

[33] P. E. J. Vermeulen, *An experimental analysis of wind turbine wakes,* in *3rd International Symposium on Wind Energy Systems*, edited by H. G. Reimerdes (1980) pp. 431–450.

[34] K. S. Hansen, *Benchmarking of lillgrund offshore wind farm scale wake models in the eera-dtoc project,* in *EERA DeepWind'2014 Conference 22 – 24 January 2014* (EERA, 2014).

[35] G. C. Larsen, *A simple stationary semi-analytical wake model,* (2009).

[36] S. Ott, *Linearised CFD models for wakes* (Danmarks Tekniske Universitet, Risø Nationallaboratoriet for Bæredygtig Energi, 2011).

[37] S. Lang and E. McKeogh, *Lidar and sodar measurements of wind speed and direction in upland terrain for wind energy purposes,* Remote Sensing **3**, 1871 (2011).

[38] D. J. Renkema, *Validation of wind turbine wake models,* Master of Science Thesis, Delft University of Technology (2007).

[39] A. Hertz, O. Marcotte, A. Mdimagh, M. Carreau, and F. Welt, *Wind farm design optimization,* (2013).

[40] J. C. Mora, J. M. C. Barón, J. M. R. Santos, and M. B. Payán, *An evolutive algorithm for wind farm optimal design,* Neurocomputing **70**, 2651 (2007), neural Network Applications in Electrical Engineering, Selected papers from the 3rd International Work-Conference on Artificial Neural Networks (IWANN 2005).

[41] A. Svetlana, S. Jussi, K. Saku, P. Jarmo, and P. Olli, *Optimization of wind farm design taking into account uncertainty in input parameters,* in *Proceedings of Annual Conference of European Wind Energy Association (EWEA)* (2013).

[42] R. Storn and K. Price, *Differential evolution–a simple and efficient heuristic for global optimization over continuous spaces,* Journal of global optimization **11**, 341 (1997).

[43] J. R. Marden, S. Ruben, and L. Pao, *A model-free approach to wind farm control using game theoretic methods,* IEEE Transactions on Control Systems Technology (2013).

[44] P. M. Gebraad, F. C. van Dam, and J.-W. van Wingerden, *A model-free distributed approach for wind plant control,* in *American Control Conference (ACC), 2013* (IEEE, 2013) pp. 628–633.

[45] *A maximum power point tracking approach for wind farm control*, Delft, University of Technology (Presented at the 2012 'The Science of Making Torque from Wind' conference in Oldenburg, Germany, 2013).

[46] K. E. Johnson and G. Fritsch, *Assessment of extremum seeking control for wind farm energy production,* Wind Engineering **36**, 701 (2012).

[47] E. T. G. Bot, *FarmFlow validation against four full scale wind farms*, Tech. Rep. (ECN, 2012).

[48] A. Crespo, F. Manuel, D. Moreno, E. Fraga, and J. Hernández, *Numerical analysis of wind turbine wakes,* in *Proceeding of the Delphy Workshop on Wind Energy Applications* (IEEE, 1985) pp. 15–25.

[49] A. Crespo and J. Hernández, *Numerical modelling of the flow field in a wind turbine wake,* in *Proceedings of the 3rd Joint ASCE/ASME Mechanics Conference, Forum on Turbulent Flows* (AMSE, 1989) pp. 628–633.

[50] B. Mohammadi and O. Pironneau, *Analysis of the k-epsilon turbulence model* (Wiley New York, 1993).

[51] Y. Jun and T.-Z. Mai, *{ADI} method – domain decomposition,* Applied Numerical Mathematics **56**, 1092 (2006).

[52] L. Caretto, A. Gosman, S. Patankar, and D. Spalding, *Two calculation procedures for steady, three-dimensional flows with recirculation,* in *Proceedings of the Third International Conference on Numerical Methods in Fluid Mechanics*, Lecture Notes in Physics, Vol. 19, edited by H. Cabannes and R. Temam (Springer Berlin Heidelberg, 1973) pp. 60–68.

[53] H. Panofsky and J. Dutton, *Atmospheric turbulence - Models and methods for engineering applications* (Wiley, 1984).

[54] T. Burton, D. Sharpe, N. Jenkins, and E. Bossanyi, *Aerodynamics of horizontal-axis wind turbines,* in *Wind Energy Handbook* (John Wiley & Sons, Ltd, 2011) pp. 39–120.

[55] W. Z. Shen, R. Mikkelsen, J. N. Sørensen, and C. Bak, *Tip loss corrections for wind turbine computations,* Wind Energy **8**, 457 (2005).

[56] A. Van Garrel, *Development of a wind turbine aerodynamics simulation module* (Citeseer, 2003).

[57] G. Schepers, A. van Garrel, E. Wiggelinkhuizen, J. Pierik, and E. Bot, *How aerodynamic and electrical aspects come together in wind farm design,* in *EERA DeepWind'2014 Conference 22 – 24 January 2014* (EERA, 2014).

[58] R. Koole, *Validation of FarmFlow wind farm-wake aerodynamic models in large offshore wind farms*, Tech. Rep. (ECN, 2014).

[59] Vestas, *V80-2.0 mw,* Brochure (2009).

[60] F. Fritsch and R. Carlson, *Monotone piecewise cubic interpolation,* SIAM Journal on Numerical Analysis **17**, 238 (1980), http://dx.doi.org/10.1137/0717021 .

[61] Siemens, *Siemens wind turbine swt-2.3-93,* Brochure (2009).

[62] H. Bergström, *Meteorological conditions at lillgrund,* Swedish Energy Agency , 1 (2009).

[63] *Wasp website,* `http://www.wasp.dk/` (2015), accessed: 2015-01-24.

[64] J. A. Dahlberg, *Assessment of the lillgrund wind farm: Power performance wake effects,* Vattenfall Vindkraft AB, 6_1 LG Pilot Report, http://www. vattenfall. se/sv/-file/15_Assessment_of_the_Lillgrund_W. pdf_16596737. pdf (cited March 30, 2012) (2009).

[65] M. Gaumond, P.-E. Réthoré, S. Ott, A. Peña, A. Bechmann, and K. S. Hansen, *Evaluation of the wind direction uncertainty and its impact on wake modeling at the horns rev offshore wind farm,* Wind Energy **17**, 1169 (2014).

[66] A. Clerc, M. Anderson, P. Stuart, and G. Habenicht, *A systematic method for quantifying wind flow modelling uncertainty in wind resource assessment,* Journal of Wind Engineering and Industrial Aerodynamics **111**, 85 (2012).

[67] J. F. Manwell, J. G. McGowan, and A. L. Rogers, *Aerodynamics of wind turbines,* in *Wind Energy Explained : Theory, Design and Application* (Wiley, 2010) pp. 91–155.

[68] G. Farin, *Class a bézier curves,* Computer Aided Geometric Design **23**, 573 (2006).

[69] Q.-b. Wu and F.-h. Xia, *Shape modification of bézier curves by constrained optimization,* Journal of Zhejiang University Science **6**, 124 (2005).

[70] Matlab, *Global Optimization Toolbox User's guide*, The MathWorks Inc, Natick Massachusetts, U.S.A (2015), version R2015a.

[71] J. C. Lagarias, J. A. Reeds, M. H. Wright, and P. E. Wright, *Convergence properties of the nelder–mead simplex method in low dimensions,* SIAM Journal on optimization **9**, 112 (1998).

[72] Matlab, *Optimization Toolbox User's guide*, The MathWorks Inc, Natick Massachusetts, U.S.A (2015), version R2015a.

[73] R. H. Byrd, J. C. Gilbert, and J. Nocedal, *A trust region method based on interior point techniques for nonlinear programming,* Mathematical Programming **89**, 149 (2000).

[74] R. H. Byrd, M. E. Hribar, and J. Nocedal, *An interior point algorithm for large-scale nonlinear programming,* SIAM Journal on Optimization **9**, 877 (1999), http://dx.doi.org/10.1137/S1052623497325107 .

[75] R. A. Waltz, J. L. Morales, J. Nocedal, and D. Orban, *An interior algorithm for nonlinear optimization that combines line search and trust region steps,* Mathematical Programming **107**, 391 (2006).

[76] L. Ingber *et al.*, *Adaptive simulated annealing (asa): Lessons learned,* Control and cybernetics **25**, 33 (1996).

[77] K. Deep, K. P. Singh, M. Kansal, and C. Mohan, *A real coded genetic algorithm for solving integer and mixed integer optimization problems,* Applied Mathematics and Computation **212**, 505 (2009).

[78] K. Deb, *An efficient constraint handling method for genetic algorithms,* Computer Methods in Applied Mechanics and Engineering **186**, 311 (2000).

[79] R. Fletcher and M. J. Powell, *On the modification of $ldl^t$ factorizations,* Mathematics of Computation **28**, 1067 (1974).

# A

# Numerical results of the FarmFlow-fast validation cases

Table A.1: Results of the A-cases of the FarmFlow-fast validation study.

| Case | [%] | | | | | | | | | | | | | | | | | | [−] | |
|---|---|---|---|---|---|---|---|---|---|---|---|---|---|---|---|---|---|---|---|---|
| | $\bar{\xi}_{\mathrm{P}_2}$ | | $\bar{\xi}_{\mathrm{P}_3}$ | | $\bar{\xi}_{\mathrm{P}_4}$ | | $\bar{\xi}_{\mathrm{P}_5}$ | | $\bar{\xi}_{\mathrm{P}_6}$ | | $\bar{\xi}_{\mathrm{P}_7}$ | | $\bar{\xi}_{\mathrm{P}_8}$ | | $\bar{\xi}_{\mathrm{P}_9}$ | | $\bar{\xi}_{\mathrm{P}_{10}}$ | | $\lvert\Delta\bar{\xi}_{\mathrm{P}_{\mathrm{SM,max}}}\rvert$ | $\lvert\Delta\bar{\xi}_{\mathrm{P}_{\mathrm{FN,max}}}\rvert$ |
| | **M** | **S** | **M** | **S** | **M** | **S** | **M** | **S** | **M** | **S** | **M** | **S** | **M** | **S** | **M** | **S** | **M** | **S** | | |
| HR A1 | 20.4 | 19.1 | 20.9 | 18.6 | 24.4 | 21.8 | 28.5 | 27.2 | 31.1 | 31.6 | 34.0 | 34.3 | 36.8 | 36.3 | 38.9 | 37.6 | 41.0 | 38.5 | $2.6 \cdot 10^{-2}$ | $8.6 \cdot 10^{-3}$ |
| HR A2 | 12.6 | 14.9 | 19.8 | 22.2 | 25.8 | 28.7 | 29.9 | 33.5 | 33.6 | 36.8 | 36.1 | 39.0 | | | | | | | $3.6 \cdot 10^{-2}$ | $9.9 \cdot 10^{-3}$ |
| HR A3 | 16.8 | 14.7 | 21.7 | 20.4 | 27.2 | 27.4 | 33.2 | 32.6 | 36.6 | 36.1 | 40.0 | 38.6 | | | | | | | $2.1 \cdot 10^{-2}$ | $1.6 \cdot 10^{-2}$ |
| LG A1 | 36.4 | 41.4 | 40.8 | 38.1 | 54.3 | 53.2 | 60.5 | 57.3 | 62.9 | 60.0 | 64.4 | 61.7 | 65.8 | 65.1 | | | | | $5.0 \cdot 10^{-2}$ | $2.6 \cdot 10^{-2}$ |

Table A.2: Results of the B-cases of the FarmFlow-fast validation study.

| Case | [%] | | [−] | |
|---|---|---|---|---|
| | $\xi_{\mathrm{P}_{2,\mathrm{max}}}$ | | $\lvert\Delta\xi_{\mathrm{P}_{\mathrm{SM,max}}}\rvert$ | $\lvert\Delta\xi_{\mathrm{P}_{\mathrm{FN,max}}}\rvert$ |
| | **M** | **S** | | |
| HR B1 | 41.2 | 42.0 | $3.7 \cdot 10^{-2}$ | $8.6 \cdot 10^{-3}$ |
| LG B1 | 70.6 | 71.8 | $6.3 \cdot 10^{-2}$ | $3.2 \cdot 10^{-2}$ |
| LG B2 | 81.6 | 77.5 | $5.9 \cdot 10^{-2}$ | $6.6 \cdot 10^{-3}$ |

# B

# Matlab optimization toolbox.

Matlab's Optimization Toolbox provides functions for finding parameters that minimize or maximize objectives while satisfying constraints. The toolbox includes solvers for linear programming, mixed-integer linear programming, quadratic programming, non-linear optimization and non-linear least squares. The solvers can be used to find optimal solutions to continuous and discrete problems, perform trade-off analyses and incorporate optimization methods into algorithms and applications.

A brief description of the optimization algorithms of Matlab's optimization toolbox is given in Appendices B.1 to B.5. Most information is obtained from the user guides of the 'Matlab Optimization Toolbox'[72] and 'Matlab Global Optimization Toolbox'[70]. For detailed information, the reader is referred to the user guides.

## B.1. fminsearch

*fminsearch* is an unconstrained, non-linear optimization algorithm that uses the 'Nelder-Mead simplex' algorithm as described in [71]. Unconstrained minimization is the problem of finding a vector $\mathbf{x}$ that is a local minimum to a scalar function $f(\mathbf{x})$: $\min_{\mathbf{x}} f(\mathbf{x})$. The term "unconstrained" means that no restriction is placed on the range of $\mathbf{x}$. The *fminsearch* algorithm uses a simplex of $n+1$ points, for $n$-dimensional $\mathbf{x}$ vectors.

The algorithm first makes a simplex around the initial guess $\mathbf{x}_0$, by adding $5\%$ of each component $\mathbf{x}_0(j)$, to $\mathbf{x}_0$ and using the $n$ vectors as elements of the simplex in addition to $\mathbf{x}_0$[1]. Hereafter, the algorithm modifies the simplex repeatedly according to the below described procedure[2].

1. Let $\mathbf{x}(j)$ denote the list of points, in the current simplex, $j = 1, ..., n+1$.
2. Order the points in the simplex, from lowest function value, $f(\mathbf{x}(1))$, to highest function value, $f(\mathbf{x}(n+1))$. At each step in the iteration, the algorithm discards the current worst point $\mathbf{x}(n+1)$ and accepts another point into the simplex. (Or in the case of step 7 below, it changes all $n$ points with values above $f(\mathbf{x}(1))$).
3. Generate the reflected point
   $\mathbf{r} = 2\mathbf{m} - \mathbf{x}(n+1)$,

   where $\mathbf{m} = \sum_{j=1}^{n} \frac{\mathbf{x}(j)}{n}$,

   and calculate $f(\mathbf{r})$.
4. If $f(\mathbf{x}(1)) \leq f(\mathbf{r}) < f(\mathbf{x}(n))$, accept $\mathbf{r}$ and terminate this iteration. **Reflect**
5. If $f(\mathbf{r}) < f(\mathbf{x}(1))$, calculate the expansion point $\mathbf{z}$
   $\mathbf{z} = \mathbf{m} + 2(\mathbf{m} - \mathbf{x}(n+1))$,

---

[1] If $\mathrm{x}_0(j) = 0$ it uses $0.00025$ as component of $j$.

[2] The keywords for the *fminsearch* iterative display appear in bold after the description of the step.

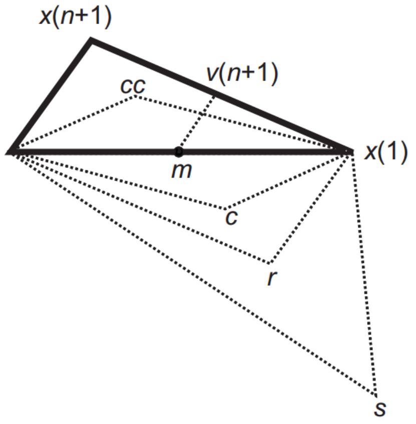

Figure B.1: Nelder-Mead Simplex algorithm evaluation procedure ($n = 2$)[72].

and calculate $f(\mathbf{z})$.

(a) If $f(\mathbf{z}) < f(\mathbf{r})$, accept $\mathbf{z}$ and terminate the iteration. **Expand**

(b) Otherwise, accept $\mathbf{r}$ and terminate the iteration. **Reflect**

6. If $f(\mathbf{r}) \geq f(\mathbf{x}(n))$, perform a contraction between $\mathbf{m}$ and the better of $\mathbf{x}(n+1)$ and $\mathbf{r}$:
   (a) If $f(\mathbf{r}) < f(\mathbf{x}(n+1))$ (i.e., $\mathbf{r}$ is better than $\mathbf{x}(n+1)$), calculate
   $\mathbf{c} = \mathbf{m} + \frac{\mathbf{r}-\mathbf{m}}{2}$,

   and calculate $f(\mathbf{c})$.

      i. If $f(\mathbf{c}) < f(\mathbf{r})$, accept $\mathbf{c}$ and terminate the iteration. **Contract outside**
      ii. Otherwise, continue with Step 7 (Shrink).

   (b) If $f(\mathbf{r}) \geq f(\mathbf{x}(n+1))$, calculate
   $\mathbf{cc} = \mathbf{m} + \frac{\mathbf{x}(n+1)-\mathbf{m}}{2}$

   and calculate $f(\mathbf{cc})$.

      i. If $f(\mathbf{cc}) < f(\mathbf{x}(n+1))$, accept $\mathbf{cc}$ and terminate the iteration. **Contract inside**
      ii. Otherwise, continue with Step 7 (Shrink).

7. Calculate the $n$ points
   $\mathbf{v}(j) = \mathbf{x}(1) + \frac{\mathbf{x}(j)-\mathbf{x}(1)}{2}$

   and calculate $f(\mathbf{v}(j))$; $j = 2, ..., n+1$.

   The simplex at the next iteration is $\mathbf{x}(1), \mathbf{v}(2), ..., \mathbf{v}(n+1)$. **Shrink**

Figure B.1 shows the points that *fminsearch* might calculate in the procedure, along with each possible new simplex. The original simplex has a bold outline. The iterations proceed until they meet a stopping criterion.

## B.2. fmincon

Constrained minimization is the problem of finding a vector $\mathbf{x}$ that is a local minimum to a scalar function $f(\mathbf{x})$ subject to constraints on the allowable $\mathbf{x}$; $\min_{\mathbf{x}} f(\mathbf{x})$, such that one or more of the following holds:

- $\mathbf{c}_{neq}(\mathbf{x}) \leq \mathbf{0}$

- $\mathbf{c}_{eq}(\mathbf{x}) = \mathbf{0}$
- $\mathbf{A}_{neq}\mathbf{x} \leq \mathbf{b}_{neq}$
- $\mathbf{A}_{eq}\mathbf{x} = \mathbf{b}_{eq}$
- $\mathbf{l} \leq \mathbf{x} \leq \mathbf{u}$

**Barrier function** The interior-point approach to constrained minimization is to solve a sequence of approximate minimization problems. The original problem is given by Equation (B.1).

$$\begin{aligned} &\min_{\mathbf{x}} f(\mathbf{x}) \\ &\text{subject to} \\ &\quad \mathbf{h}(\mathbf{x}) = \mathbf{0} \\ &\quad \mathbf{g}(\mathbf{x}) \leq \mathbf{0} \end{aligned} \tag{B.1}$$

For each $\mu > 0$, the approximate problem is given by Equation (B.2).

$$\begin{aligned} &\min_{\mathbf{x},\mathbf{s}} f(\mathbf{x}) - \mu \sum_i \ln(s_i) \\ &\text{subject to} \\ &\quad \mathbf{h}(\mathbf{x}) = \mathbf{0} \\ &\quad \mathbf{g}(\mathbf{x}) + \mathbf{s} = \mathbf{0} \end{aligned} \tag{B.2}$$

There are as many slack variables $s_j$ as there are inequality constraints $\mathbf{g}$. The $s_j$ are restricted to be positive to keep $\ln(s_j)$ bounded. As $\mu$ decreases to zero, the minimum of $f(\mathbf{x}) - \mu \sum_j \ln(s_j)$ should approach the minimum of $f$. The added logarithmic term is called a "barrier function". This method is described in [73–75].

The approximate problem in Equation (B.2) is a sequence of equality constrained problems. The equality constraint problems are easier to solve than the original inequality constrained problem in Equation (B.1). To solve the approximate problem, the algorithm uses one of two main types of steps at each iteration:

- A direct step in $(\mathbf{x}, \mathbf{s})$. This step attempts to solve the Karush-Kuhn-Tucker (KKT) Equations (B.3) and (B.4), for the approximate problem via a linear approximation. The KKT equations use the auxiliary Lagrangian function in Equation (B.5). The direct step is also called a "Newton step".
- A Conjugate Gradient (CG) step, using a trust region.

$$\nabla_{\mathbf{x}} \mathcal{L}(\mathbf{x}, \boldsymbol{\lambda}) = 0 \tag{B.3}$$

$$\lambda_{g,j} g_j(\mathbf{x}) = 0 \ \forall\ j \tag{B.4}$$

$$\mathcal{L}(\mathbf{x}, \boldsymbol{\lambda}) = f(\mathbf{x}) + \sum \lambda_{g,j} g_j(\mathbf{x}) + \sum \lambda_{h,j} h_j(\mathbf{x}) \tag{B.5}$$

By default, the algorithm first attempts to take a direct step. If it cannot, it attempts a CG step. One case where it does not take a direct step is when the approximate problem is not locally convex near the current iterate. At each iteration, the algorithm decreases a "merit function" such as in Equation (B.6).

$$f(\mathbf{x}) - \mu \sum_j \ln(s_j) + \nu ||\mathbf{h}(\mathbf{x}), \mathbf{g}(\mathbf{x}) + \mathbf{s}|| \tag{B.6}$$

The parameter $\nu$ may increase with iteration number in order to force the solution towards feasibility. If an attempted step does not decrease the merit function, the algorithm rejects the attempted step and attempts a new step.

**Direct step** The following variables are used in defining the direct step:

- $\mathbf{H}$ denotes the Hessian of the Lagrangian of $f(\mathbf{x}) - \mu \sum_j \ln(s_j)$:
  $\mathbf{H} = \nabla^2 f(\mathbf{x}) + \sum_j \lambda_j \nabla^2 g_j(\mathbf{x}) + \sum_l \lambda_l \nabla^2 h_l(\mathbf{x})$.
- $\mathbf{J_g}$ denotes the Jacobian of the constraint function $\mathbf{g}$.
- $\mathbf{J_h}$ denotes the Jacobian of the constraint function $\mathbf{h}$.
- $\mathbf{S} = diag(\mathbf{s})$.
- $\boldsymbol{\lambda}$ denotes the Lagrange multiplier vector associated with constraints $\mathbf{g}$.
- $\boldsymbol{\Lambda} = diag(\boldsymbol{\lambda})$.
- $\mathbf{y}$ denotes the Lagrange multiplier vector associated with $\mathbf{h}$.
- $\mathbf{e}$ denotes the vector of ones with the same size as $\mathbf{g}$.

Equation (B.7) defines the direct step $(\Delta\mathbf{x}, \Delta\mathbf{s})$.

$$\begin{bmatrix} \mathbf{H} & 0 & \mathbf{J_h}^T & \mathbf{J_g}^T \\ 0 & \mathbf{S}\boldsymbol{\Lambda} & 0 & -\mathbf{S} \\ \mathbf{J_h} & 0 & \mathbf{I} & 0 \\ \mathbf{J_g} & -\mathbf{S} & 0 & \mathbf{I} \end{bmatrix} \begin{bmatrix} \Delta\mathbf{x} \\ \Delta\mathbf{s} \\ -\Delta\mathbf{y} \\ -\Delta\boldsymbol{\lambda} \end{bmatrix} = - \begin{bmatrix} \nabla f - \mathbf{J_h}^T\mathbf{y} - \mathbf{J_g}^T\boldsymbol{\lambda} \\ \mathbf{S}\boldsymbol{\lambda} - \mu\mathbf{e} \\ \mathbf{h} \\ \mathbf{g} + \mathbf{s} \end{bmatrix} \tag{B.7}$$

Equation (B.7) comes directly from attempting to solve Equations (B.3) and (B.4), using a linearized Lagrangian. In order to solve Equation (B.7) for $(\Delta\mathbf{x}, \Delta\mathbf{s})$, the algorithm makes an LDL factorization[79] of the matrix. This is the most computationally expensive step. One result of the factorization is the determination whether the projected Hessian is positive definite or not. If the projected Hessian is not positive definite, the algorithm uses a CG step as described in the next paragraph.

**Conjugate gradient step** The CG approach to solving the approximate problem in Equation (B.2) is similar to other CG calculations. In this case, the algorithm adjusts both $\mathbf{x}$ and $\mathbf{s}$, keeping the slacks $\mathbf{s}$ positive. The approach is to minimize a quadratic approximation to the approximate problem in a trust region, subject to linearized constraints.

Specifically, let $R$ denote the radius of the trust region and let other variables be defined as in the 'Direct step' paragraph. The algorithm obtains Lagrange multipliers by approximately solving the KKT equations in the least-squares sense subject to $\boldsymbol{\lambda} > \mathbf{0}$, by Equation (B.8).

$$\nabla_{\mathbf{x}}\mathcal{L} = \nabla_{\mathbf{x}} f(\mathbf{x}) + \sum_j \lambda_j \nabla g_j(\mathbf{x}) + \sum_l y_l \nabla h_l(\mathbf{x}) = 0 \tag{B.8}$$

It takes a step $(\Delta\mathbf{x}, \Delta\mathbf{s})$ to approximately solve the optimization problem in Equation (B.9).

$$\min_{\Delta\mathbf{x},\Delta\mathbf{s}} \nabla f^T \Delta\mathbf{x} + \frac{1}{2}\Delta\mathbf{x}^T \nabla^2_{xx}\mathcal{L}\Delta\mathbf{x} + \mu\mathbf{e}^T\mathbf{S}^{-1}\Delta\mathbf{s} + \frac{1}{2}\Delta\mathbf{s}^T\mathbf{S}^{-1}\boldsymbol{\Lambda}\Delta\mathbf{s} \tag{B.9}$$

subject to

$$\mathbf{g}(\mathbf{x}) + \mathbf{J_g}\Delta\mathbf{x} + \Delta\mathbf{s} = \mathbf{0}$$

$$\mathbf{h}(\mathbf{x}) + \mathbf{J_h}\Delta\mathbf{x} = \mathbf{0}$$

To solve the linearized constraints of Equation (B.9), the algorithm tries to minimize a norm of the linearized constraints inside the region with a radius scaled by $R$. The objective function of Equation (B.9) is afterwards solved with the constraints being to match the residual from solving the constraints, staying within the trust region with radius $R$ and keeping $\mathbf{s}$ strictly positive. For details on the algorithm and the derivation, the reader is referred to [73–75].

## B.3. Pattern search

Pattern search is a method for solving optimization problems that does not require any information about the gradient of the objective function. Unlike more traditional optimization methods that use information about the gradient or higher derivatives to search for an optimal point, the pattern search algorithm searches a set of points around the current point, looking for one where the value of the objective function is lower than the value at the current point. Pattern search can be used to solve problems for which the objective function is not differentiable or not even continuous.

Pattern search algorithms compute a sequence of points that approach an optimal point. At each step, the algorithm searches a set of points (called a mesh) around the current point; the point computed at the previous step of the algorithm. The mesh is formed by adding the current point to a scalar multiple of a set of vectors called a pattern. If the *patternsearch* algorithm finds a point in the mesh that improves the objective function at the current point, the new point becomes the current point at the next step of the algorithm. The Generalized Pattern Search (GPS) algorithm uses fixed direction vectors.

**Patterns** A pattern is a set of vectors $\mathbf{v}_j$ that the pattern search algorithm uses to determine which points to search at each iteration. The set $\mathbf{v}_j$ is defined by the number of independent variables in the objective function, $N$, and the positive basis set. Two commonly used positive basis sets in pattern search algorithms are the maximal basis, with $2N$ vectors, and the minimal basis, with $N+1$ vectors.

With GPS, the collection of vectors that form the pattern are fixed-direction vectors. For example, if there are three independent variables in the optimization problem, the default for a $2N$ positive basis consists of the following pattern vectors:

$$\mathbf{v}_1 = \begin{bmatrix}1 & 0 & 0\end{bmatrix} \quad \mathbf{v}_2 = \begin{bmatrix}0 & 1 & 0\end{bmatrix} \quad \mathbf{v}_3 = \begin{bmatrix}0 & 0 & 1\end{bmatrix}$$
$$\mathbf{v}_4 = \begin{bmatrix}-1 & 0 & 0\end{bmatrix} \quad \mathbf{v}_5 = \begin{bmatrix}0 & -1 & 0\end{bmatrix} \quad \mathbf{v}_6 = \begin{bmatrix}0 & 0 & -1\end{bmatrix}$$

A $N+1$ positive basis consists of the following default pattern vectors:

$$\mathbf{v}_1 = \begin{bmatrix}1 & 0 & 0\end{bmatrix} \quad \mathbf{v}_2 = \begin{bmatrix}0 & 1 & 0\end{bmatrix} \quad \mathbf{v}_3 = \begin{bmatrix}0 & 0 & 1\end{bmatrix} \quad \mathbf{v}_4 = \begin{bmatrix}-1 & -1 & -1\end{bmatrix}$$

Depending on the poll method choice, the number of vectors selected will be $2N$ or $N+1$. As in GPS $2N$ vectors consist of $N$ vectors and their $N$ negatives, while $N+1$ vectors consist of $N$ vectors and one that is the negative of the sum of the others.

**Meshes** At each step, *patternsearch* searches a set of points for a point that improves the objective function. The algorithm forms the mesh by:

1. Generating a set of vectors $\mathbf{d}_j$, by multiplying each pattern vector $\mathbf{v}_j$ by a scalar $\Delta^m$. $\Delta^m$ is called the mesh size.
2. Adding the $\mathbf{d}_j$ to the current point; the point with the best objective function value found at the previous step.

For example, using the GPS algorithm with a $2N$ positive basis set, suppose that:

- The current point is $\begin{bmatrix}1.6 & 3.4\end{bmatrix}$.
- The pattern consists of the vectors: $\mathbf{v}_1 = \begin{bmatrix}1 & 0\end{bmatrix}$, $\mathbf{v}_2 = \begin{bmatrix}0 & 1\end{bmatrix}$, $\mathbf{v}_3 = \begin{bmatrix}-1 & 0\end{bmatrix}$ and $\mathbf{v}_4 = \begin{bmatrix}0 & -1\end{bmatrix}$.
- The current mesh size is $\Delta^m = 4$.

The algorithm multiplies the pattern vectors with 4 and adds them to the current point to obtain the following mesh:

$$\begin{bmatrix}1.6 & 3.4\end{bmatrix} + 4 \cdot \begin{bmatrix}1 & 0\end{bmatrix} = \begin{bmatrix}5.6 & 3.4\end{bmatrix}$$
$$\begin{bmatrix}1.6 & 3.4\end{bmatrix} + 4 \cdot \begin{bmatrix}0 & 1\end{bmatrix} = \begin{bmatrix}1.6 & 7.4\end{bmatrix}$$
$$\begin{bmatrix}1.6 & 3.4\end{bmatrix} + 4 \cdot \begin{bmatrix}-1 & 0\end{bmatrix} = \begin{bmatrix}-2.4 & 3.4\end{bmatrix}$$
$$\begin{bmatrix}1.6 & 3.4\end{bmatrix} + 4 \cdot \begin{bmatrix}0 & -1\end{bmatrix} = \begin{bmatrix}1.6 & -0.6\end{bmatrix}$$

The pattern vector that produces a mesh point is called its direction. A pattern search will sometimes run faster using GPS Positive basis Np1 rather than the GPS Positive basis 2N as the poll method, because the algorithm searches fewer points at each iteration[70].

**Polling** At each step, the algorithm polls the points in the current mesh by computing their objective function values. When the `Complete poll` option has the (default) setting `Off`, the algorithm stops polling the mesh points as soon as it finds a point whose objective function value is less than that of the current point. If this occurs, the poll is called successful and the point it finds becomes the current point at the next iteration.

The algorithm only computes the mesh points and their objective function values up to the point at which it stops the poll. If the algorithm fails to find a point that improves the objective function, the poll is called unsuccessful and the current point stays the same at the next iteration.

When the `Complete poll` option has the setting `On`, the algorithm computes the objective function values at all mesh points. The algorithm then compares the mesh point with the smallest objective function value to the current point. If that mesh point has a smaller value than the current point, the poll is successful.

For problems in which there are several local minima, it is sometimes preferable to make the pattern search poll all the mesh points at each iteration and choose the one with the best objective function value[70]. A complete poll enables the pattern search to explore more points at each iteration and thereby potentially avoid a local minimum that is not the global minimum.

**Expanding and Contracting** After polling, the algorithm changes the value of the mesh size $\Delta^m$. The default is to multiply $\Delta^m$ with $2$ after a successful poll, and with $0.5$ after an unsuccessful poll.

**Stopping Conditions** The algorithm stops when any of the following conditions occurs:

- The mesh size is less than `Mesh tolerance`.
- The number of iterations performed by the algorithm reaches the value of `Max iteration`.
- The total number of objective function evaluations performed by the algorithm reaches the value of `Max function evaluations`.
- The algorithm runs until the time in seconds reaches the value of `Time limit`.
- The distance between the points found in two consecutive iterations and the mesh size are both less than `X tolerance`.
- The change in the objective function in two consecutive iterations and the mesh size are both less than `Function tolerance`.

Most optimization runs stop as a consequence of the first mentioned stopping criterion.

## B.4. Simulated annealing

Simulated annealing is a method for solving unconstrained and bound-constrained optimization problems. The method models the physical process of heating a material and then slowly lowering the temperature to decrease defects, i.e. minimizing the system energy.

At each iteration of the simulated annealing algorithm, a new point is randomly generated. The distance of the new point from the current point, or the extent of the search, is based on a probability distribution with a scale proportional to the temperature. The algorithm accepts all new points that lower the objective function value, but also (with a certain probability) points that raise the objective function value.

By accepting points that raise the objective function value, the algorithm avoids being trapped in local minima and is able to explore globally for more possible solutions. An annealing schedule is selected to systematically decrease the temperature as the algorithm proceeds. As the temperature decreases, the algorithm reduces the extent of its search to converge to a minimum.

The simulated annealing algorithm performs the below described steps[76].

1. The algorithm generates a random trial point. The algorithm chooses the distance of the trial point from the current point by a probability distribution with a scale depending on the current temperature. The step length equals the current temperature and the direction choice is uniformly random.

2. The algorithm determines whether the new point is better or worse than the current point. If the new point is better than the current point, it becomes the next point. If the new point is worse than the current point, the algorithm can still make it the next point. The algorithm accepts a worse point based on an acceptance function. For the 'Simulated annealing acceptance function', the probability of acceptance is: $\frac{1}{1+e^{\frac{\Delta f_{no}}{\max(\tau)}}}$.

   In this function $\Delta f_{no}$ is the absolute difference between the new and the old objective function value, $\tau_0$ is the initial temperature of component $j$ and $\tau$ is the current temperature. Since both $\Delta f_{no}$ and $\tau$ are positive, the probability of acceptance is between $0$ and $\frac{1}{2}$. Smaller temperature leads to smaller acceptance probability. Larger $\Delta f_{no}$ also leads to smaller acceptance probability.

3. The algorithm systematically lowers the temperature, storing the best point found so far. The function used by the algorithm to update the temperature is $\tau = \tau_0 \cdot 0.95^q$, where $q$ denotes the annealing parameter. The annealing parameter is the same as the iteration number until re-annealing.

4. *simulannealbnd* re-anneals after it accepts 100 points. Re-annealing sets the annealing parameters to lower values than the iteration number, thus raising the temperature in each dimension. The annealing parameters depend on the values of the estimated gradients of the objective function in each dimension. The basic formula is $q_j = \log\left(\frac{\tau_0}{\tau_j}\frac{\max_l(w_l)}{s_j}\right)$, where $q_j$ is the annealing parameter for component $j$, $\tau_0$ and $\tau_j$ are the initial and current temperature of component $j$ and $w_j$ is the gradient of the objective function value in direction $j$ times difference of bounds in direction $j$.

5. The algorithm stops when the average change in the objective function is smaller than the `TolFun` tolerance, or when it reaches any other stopping criterion.

## B.5. Genetic algorithm

The genetic algorithm is a method for solving both constrained and unconstrained optimization problems that is based on natural selection; the process that drives biological evolution. The genetic algorithm repeatedly modifies a population of individual solutions. At each step, the genetic algorithm selects individuals at random from the current population to be parents and uses them to produce children for the next generation. Over successive generations, the population "evolves" toward an optimal solution.

Genetic algorithm can be applied to solve a variety of optimization problems that are not well suited for standard optimization algorithms, including problems in which the objective function is discontinuous, non-differentiable, stochastic, or highly non-linear. The genetic algorithm can address problems of mixed integer programming, where some components are restricted to be integer-valued[77, 78].

The genetic algorithm uses three main types of rules at each step to create the next generation from the current population:

- Selection rules select the individuals (parents) that contribute to the population at the next generation.
- Crossover rules combine two parents to form children for the next generation.
- Mutation rules apply random changes to individual parents to form children.

The following outline summarizes how the genetic algorithm works.

1. The algorithm begins by creating a random initial population.

2. The algorithm then creates a sequence of new populations. At each step, the algorithm uses the individuals in the current generation to create the next population. To create the new population, the algorithm performs the following steps:

   (a) Scores each member of the current population by computing its fitness value.
   (b) Scales the raw fitness scores to convert them into a more usable range of values.

   (c) Selects members, called parents, based on their fitness
   (d) Some of the individuals in the current population that have lower fitness are chosen as elite. Elite individuals are passed to the next population.
   (e) Produces children from the parents. Children are produced either by making random changes to a single parent (mutation) or by combining the vector entries of a pair of parents (crossover).
   (f) Replaces the current population with the children to form the next generation.

3. The algorithm stops when one of the stopping criteria is met.

# C

# Numerical results of the axial induction optimization.

Table C.1: Numerical results of the axial induction optimization problem (Case A1).

| | [−] | | | | [kW] | | | | | | | | | [%] | | | [min] |
|---|---|---|---|---|---|---|---|---|---|---|---|---|---|---|---|---|---|
| **Algorithm** | $\mathbf{a}_{\mathbf{1},\mathrm{init}}$ | $\mathbf{a}_{\mathbf{2},\mathrm{init}}$ | $\mathbf{a}_{\mathbf{1},\mathrm{opt}}$ | $\mathbf{a}_{\mathbf{2},\mathrm{opt}}$ | $\mathbf{P}_{\mathbf{1},\mathrm{init}}$ | $\mathbf{P}_{\mathbf{2},\mathrm{init}}$ | $\mathbf{P}_{\mathbf{3},\mathrm{init}}$ | $\mathbf{P}_{\mathrm{tot,init}}$ | $\mathbf{P}_{\mathbf{1},\mathrm{opt}}$ | $\mathbf{P}_{\mathbf{2},\mathrm{opt}}$ | $\mathbf{P}_{\mathbf{3},\mathrm{opt}}$ | $\mathbf{P}_{\mathrm{tot,opt}}$ | $\boldsymbol{\Delta}\mathbf{P}_{\mathrm{opt,Betz}}$ | $\mathbf{I}_{\mathrm{P}}$ | $\boldsymbol{\xi}_{\mathrm{P,init}}$ | $\boldsymbol{\xi}_{\mathrm{P,opt}}$ | $\mathbf{t}_{\mathrm{opt}}$ |
| Betz | $\frac{1}{3}$ | $\frac{1}{3}$ | | | 1816 | 549 | 691 | 3056 | | | | | | | 43.90 | | |
| Robust | | | 0.230 | 0.340 | | | | | 1672 | 717 | 798 | 3187 | 131 | 4.29 | | 41.50 | 503.0 |
| fminsearch | $\frac{1}{3}$ | $\frac{1}{3}$ | 0.2315 | 0.3410 | 1816 | 549 | 691 | 3056 | 1676 | 713 | 799 | 3188 | 132 | 4.31 | 43.90 | 41.49 | 5.6 |
| | $\frac{53}{600}$ | $\frac{53}{600}$ | 0.0829 | 0.0919 | 900 | 664 | 1075 | 2640 | 854 | 708 | 1080 | 2642 | −414 | −13.54 | 51.55 | 51.50 | 2.2 |
| | $\frac{1}{300}$ | $\frac{1}{300}$ | 0.2329 | 0.3394 | 41 | 40 | 1801 | 1882 | 1680 | 709 | 799 | 3188 | 132 | 4.31 | 65.46 | 41.49 | 7.8 |
| fmincon | $\frac{1}{3}$ | $\frac{1}{3}$ | 0.2083 | 0.3367 | 1816 | 549 | 691 | 3056 | 1600 | 784 | 780 | 3164 | 108 | 3.52 | 43.90 | 41.93 | 6.1 |
| | $\frac{53}{600}$ | $\frac{53}{600}$ | 0.0830 | 0.0868 | 900 | 664 | 1075 | 2640 | 855 | 676 | 1111 | 2642 | −414 | −13.55 | 51.55 | 51.01 | 2.6 |
| | $\frac{1}{300}$ | $\frac{1}{300}$ | 0.2329 | 0.3264 | 41 | 40 | 1801 | 1882 | 1680 | 709 | 798 | 3187 | 131 | 4.28 | 65.46 | 41.51 | 5.6 |
| Pattern Search | $\frac{1}{3}$ | $\frac{1}{3}$ | 0.2298 | 0.3393 | 1816 | 549 | 691 | 3056 | 1671 | 718 | 799 | 3188 | 131 | 4.30 | 43.90 | 41.49 | 7.9 |
| | $\frac{53}{600}$ | $\frac{53}{600}$ | 0.2329 | 0.3400 | 900 | 664 | 1075 | 2640 | 1680 | 709 | 799 | 3188 | 132 | 4.31 | 51.55 | 41.49 | 7.6 |
| | $\frac{1}{300}$ | $\frac{1}{300}$ | 0.2298 | 0.3390 | 41 | 40 | 1801 | 1882 | 1671 | 718 | 799 | 3188 | 131 | 4.30 | 65.46 | 41.49 | 9.2 |
| Simulated Annealing | $\frac{1}{3}$ | $\frac{1}{3}$ | 0.2299 | 0.3263 | 1816 | 549 | 691 | 3056 | 1671 | 717 | 798 | 3186 | 130 | 4.26 | 43.90 | 41.51 | 109.4 |
| | $\frac{53}{600}$ | $\frac{53}{600}$ | 0.2282 | 0.3379 | 900 | 664 | 1075 | 2640 | 1666 | 722 | 798 | 3186 | 130 | 4.26 | 51.55 | 41.51 | 103.1 |
| | $\frac{1}{300}$ | $\frac{1}{300}$ | 0.2337 | 0.3415 | 41 | 40 | 1801 | 1882 | 1682 | 707 | 797 | 3186 | 130 | 4.26 | 65.46 | 41.51 | 166.3 |
| Genetic Algorithm | $\frac{1}{3}$ | $\frac{1}{3}$ | 0.2315 | 0.3395 | 1816 | 549 | 691 | 3056 | 1676 | 713 | 799 | 3188 | 132 | 4.31 | 43.90 | 41.49 | 221.2 |
| | $\frac{53}{600}$ | $\frac{53}{600}$ | 0.2329 | 0.3396 | 900 | 664 | 1075 | 2640 | 1680 | 709 | 799 | 3188 | 132 | 4.31 | 51.55 | 41.49 | 234.6 |
| | $\frac{1}{300}$ | $\frac{1}{300}$ | 0.2329 | 0.3397 | 41 | 40 | 1801 | 1882 | 1680 | 709 | 799 | 3188 | 132 | 4.31 | 65.46 | 41.49 | 166.3 |

# D

# Numerical results of the performance curve optimization.

Table D.1: Numerical results of performance curve optimization Case B1.

|  | [−] | [GWh] |  |  |  | [MWh] | [%] |  | [min] |
|---|---|---|---|---|---|---|---|---|---|
| **TolMesh** | $a_{opt}$ | **$AEP_1$** | **$AEP_2$** | **$AEP_3$** | **$AEP_{tot}$** | **$\Delta AEP_{opt,Betz}$** | $I_{AEP}$ | $\xi_{AEP,opt}$ | $t_{opt}$ |
| Betz | [0.3333 0.3333 0.3333 0.3333 0.3333 0.3333 0.3333 0.3333 0.3333 0.3333 0.1826 0.1219 0.0891 0.0682] | 10.67 | 7.18 | 6.78 | 24.62 |  |  | 23.066 |  |
| $10^{-2}$ | [0.3333 0.3281 0.3333 0.3281 0.3281 0.3281 0.3229 0.3333 0.2813 0.2656 0.1826 0.1219 0.0891 0.0682] | 10.61 | 7.24 | 6.87 | 24.72 | 99.6 | 0.40 | 22.755 | 125 |
| $10^{-3}$ | [0.3281 0.3307 0.3320 0.3294 0.3294 0.3255 0.3236 0.3307 0.2813 0.2656 0.1826 0.1219 0.0891 0.0682] | 10.61 | 7.24 | 6.87 | 24.72 | 100.5 | 0.41 | 22.752 | 244 |
| $10^{-4}$ | [0.3281 0.3308 0.3320 0.3289 0.3289 0.3262 0.3239 0.3302 0.2813 0.2651 0.1826 0.1219 0.0890 0.0682] | 10.61 | 7.24 | 6.87 | 24.73 | 102.3 | 0.42 | 22.747 | 472 |
| $10^{-5}$ | [0.3281 0.3308 0.3320 0.3289 0.3289 0.3262 0.3239 0.3302 0.2813 0.2651 0.1826 0.1219 0.0890 0.0682] | 10.61 | 7.24 | 6.87 | 24.73 | 102.3 | 0.42 | 22.747 | 621 |
| $10^{-6}$ | [0.3281 0.3308 0.3320 0.3289 0.3289 0.3262 0.3239 0.3302 0.2813 0.2651 0.1826 0.1219 0.0890 0.0682] | 10.61 | 7.24 | 6.87 | 24.73 | 102.3 | 0.42 | 22.747 | 1857 |

Table D.2: Numerical results of performance curve optimization Case B2.

|  |  |  | [−] | [GWh] |  |  |  | [MWh] | [%] |  | [min] |
|---|---|---|---|---|---|---|---|---|---|---|---|
| **PollMethod** | **CompletePoll** | $x_0$ | $a_{opt}$ | **$AEP_1$** | **$AEP_2$** | **$AEP_3$** | **$AEP_{tot}$** | **$\Delta AEP_{opt,Betz}$** | $I_{AEP}$ | $\xi_{AEP,opt}$ | $t_{opt}$ |
| Betz |  |  | [0.3333 0.3333 0.3333 0.3333 0.3333 0.3333 0.3333 0.3333 0.3333 0.3333 0.1826 0.1219 0.0891 0.0682] | 10.67 | 7.18 | 6.78 | 24.62 |  |  | 23.07 |  |
| GPSPositiveBasis2N | off | A | [0.3281 0.3308 0.3320 0.3289 0.3289 0.3262 0.3239 0.3302 0.2813 0.2651 0.1826 0.1219 0.0890 0.0682] | 10.61 | 7.24 | 6.87 | 24.73 | 102.3 | 0.42 | 22.75 | 472 |
| GPSPositiveBasis2N | off | B | [0.3331 0.3305 0.3312 0.3291 0.3292 0.3221 0.3265 0.3165 0.2427 0.2550 0.1823 0.1218 0.0890 0.0682] |  |  |  |  |  | 0.43 | 22.73 | 631 |
| GPSPositiveBasis2N | off | C | [0.3328 0.3302 0.3313 0.3295 0.3295 0.3233 0.3269 0.3158 0.2449 0.2559 0.1823 0.1218 0.0890 0.0681] | 10.56 | 7.29 | 6.88 | 24.73 | 105.1 | 0.43 | 22.74 | 835 |
| GPSPositiveBasisNp1 | on | A | [0.3327 0.3319 0.3322 0.3306 0.3308 0.3268 0.3241 0.3201 0.2889 0.2681 0.1826 0.1218 0.0890 0.0682] | 10.62 | 7.24 | 6.87 | 24.72 | 99.8 | 0.41 | 22.75 | 321 |
| GPSPositiveBasisNp1 | on | B | [0.3331 0.3302 0.3302 0.3299 0.3289 0.3282 0.3223 0.3170 0.3116 0.2699 0.1823 0.1217 0.0890 0.0682] | 10.63 | 7.23 | 6.86 | 24.72 | 95.2 | 0.39 | 22.77 | 415 |
| GPSPositiveBasisNp1 | on | C | [0.3331 0.3305 0.3326 0.3300 0.3300 0.3223 0.3276 0.3189 0.2336 0.2336 0.1823 0.1217 0.0890 0.0681] | 10.50 | 7.32 | 6.91 | 24.73 | 105.1 | 0.43 | 22.74 | 1220 |

Table D.3: Numerical results of performance curve optimization Case B3.

|  | [m/s] | [−] | [GWh] |  |  |  | [MWh] | [%] |  | [min] |
|---|---|---|---|---|---|---|---|---|---|---|
| **Control points** | $u_{\infty,opt}$ | $a_{opt}$ | **$AEP_1$** | **$AEP_2$** | **$AEP_3$** | **$AEP_{tot}$** | **$\Delta AEP_{opt,Betz}$** | $I_{AEP}$ | $\xi_{AEP,opt}$ | $t_{opt}$ |
| Betz |  |  | 10.67 | 7.18 | 6.78 | 24.62 |  |  | 23.07 |  |
| 3 | [0 8.7500 14.0000] | [0.3333 0.3333 0.2708] | 10.66 | 7.20 | 6.80 | 24.66 | 41.3 | 0.17 | 22.94 | 19 |
| 4 | [0 8.0573 8.1302 14.0000] | [0.3333 0.3307 0.3099 0.2891] | 10.66 | 7.20 | 6.80 | 24.66 | 41.0 | 0.17 | 22.94 | 33 |
| 5 | [0 2.6250 6.1250 6.1250 14.0000] | [0.3343 0.3021 0.3646 0.3021 0.3021] | 10.66 | 7.20 | 6.80 | 24.66 | 39.3 | 0.16 | 22.94 | 34 |
| 6 | [0 2.2750 5.5125 7.0000 8.6625 14.0000] | [0.3333 0.3130 0.3568 0.3083 0.3076 0.3083] | 10.66 | 7.20 | 6.80 | 24.66 | 38.1 | 0.15 | 22.95 | 105 |

Table D.4: Numerical results of performance curve optimization Case B4.

| | [m/s] | [−] | [GWh] | | | | [MWh] | [%] | | [min] |
|---|---|---|---|---|---|---|---|---|---|---|
| **Control points** | $\mathbf{u}_{\infty,\mathrm{opt}}$ | $\mathbf{a}_{\mathrm{opt}}$ | $\mathbf{AEP}_1$ | $\mathbf{AEP}_2$ | $\mathbf{AEP}_3$ | $\mathbf{AEP}_{\mathrm{tot}}$ | $\mathbf{\Delta AEP}_{\mathrm{opt,Betz}}$ | $\mathbf{I}_{\mathrm{AEP}}$ | $\boldsymbol{\xi}_{\mathrm{AEP,opt}}$ | $\mathbf{t}_{\mathrm{opt}}$ |
| Betz | | | 10.67 | 7.18 | 6.78 | 24.62 | | | 23.07 | |
| 3 | $[0 \quad 3.2813 \quad 14.0000]$ | $[0.1497 \quad 0.2747 \quad 0.2122]$ | 10.36 | 7.55 | 7.02 | 24.92 | 299.5 | 1.22 | 22.13 | 37 |
| 4 | $[0 \quad 1.2031 \quad 5.8333 \quad 14.0000]$ | $[0.0085 \quad 0.3750 \quad 0.2083 \quad 0.2083]$ | 10.34 | 7.56 | 7.00 | 24.91 | 283.9 | 1.15 | 22.18 | 46 |
| 5 | $[0 \quad 0.3281 \quad 3.0625 \quad 7.0000 \quad 14.0000]$ | $[0.0990 \quad 0.3646 \quad 0.1693 \quad 0.2396 \quad 0.2396]$ | 10.37 | 7.54 | 7.02 | 24.92 | 301.1 | 1.22 | 22.13 | 61 |

Table D.5: Numerical results of performance curve optimization Case B5.

| | [m/s] | [−] | [GWh] | | | | | | | | | [MWh] | [%] | | [min] |
|---|---|---|---|---|---|---|---|---|---|---|---|---|---|---|---|
| **Control points** | $\mathbf{u}_{\infty,\mathrm{opt}}$ | $\mathbf{a}_{\mathrm{opt}}$ | $\mathbf{AEP}_1$ | $\mathbf{AEP}_2$ | $\mathbf{AEP}_3$ | $\mathbf{AEP}_4$ | $\mathbf{AEP}_5$ | $\mathbf{AEP}_6$ | $\mathbf{AEP}_7$ | $\mathbf{AEP}_8$ | $\mathbf{AEP}_{\mathrm{tot}}$ | $\mathbf{\Delta AEP}_{\mathrm{opt,Betz}}$ | $\mathbf{I}_{\mathrm{AEP}}$ | $\boldsymbol{\xi}_{\mathrm{AEP,opt}}$ | $\mathbf{t}_{\mathrm{opt}}$ |
| Betz | | | 10.67 | 7.18 | 6.78 | 7.21 | 7.32 | 7.29 | 7.24 | 7.17 | 60.85 | | | 28.70 | |
| 3 | $[0 \quad 10.4453 \quad 14.0000]$ | $[0.3333 \quad 0.2396 \quad 0.2630]$ | 10.56 | 7.26 | 6.82 | 7.24 | 7.37 | 7.35 | 7.31 | 7.26 | 61.18 | 323.37 | 0.53 | 28.32 | 117 |
| 4 | $[0 \quad 1.3672 \quad 1.4036 \quad 14.0000]$ | $[0.3060 \quad 0.3776 \quad 0.2891 \quad 0.2467]$ | 10.57 | 7.26 | 6.82 | 7.24 | 7.37 | 7.35 | 7.31 | 7.26 | 61.19 | 330.76 | 0.54 | 28.31 | 227 |

Table D.6: Numerical results of performance curve optimization Case B6.

| [m/s] | [−] | [GWh] | | | | [MWh] | [%] | | [min] |
|---|---|---|---|---|---|---|---|---|---|
| $\mathbf{u}_{\infty,\mathrm{opt}}$ | $\mathbf{a}_{\mathrm{opt}}$ | $\mathbf{AEP}_{\mathrm{A}}$ | $\mathbf{AEP}_{\mathrm{B}}$ | $\mathbf{AEP}_{\mathrm{C}}$ | $\mathbf{AEP}_{\mathrm{tot}}$ | $\mathbf{\Delta AEP}_{\mathrm{opt,Betz}}$ | $\mathbf{I}_{\mathrm{AEP}}$ | $\boldsymbol{\xi}_{\mathrm{AEP,opt}}$ | $\mathbf{t}_{\mathrm{opt}}$ |
| Betz | | 9.84 | 9.80 | 10.05 | 157.96 | | | 7.46 | |
| $[0 \quad 7.9219 \quad 13.0000]$ | $[0.3255 \quad 0.3333 \quad 0.3021]$ | 9.84 | 9.81 | 10.05 | 158.04 | 72.88 | 0.046 | 7.42 | 430 |